공학박사 학위논문

Development of a Two-step Pin-by-Pin Core Calculation System for Commercial Nuclear Design Applications

상용 핵설계 적용을 위한 2단계 봉단위 노심 계산 체계 개발

2021년 8월

서울대학교 대학원

에너지시스템공학부

윤 주 일

Development of a Two-step Pin-by-Pin Core Calculation System for Commercial Nuclear Design Applications

상용 핵설계 적용을 위한
2단계 봉단위 노심 계산 체계 개발

지도 교수 주 한 규

이 논문을 공학박사 학위논문으로 제출함
2021년 8월

서울대학교 대학원
에너지시스템공학부
윤 주 일

윤주일의 공학박사 학위논문을 인준함
2021년 7월

위 원 장 _____ 심 형 진 _____

부위원장 _____ 주 한 규 _____

위 원 _____ 이 덕 중 _____

위 원 _____ 이 현 철 _____

위 원 _____ 조 진 영 _____

Abstract

A pin-wise three-dimensional nuclear design code newly has been developed as an effort to establish more accurate, yet practically applicable to commercial nuclear designs. As neutronics solvers, the numerical methods based on the traditional diffusion theory are implemented with the pin-wise finite difference method (FDM) and coarse mesh finite difference (CMFD) method coupled with the semi-analytic nodal method and evaluated which numerical method is practically desired. The planar parallelization method and the two-level CMFD acceleration method are incorporated to achieve high calculating performance. Since the lattice calculation based on MOC is still used to generate pin-wise group constants for each slice of an assembly, the pin-wise equivalence factors such as the flux discontinuity factors or the super homogenization factors are examined to preserve the higher order solutions of the lattice calculation. The accuracy and performance of the proposed methods are tested with the C5G7MOX, VERA, BanDi-50 and APR1400 benchmark problems. The results indicate the superiority of the pin-wise calculations compared to the traditional node-wise calculations and the computing time and resources are reasonable for the commercial reactor core designs. To assess transient calculation capability, SPERT III E-Core transient problems are solved. With the proper kinetic nuclear parameters, the pin-wise transient calculation shows good agreement on the higher order solutions.

KEYWORDS : Pin-by-Pin Calculation, SPH, CMFD, C5G7, VERA, APR1400

Student Number : 2011-30995

Table of Contents

List of Tables

List of Figures

1. Introduction

As the commercial nuclear design procedure, the two-step calculation approach has been widely used. The first step is to generate assembly-wise homogeneous group constants such as cross-sections and diffusion coefficients as solving two-dimensional lattice problems with higher-order calculations. In this step, the method of characteristics has been widely used. The second step is to solve three-dimensional core problems and obtain neutronics solutions such as reactivity and flux/power distributions. In this step, the various nodal methods coupled with some efficient accelerations are implemented. The source expansion nodal method coupled with the two-level coarse mesh finite difference method introduced in the previous work [1] is also one of the good solutions. The conventional nuclear design code systems are still valid for the commercial PWR nuclear designs with appropriate bias and uncertainties. However, the safety regulations have been strengthened and strict regulations have been additionally introduced for the safety analysis. In this circumstance, the more accurate solutions of neutronics calculations are also requested.

With the increasing need for the more accurate reactor calculation, there have been various researches to develop cutting-edge core calculation codes based on the neutron transport methods in recent years. The deterministic

codes such as nTRACER [2], DeCART [3], MPACT [4], OpenMOC [5] and the stochastic codes such as MCNP [6], KENO [7], OpenMC [8] rapidly have been developed and improved as the computing power have been grown. The fuel vendors have also tried to adopt the transport codes to improve an accuracy of core calculations. In commercial core designs, thousands of three-dimensional core calculation are performed for searching the proper loading patterns and generate lots of nuclear design data for each cycle of all reactors. With this reason, the direct whole core transport calculations are still impractical because they require too much computing resource and calculation time. Therefore, we need other solutions that should provide more accurate results competing with them of transport codes, yet reasonable calculation speed. The pin-by-pin calculation method lately has received attention from the nuclear industries since the method reduces numerical errors originated from the assembly-wise spatial homogenization. There are various researches to incorporate the pin-by-pin calculation formulated with the diffusion method, the simplified P3 method [9], and other low-order methods. The AEGIS/SCOPE2 code system [10] developed by NFI and NEL of Japan is one of the highly developed nuclear design code system. In this system, AEGIS is the conventional lattice code incorporating the method of characteristics to generate pin-wise group constants and SCOPE2 is the pin-wise core calculation code based on the SP3 method. Especially, the GPGPU

is introduced in SCOPE2 to maximize computing performance. Similar to the NFI/NEL's work, many researches have been working on that kind of parallelization for maximizing the calculating performance as introducing the cutting-edge computing systems based on GPGPU. However, fuel vendors are still utilizing the conventional CPU-based multicore computing systems and sharing them with a lot of computer codes. Therefore, the three-dimensional pin-by-pin nuclear design code system based on the practical computing environments is more practical and useful for commercial nuclear designs.

In this work, the conventional finite difference method based on the diffusion theory and the planar parallelization with 2D/1D decoupling calculation is introduced to maximize the pin-wise calculation performance. And, the pin-wise equivalence factors are introduced and evaluated to reduce the spatial error originated from the low-order approximation of the diffusion calculation where pin-wise group constants are used. In the following section, the two-step calculation procedure is referred to solve three-dimensional pin-wise core problems in detail. After that, the well-known L336C5 [11] and VERA [12] benchmark problems are solved for evaluating performance and accuracy of the proposed pin-wise calculation as comparing to the conventional nodal calculation. Moreover, benchmark problems based on the realistic small modular reactors and commercial reactors are solved to verify

applicability of the pin-wise calculations for small modular reactors and commercial reactors.

2. Calculational Method

2.1. Two-step core calculation procedure

The typical core calculation procedure is divided into two steps. In the first step, the assembly-wise two-dimensional higher order calculations are performed as considering detail geometry information such as pellet, gap, clad, etc. The collision probability method [13] and method of characteristics are usually used in this step. After the assembly-wise calculation, the representative homogeneous cross-sections are generated as preserving the group-wise reaction rates with the flux-volume weighting process. After that, the core problems are constructed with the pre-generated homogeneous group constants and they are solved with the efficient nodal or finite difference methods. The pin-wise core calculations suggested in this work basically follows the typical two-step calculation procedure. But the pin-wise group constants instead of the assembly-wise group constants are generated with some techniques in the first step and the three-dimensional core problems are composed of the pin-wise group constants. Therefore, it is obviously important to determine how to generate the pin-wise group constants.

2.2. Pin-wise homogenization

The lattice calculation is still mandatory to generate pin-wise homogeneous coarse-group constants with the pin-wise homogenization process. The essential group constants for the pin-wise core calculation are $D, \Sigma_{tr}, \Sigma_a, \nu\Sigma_f, \kappa\Sigma_f, \Sigma_s \; and \; \chi$. The homogenization is performed as preserving reaction rates of the specified energy groups and volumes as the following equation.

$$\bar{\Sigma}_{x,g,i}\bar{\phi}_{g,i}V_i = RR_{x,g,i}V_i = \sum_{j\in i}^{V_i} \Sigma_{x,g,j}\phi_{g,j}V_j \qquad (2.1)$$

where

$\bar{\Sigma}_{x,g,i}$: Pin-wise homogenized cross-section of reaction x, group g at pin index i,

$\bar{\phi}_{g,i}$: Homogenized neutron flux of group g at pin index i,

V_i: Total volume of pin index i $(= \sum_j^{V_i} V_j)$,

V_j: Volume of sub region index j,

$RR_{x,g,i}$: Reaction rate of reaction type x, group g at pin index i,

$\Sigma_{x,g,j}$: Cross-section of reaction type x, group g at sub region j,

$\phi_{g,j}$: Average flux of group g at sub region j.

The homogeneous cross-section of each pin is obtained with the following equation.

$$\bar{\Sigma}_{x,g,i} = \frac{RR_{x,g,i}}{\bar{\phi}_{g,i}} = \frac{\sum_j^{V_i} \Sigma_{x,g,j}\phi_{g,j}V_j}{\sum_j^{V_i} \phi_{g,j}V_j} \quad (2.2)$$

Especially, the diffusion coefficient is not directly homogenized but obtained from the transport cross-section homogenization as the following.

$$\bar{\Sigma}_{tr,g,i} = \frac{\sum_j^{V_i} \Sigma_{tr,g,j}\phi_{g,j}V_j}{\sum_j^{V_i} \phi_{g,j}V_j} \quad (2.3)$$

$$\bar{D}_{g,i} = \frac{1}{3\bar{\Sigma}_{tr,g,i}} \quad (2.4)$$

where

$\bar{\Sigma}_{tr,g,i}$: Homogenized transport cross-section of group *g* at pin index *i*,

$\Sigma_{tr,g,j}$: Macroscopic transport cross-section of group *g* at sub region *j*,

$\bar{D}_{g,i}$: Diffusion coefficient of group *g* at pin index *i*.

Different from the other constants, the fission spectrum should be homogenized with fission source weighting as shown in the following equation.

$$\bar{\chi}_{g,i} = \frac{\sum_j^{V_i} \chi_{g,j}\psi_j}{\bar{\psi}_i} = \frac{\sum_j^{V} \chi_{g,j} \sum_{g'=1}^{ng} \nu\Sigma_{f,g',j}\phi_{g',j}V_j}{\sum_j^{V} \sum_{g'=1}^{ng} \nu\Sigma_{f,g',j}\phi_{g',j}V_j} \tag{2.5}$$

where

ng: The number of fine energy groups,

$\bar{\chi}_{g,i}$: Homogenized Chi spectrum of group *g* at pin index *i*,

$\chi_{g,j}$: Chi spectrum of group *g* at sub region *j*,

$\bar{\psi}_i$: Homogenized fission source at pin index *i*,

ψ_j: Fission source at sub region *j*.

The energy group condensation is similarly processed as preserving the reaction rates of the fine energy groups as shown in the Eq. (2.6) and (2.7).

$$\bar{\Sigma}_{x,G}\bar{\varphi}_G = \bar{\Sigma}_{x,G}\sum_{g\in G}\bar{\phi}_g = \sum_{g\in G}\bar{\Sigma}_{x,g}\bar{\phi}_g \tag{2.6}$$

$$\bar{\Sigma}_{x,G} = \frac{\sum_{g\in G}\bar{\Sigma}_{x,g}\bar{\phi}_g}{\sum_{g\in G}\bar{\phi}_g} \tag{2.7}$$

where

$\bar{\Sigma}_{x,G}$: Pin-wise coarse-group homogenized cross-section of reaction *x*, coarse-group *G*.

The scattering cross-section and fission spectrum are condensed as Eq. (2.8) and (2.9).

$$\bar{\Sigma}_{G'\to G} = \frac{\sum_{g'\in G'}\sum_{g\in G}\bar{\Sigma}_{g'\to g}\bar{\phi}_{g'}}{\sum_{g'\in G'}\bar{\phi}_{g'}} \tag{2.8}$$

$$\bar{\chi}_G = \sum_{g\in G}\bar{\chi}_g \tag{2.9}$$

where

$\bar{\Sigma}_{G'\to G}$: Pin-wise coarse-group homogenized scattering cross-section from *G'* to *G*,

$\bar{\chi}_G$: Pin-wise coarse-group fission spectrum of coarse-group *G*.

The coarse-group diffusion coefficient is generated with condensation of the fine group diffusion coefficient.

2.3. Volume Adjustment

The fuel assembly considered in the lattice calculation contains water gap as well as square fuel cells. In this work, the water gap is smeared into the peripheral cells as shown in Figure 2.1.

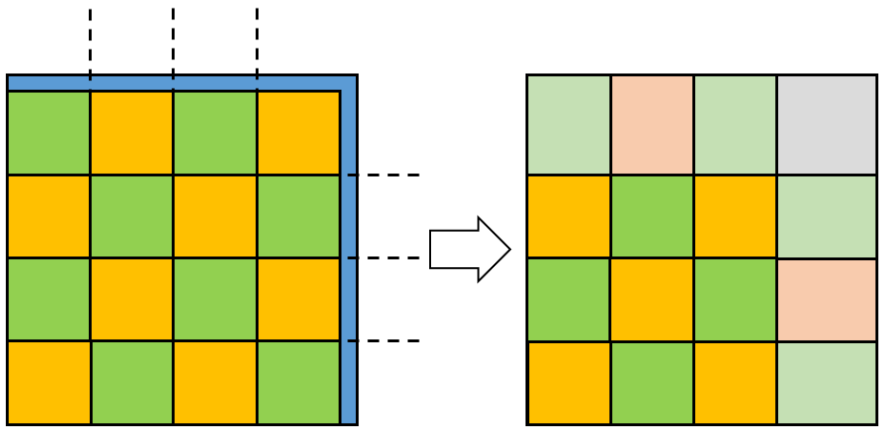

Figure 2.1 Process to smear water gaps into the peripheral pins

Sizes of peripheral cells become different from the normal cells. Instead of model the different sizes as itself, the volume adjustment is introduced for simplifying the core calculation. Once the volumes of peripheral pins are changed to that of the normal pins, all the variables should be adjusted to the same volume. First of all, material densities are modified to preserve masses as the Eq. (2.10).

$$\rho_i^{'} = \rho_i \frac{V_i}{V_i^{'}} \tag{2.10}$$

where

$\rho_i^{'}$: Adjusted material density at region *i*,

ρ_i: Original material density at region *i*,

$V_i^{'}$: Adjusted material volume at region *i*,

V_i: Original material volume at region *i*.

The group-wise flux is also adjusted to preserve the original flux as Eq. (2.11).

$$\phi_{i,g}' = \phi_{i,g} \frac{V_i}{V_i'} \tag{2.11}$$

where,

$\phi_{i,g}^{'}$: Adjusted neutron flux of group *g* at region *i*,

$\phi_{i,g}$: Original neutron flux of group *g* at region *i*.

With the modified flux and density, microscopic cross-sections are modified to preserve reaction rates as Eq. (2.12) and (2.13).

$$\rho_{x,i}' \sigma_{x,i,g}' \phi_{i,g}' V_i' = \rho_{x,i} \sigma_{x,i,g} \phi_{i,g} V_i \tag{2.12}$$

$$\sigma_{x,g,i}' = \sigma_{x,g,i} \frac{\rho_{x,i} \phi_{i,g} V_i}{\rho_{x,i}' \phi_{i,g}' V_i'} = \sigma_{x,i,g} \frac{V_i'}{V_i} \tag{2.13}$$

where

$\sigma'_{x,i,g}$:Adjusted microscopic cross-section of reaction *x*, group *g* at region *i*,

$\sigma_{x,i,g}$:Original microscopic cross-section of reaction *x*, group *g* at region *i*.

Therefore, the modified densities and microscopic cross-sections are used in the core calculation with one size for all cells.

2.4. Pin-wise equivalence factors

As following the conventional two-step calculation procedure, the second step which is composed of the nodal and pin power reconstruction calculations reproduces solutions of lattice calculations for two-dimensional single assembly problems because all the group constants are homogenized as preserving reaction rates and leakages at surfaces of the assembly are zero due to the reflective boundary condition. However, the pin-wise fine mesh calculation with pin-wise homogeneous group constants does not preserve solutions of lattice calculations because the surface currents at pin surfaces are not reproduced. Therefore, pin-wise solutions should have additional errors not shown in the assembly-wise homogeneous calculation because of the low-order approximation. Moreover, there is a practical issue that is the difference of pin powers should be additionally assessed and included to the bias/uncertainty in nuclear design process. In order to resolve the mismatch, the pin-wise equivalence factors are needed to make the solutions of pin-wise fine mesh calculation same to the lattice solution. There are two typical ways to preserving surface leakages as well as average reaction rates.

The first one is the surface discontinuity factor introduced in the equivalence theory [14]. In this theory, the surface flux discontinuity is allowed to preserve surface leakages so that the pin-wise nodal balance for all pins should be preserved. As shown in the Figure 2.2, the homogenous surface

flux shown as the blue line is continuous between left and right nodes.

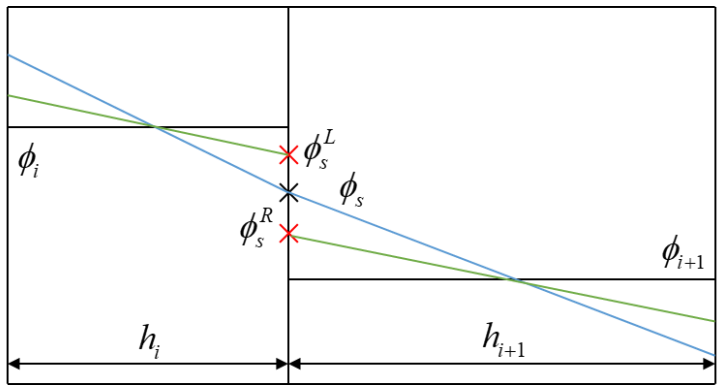

Figure 2.2 Flux discontinuity in the equivalence theory

At this black point, the net current is different from the heterogeneous current and the condition of the nodal balance is not satisfied. With the appropriate discontinuity factors, the surface flux becomes discontinuous (green line) and the current becomes identical to the heterogeneous current as preserving the nodal balance.

The homogenous surface flux is determined by the fine mesh calculation and the homogeneous surface current and flux are calculated with the flux and current continuity conditions as the following equations.

$$\phi_s = \frac{\beta_{i+1}\phi_{i+1} + \beta_i\phi_i}{\beta_{i+1} + \beta_i} \tag{2.14}$$

$$J_{hom} = \frac{\beta_{i+1}\beta_i}{\beta_{i+1} + \beta_i}(\phi_{i+1} - \phi_i) \quad (2.15)$$

where

J_{hom}: Surface current,

ϕ_s: Homogenous surface flux,

β_i: Diffusion coefficient per unit length at node *i*, ($\frac{D_i}{h_i}$),

ϕ_i: Average flux at node *i*.

In order to preserve the heterogeneous current, the surface discontinuity factor is adopted as the following equation. The surface flux multiplied by the discontinuity factor is called the heterogeneous surface flux.

$$f_L\phi_s^L = \phi_s^{het} = f_R\phi_s^R \quad (2.16)$$

where

f_L: Discontinuity factor from left side of surface,

f_R: Discontinuity factor from right side of surface.

Then, the heterogeneous surface current and flux are redefined with the discontinuity factor as the following equation. This means the heterogeneous surface flux, instead of the homogeneous surface flux, is continuous.

$$\phi_s^{het} = \frac{\beta_{i+1}\phi_{i+1} + \beta_i\phi_i}{\frac{\beta_{i+1}}{f_R} + \frac{\beta_i}{f_L}} \tag{2.17}$$

$$J_{het} = -D_i \frac{\phi_s^L - \phi_i}{\frac{h_i}{2}} = -D_{i+1} \frac{\phi_{i+1} - \phi_s^R}{\frac{h_{i+1}}{2}} \tag{2.18}$$

With the above two equations and substituting the surface flux $\phi_s^{L,R}$ with $\frac{\phi_s^{het}}{f_{L,R}}$, the final form of the current is shown as the following.

$$J_{het} = -2 \frac{\left(\frac{\beta_{i+1}}{f_R}\right)\left(\frac{\beta_i}{f_L}\right)}{\left(\frac{\beta_{i+1}}{f_R}\right) + \left(\frac{\beta_i}{f_L}\right)} (\phi_{i+1} f_R - \phi_i f_L) \tag{2.19}$$

With the homogeneous surface flux calculated from the heterogeneous average fluxes and the heterogeneous surface currents, the discontinuity factors are calculated as solving Eq. (2.18)2.19 and Eq. (2.19). Using the discontinuity factors, the fine mesh calculation exactly reproduces the results of the lattice calculation. Since the discontinuity factor is dependent on each surface of the problem, the two-dimensional problem should explicitly have 4N of discontinuity factors. It requires additional memory storage and computing time.

The other equivalence factor is the SPH factor introduced in the super homogenization method [15]. The factor is defined as the ratio of the heterogeneous flux to the homogeneous flux as shown in the Eq. (2.20) and it is same to the ratio of the heterogeneous reaction rate to the homogeneous value because of the homogenization process. Different from the discontinuity factor which is defined for every surface, the SPH factor is defined for every node.

$$\mu_g = \frac{\bar{\phi}^*_g}{\bar{\phi}_g} \tag{2.20}$$

where

μ_i: SPH correction factor of group g,

$\bar{\phi}^*_g$: Average flux of group g obtained by the heterogeneous calculation,

$\bar{\phi}_g$: Average flux of group g obtained by the pin-homogeneous calculation using SPH corrected cross-section.

Once the SPH factor is obtained after the homogeneous pin-by-pin calculation, the homogeneous cross-sections are changed by multiplying the SPH factors to preserving the heterogeneous reaction rates. As repeating the homogeneous calculations following the cross-section change, the SPH factors are converged and the heterogeneous reaction rates and sum of the

heterogeneous surface currents of each node are preserved.

Compared to the reference solutions, the flux value is shifted to the ϕ_g^* by the SPH factor. Different from the discontinuity factor, the SPH factor only preserves node average values of the reaction rates and sum of the surface currents. The advantage of the SPH method is that additional computing resources are not required because the SPH factor is incorporated into the cross-sections by following the next equation.

$$\Sigma_g = \Sigma_g^* \mu_g \tag{2.21}$$

The overall calculation process of the SPH factor is shown in the Figure 2.3. The comparison of the equivalence theory and the super homogenization method is shown in the section 3.1.

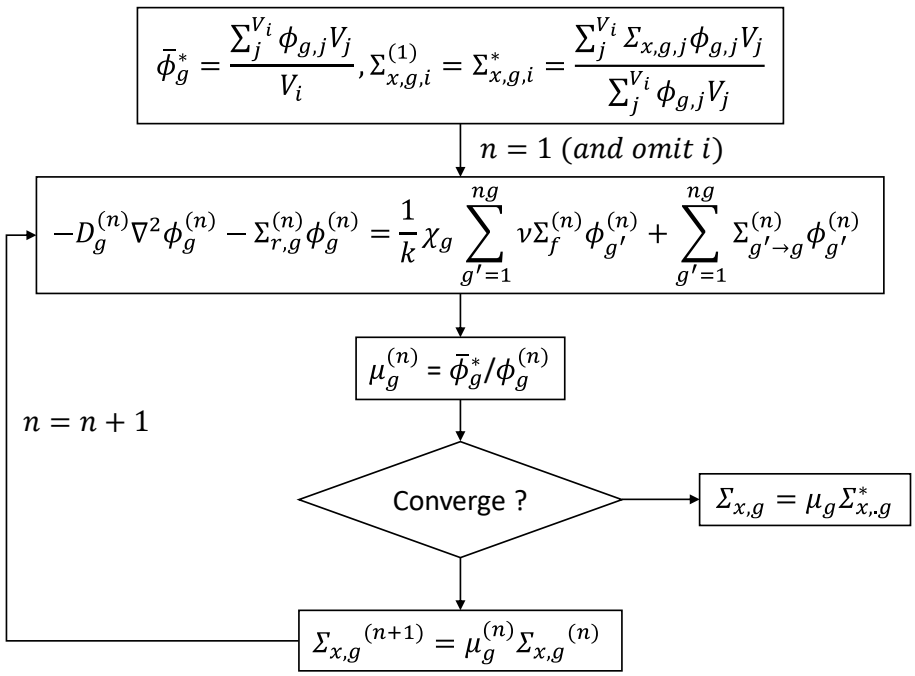

Figure 2.3 Neutronics calculation process to determine the SPH factor

2.5. 3D pin-wise calculation with 2D/1D decoupling method

The three-dimensional pin-wise neutronics calculations of commercial reactor cores are still impractical since too much calculation time is required. Over fifty thousand of fuel pins, 30~40 axial planes, a few energy groups should be considered for the commercial reactor core calculations. That means the solution vectors have a scale of millions. Even though the efficient linear system solvers based on Krylov subspace methods are utilized, it is not applicable to solve the huge linear systems directly. Therefore, the planar decoupling method is chosen as a practical way of domain decompositions because the number of planes is around 30~40, which is suitable for parallelization of the multicore system.

In this work, the finite difference method is basically used as a solver of three-dimensional neutron diffusion equation. Generally, representing each pincell to one mesh is not sufficient to achieve desirable accuracy in finite difference calculation. However, If the SPH factor described in the previous chapter is generated from the finite difference calculation with geometry of the one mesh per pin, it can also compensate errors coming from the large mesh size. Therefore, the geometry with a mesh per pin is consistently used in this work.

The three-dimensional pin-by-pin diffusion equation with the finite difference method is shown in the following equation.

$$\sum_{u=x,y,z} \frac{1}{h_u}\left(J_{gu}^{R} - J_{gu}^{L}\right) + \Sigma_{rg}\bar{\phi}_g = \frac{\chi_g}{k_{eff}} \sum_{g'=1}^{G} \nu\Sigma_{fg'}\bar{\phi}_{g'} + \sum_{\substack{g'=1 \\ g' \neq g}}^{G} \Sigma_{g'g}\bar{\phi}_{g'} \quad (2.22)$$

In order for the plane-wise domain decomposition, the axial current term of the Eq. (2.22) is simply moved to the right-hand side and it is treated as a source term of Eq. (2.23).

$$\sum_{u=x,y} \frac{1}{h_u}\left(J_{gu}^{R} - J_{gu}^{L}\right) + \Sigma_{rg}\bar{\phi}_g = \frac{\chi_g}{k_{eff}} \sum_{g'=1}^{G} \nu\Sigma_{fg'}\bar{\phi}_{g'} + \sum_{\substack{g'=1 \\ g' \neq g}}^{G} \Sigma_{g'g}\bar{\phi}_{g'} - \frac{1}{h_z}\left(J_{gz}^{R} - J_{gz}^{L}\right) \quad (2.23)$$

where

J_{gu}^{R}: u-direction neutron surface current from east side surface,

J_{gu}^{L} u-direction current surface current from west side surface,

χ_g: Neutron fission spectrum.

Then, the 3D neutron balance equation is decoupled into a set of 2D neutron balance equations and each of the 2D equations is independently solved for each plane. It is noted that the axial current term should be independently

determined with additional calculations.

Like the 2D calculation, the 3D neutron balance equation is divided into a set of 1D neutron balance equations as the radial current term is moved to the right-hand side. The 1D equation is expressed as Eq. (2.24).

$$\frac{1}{h_z}\left(J_{gz}^{R}-J_{gz}^{L}\right)+\Sigma_{rg}\bar{\phi}_g = \frac{\chi_g}{k_{eff}}\sum_{g'=1}^{G}\nu\Sigma_{fg'}\bar{\phi}_{g'}+\sum_{\substack{g'=1\\ g'\neq g}}^{G}\Sigma_{g'g}\bar{\phi}_{g'}-\sum_{u=x,y}\frac{1}{h_u}\left(J_{gu}^{R}-J_{gu}^{L}\right) \qquad (2.24)$$

This equation is established for each fuel rod and decoupled with one another. The 2D/1D decoupling calculation produces the essentially same solution to the solution of typical 3D fine mesh calculation.

In case of the 2D equation, the mesh size is sufficiently small about 1~2cm to achieve reasonably accurate solutions since the spatial errors diminish with the SPH factors. However, the axial mesh size of 1D equation about tens of centimeters is not small to get the accurate solution with the typical finite difference calculation. Improving the accuracy of axial calculations has been done in several researches of the whole core transport calculation as adopting the nodal or fine mesh calculations. In the recent research [16], the fine mesh calculation with dividing the axial coarse mesh

into a set of around 1cm fine meshes are incorporated. For the 1D fine mesh calculation, the radial leakage of the coarse mesh is represented as a second order polynomial function using the three radial leakages of upper, lower and self-nodes as shown in Figure 2.4 and the radial leakages of the fine meshes are determined with partial integration of the function.

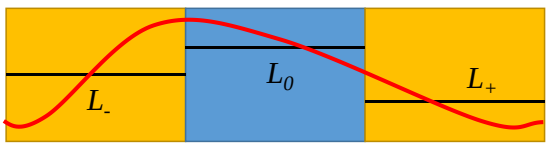

Figure 2.4. Approximation of the transverse radial leakage

As the radial leakage is moving to the right-hand side, we obtain the fine mesh 1D equation as shown in the following equation.

$$\frac{1}{h_z}\left(J_{gz}^{R}-J_{gz}^{L}\right)+\Sigma_{rg}\bar{\phi}_g=\frac{\chi_g}{k_{eff}}\sum_{g'=1}^{G}\nu\Sigma_{fg'}\bar{\phi}_{g'}+\sum_{\substack{g'=1\\ g'\neq g}}^{G}\Sigma_{g'g}\bar{\phi}_{g'}-\sum_{u=x,y}\sum_{i=0}c_iP_i(u) \qquad (2.25)$$

Once the 1D finite difference formulation is constructed and solved, the axial surface currents are obtained and they are used as source term in the 2D planar equation. Repeating the 2D and 1D finite difference calculations, the 3D solution should be obtained.

2.6. Two-level CMFD acceleration

The pin-wise 2D/1D decoupling method takes long computing time though the plane-wise parallelization is adopted since the number of meshes is too large. In order to accelerate the calculation, the two-level CMFD calculation [1] is introduced. In the reference, the first-level CMFD calculation has a role of determining the node-wise and multi-group global solutions such as k-eff and flux distribution with the nodal correction factor and the second level CMFD accelerates the first-level CMFD calculation as condensing the multi-group structure to the two-group structure. The first-level CMFD is essential because it iteratively updates solutions instead of the nodal calculation. The idea of the original two-level CMFD calculation is slightly changed in this work. Since the 2D/1D decoupling method is able to determine the solutions by itself, the role of the first one is changed to accelerate the pin-wise calculation as homogenizing the pin-wise geometry into the assembly-wise one and improve the iteration stability as keeping the multi-group structure. And the second CMFD accelerates the first CMFD calculation as condensing the multi-group structure into two-group structure.

For the first-level CMFD calculation, the pin-wise cross-sections are homogenized with the current pin-wise flux as preserving the assembly reaction rates as shown in Eq. (2.26).

$$\bar{\Sigma}_{xg}^{i} = \frac{\sum_{k \in i} V_k \Sigma_{xg}^{k} \phi_g^k}{\bar{\varphi}_g^i V_i} \tag{2.26}$$

where

$\bar{\Sigma}_{xg}^{i}$: Homogenized cross-section of reaction x , group g at pin index i,

$\bar{\phi}_g^i$: Pin average neutron flux of group g, pin index i ,

V_i: Total volume of pin index i .

The current of the CMFD formulation is defined as Eq. (2.27).

$$J_g^{cmfd} = -\widetilde{D}_g\left(\bar{\phi}_g^r - \bar{\phi}_g^l\right) - \widehat{D}_g\left(\bar{\phi}_g^r - \bar{\phi}_g^l\right) \tag{2.27}$$

where

J_g^{cmfd}: Net current of the CMFD,

$\widetilde{D}_g$: Modified diffusion coefficient,

$\widehat{D}_g$: CMFD correction factor,

$\bar{\phi}_g^r$,$\bar{\phi}_g^l$: Neutron flux from right and left side of mesh (on the basis of boundary surface).

It is noted that the variables of the above equation are defined for an assembly not a fuel pin. The reference current is calculated by averaging the pin-wise current along the assembly surface. Then, the correction factor is given by Eq.

(2.28).

$$\widehat{D}_g = \frac{J_g + \widetilde{D}_g\left(\bar{\phi}_g^r - \bar{\phi}_g^l\right)}{\bar{\phi}_g^r + \phi_g^l} \tag{2.28}$$

where

J_g : Neutron current which is obtained from solving diffusion equation.

Once the first-level CMFD calculation is done, the multi-group cross-sections and flux are condensed to the two-group values as shown in the Eq. (2.29) and (2.30).

$$\bar{\phi}_G = \sum_{g \in G} \bar{\phi}_g \tag{2.29}$$

$$\Sigma_{x,G} = \sum_{g \in G} \frac{\bar{\phi}_g}{\bar{\phi}_G} \Sigma_{x,g} \tag{2.30}$$

where

$\bar{\phi}_G$: Two-group assembly-wise neutron flux of group G,

$\bar{\phi}_g$: Multi-group assembly-wise neutron flux of group g,

$\Sigma_{x,G}$: Two-group cross-section of reaction x, group G,

$\Sigma_{x,g}$: Multi-group cross-section of reaction x, group g.

And, the correction factor of the second-level CMFD is obtained as shown in the Eq. (2.31).

$$\widehat{D}_G = \frac{\sum_{g\in G} J_g + \widetilde{D}_g\left(\phi_G^r - \phi_G^l\right)}{\left(\phi_G^r + \phi_G^l\right)} \tag{2.31}$$

where

$\widetilde{D}_G$: Two-group CMFD diffusion coefficient.

Once the second-level CMFD calculation is done with the two-group values, the two-group solution is expanded to the multi-group for the first-level CMFD calculation as the Eq. (2.32). In the process, the previous multi-group solution is simply used.

$$\phi_g^{(n)} = \frac{\phi_G}{\sum_{g\in G} \phi_g^{(n-1)}} \phi_g^{(n-1)} \tag{2.32}$$

After finishing the first-level CMFD calculation with the expanded solution, the assembly-wise multi-group flux is obtained. It is expanded into the pin-wise flux for the pin-wise calculation with the previous pin-wise flux as shown in the Eq. (2.33).

$$\phi_{g,k}^{(n)} = \frac{\bar{\phi}_{g,i}^{(n)}}{\sum_{k\in i} V_k \bar{\varphi}_g^{n-1}} \phi_{g,k}^{(n-1)} \qquad (2.33)$$

where

$\bar{\phi}_{g,i}^{(n)}$: Assembly-wise neutron flux of index i, group g in nth CMFD iteration,

$\phi_{g,k}^{(n)}$: Pin-wise neutron flux of pin index k, group g in nth CMFD iteration.

The overall procedure of the two-level CMFD calculation is shown in the Figure 2.5.

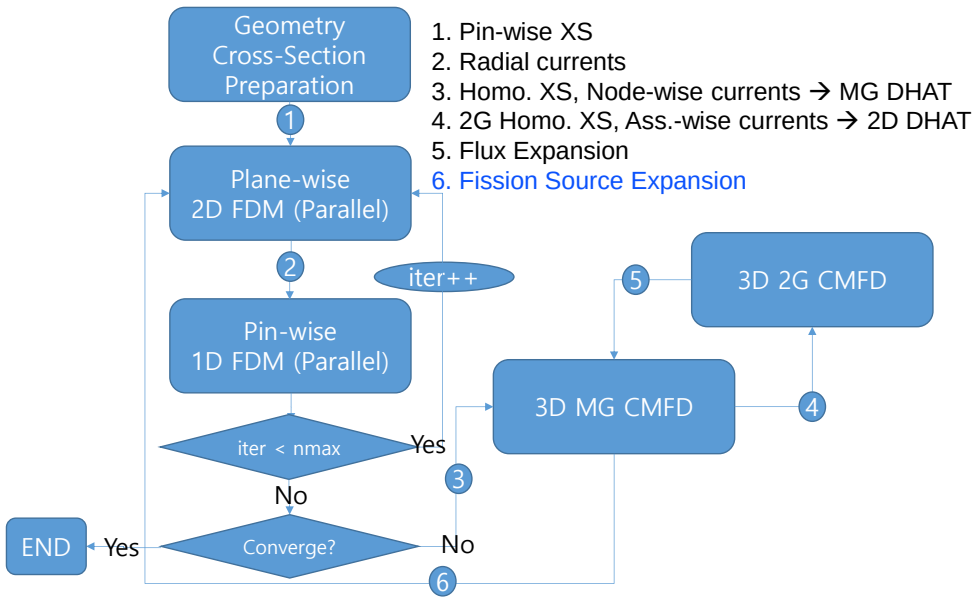

Figure 2.5 Pin-wise calculation based on two-level CMFD acceleration

2.7. Transient Calculation

The multi-group pin-wise transient calculation also begins with the spatially discretized time-dependent neutron and precursor balance equations. The matrix form of spatially discretized balance equations is given simply as follows.

$$\frac{1}{v_g}\frac{d\boldsymbol{\phi}_g(t)}{dt} = \boldsymbol{s}_g(t) - \boldsymbol{L}_g(t)\boldsymbol{\phi}_g(t) \tag{2.34}$$

$$\frac{1}{v_g}\frac{d\boldsymbol{C}_k(t)}{dt} = \boldsymbol{\beta_k}\boldsymbol{\Psi}(t) - \lambda_k\boldsymbol{C}_k(t) \tag{2.35}$$

where $\boldsymbol{\phi}_g(t)$, $\boldsymbol{\Psi}(t)$, $\boldsymbol{C}_k$ are vectors consisting of the flux, fission source and precursor density, respectively. $\boldsymbol{s}_g(t)$ is a vector consisting of transient source terms given as:

$$s_g^m(t) = \chi_{pg}\big(1-\beta^m(t)\big)\Psi^m(t) + \sum_{k=1}^{6}\chi_{dgk}\lambda_k C_k^m(t) + \sum_{g=1}^{G}\Sigma_{g'g}^m\phi_g^m(t) \tag{2.36}$$

with *m, g and k* being the indices for node, energy group and delayed neutron group, respectively. v_g is the velocity of group g. $\boldsymbol{\beta_k}$ and λ_k are vectors for delayed neutron fraction and the decay constant of the k-th delayed

neutron group, respectively. χ_{pg} and χ_{dgk} are prompt and delayed neutron emission yields which should be different in the multigroup formulation. $\boldsymbol{L}_g(t)$ is a loss matrix consisting of the leakage and removal terms.

Temporal discretization performed with the theta method yields the following transient fixed source problem:

$$\left(L_g^{n+1}+\frac{1}{\theta v_g \Delta t}I\right)\phi_g^{n+1}-s_g^{n+1}=\frac{1}{\theta v_g \Delta t}\phi_g^{n}-\frac{\bar{\theta}}{\theta}\left(s_g^{n}-L_g^{n}\phi_g^{n}\right) \quad (2.37)$$

where n is the time point index and $\bar{\theta}=1-\theta$. Since s_g^{n+1} which includes the delayed neutron source term is coupled with the precursor balance equations, the precursor balance equation has to be solved before solving the above equation. The precursor balance equation can be solved analytically as long as the temporal variation of the fission source is assumed to be known. By introducing a second order temporal variation on the fission source in terms of three time point values, the precursor density at the new time point is given in terms of the fission sources of three-time points.

$$C_k^{m,n+1}=\kappa_k C_k^{m,n}+\frac{\beta_k^{m,n}}{\lambda_k}\left(\Omega_k^{n-1}\psi^{m,n-1}+\Omega_k^{n}\psi^{m,n}+\Omega_k^{n+1}\psi^{m,n+1}\right) (2.38)$$

where the Ω_k^n is a coefficient for the contribution of fission source of time point n that is given in terms of the time step size and the decay constant. The definition of these coefficients and some other terms which are not explicitly defined in the following can be found in the PARCS manual [4]. Inserting Eq. (2.38) and (2.39) into the delayed neutron source term of Eq. (2.37) yields

$$\begin{aligned} s_d^{m,n+1} &\equiv \sum_{k=1}^{6} \chi_{dgk} \lambda_k C_k^{m,n+1} \\ &= \sum_{k=1}^{6} \chi_{dgk} \left(\lambda_k \kappa_k C_k^{m,n} + \beta_k^{m,n} \left(\Omega_k^{n-1} \psi^{m,n-1} + \Omega_k^n \psi^{m,n} + \Omega_k^{n+1} \psi^{m,n+1} \right) \right) \\ &= \tilde{s}_{dg}^{m,n} + \omega_g^{n+1} \psi^{m,n+1} \end{aligned} \tag{2.39}$$

where

$$\tilde{s}_{dg}^{m,n} = \sum_{k=1}^{6} \chi_{dgk} \left(\lambda_k \kappa_k C_k^{m,n} + \beta_k^{m,n} \left(\Omega_k^{n-1} \psi^{m,n-1} + \Omega_k^n \psi^{m,n} \right) \right),$$

$$\omega_g^{m,n+1} = \sum_{k=1}^{6} \chi_{dgk} \beta_k^{m,n} \Omega_k^{n+1}.$$

Since the transient fixed source problem is then recast into the following linear system:

$$\left(L_g^{n+1}+\frac{1}{\theta v_g \Delta t}I\right)\varphi_g^{n+1}-\left(S_g+F_g\right)\begin{bmatrix}\varphi_1^{n+1}\\ \vdots \\ \varphi_G^{n+1}\end{bmatrix}$$
$$=\mathrm{s}\tilde{}_{dg}^{n}+\frac{1}{\theta v_g \Delta t}\varphi_g^n-\frac{\bar{\theta}}{\theta}\left(s_g^n(t)-L_g^n(t)\varphi_g^n(t)\right)\equiv s_g^n \qquad (2.40)$$

where

$$S_g=[diag(\Sigma_{1g}^m),\cdots,diag(\Sigma_{Gg}^m)]\ ,$$
$$F_g=diag\left(\chi_g(1-\beta_m^{n+1})+\omega_g^{n+1}\right)[diag(\nu\Sigma_{f1}^m),\cdots,diag(\nu\Sigma_{fG}^m)]$$

and $diag(a_m)$ is a *M X M* diagonal matrix containing a_i at the i[th] diagonal position. The form of the transient linear system is almost same to the static linear system except the additional term of time differencing. Practically, the routines of the static calculation are utilized for the transient calculating as adding the additional term into the diagonal elements of loss matrix.

3. Assessment

3.1. Discontinuity Factor vs SPH Factor

In this section, the accuracy of the discontinuity factor and SPH factor is evaluated. As described in the previous chapter, the discontinuity factor exactly preserves each of the heterogeneous currents whereas the SPH factor preserves the node-wise sum of the currents. With this difference, the discontinuity factor should give the more exact solutions, numerically. In the two-step core calculation procedure, there is uncountable error originated from not knowing the neighbor assemblies while generating the pin-wise cross-sections of each assembly. Because of the unknown information, it is not promised that the discontinuity factor always gives better solution than the SPH factor. In order to investigate the accuracy of the discontinuity factor and the SPH factor, the simple 2X2 checkerboard problems are prepared. The geometry of assemblies is described in the Figure 3.1. The UO2 enrichments of the assemblies A0 and C0 are 1.71 w/o and 3.64 w/o, respectively. The multiplication factors of the assemblies A0 and C0 are 1.08943 and 1.30156.

The neutron transport code nTRACER has been developed by cooperation of SNU and KNF and solves three-dimensional problems with the 2D/1D decoupling method. The radially two-dimensional numerical method is the method of characteristics and the axially one-dimensional method is the source expansion nodal method. The nTRACER is used to

generate the reference solution and the pin-by-pin cross-sections for the checkerboard problem.

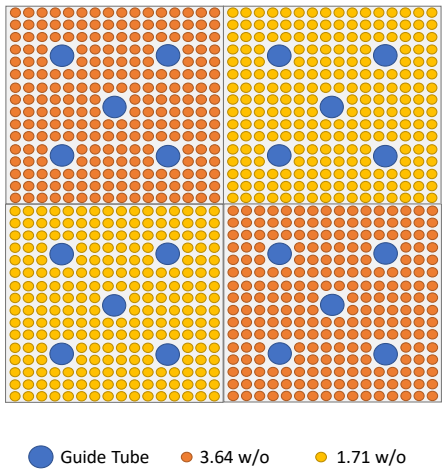

Figure 3.1. Geometry of the checkboard problem

First of all, the checkerboard problem is solved without any equivalence factor. In this case, two sets of cross-sections are generated from the single assembly calculations and the checkerboard calculation of nTRACER. As shown in Table 3-1, using checkboard cross-sections obviously gives more accurate results of multiplication factor and pin power distribution than using the single assembly calculation as it is expected.

Table 3-1 Reactivity and RMS errors of the A0C0 checkboard problem

	k-eff	Δk (pcm)	RMS (%)
Reference	1.11600	-	-
Single Assembly XS	1.11777	177	0.96
Checkerboard XS	1.11685	85	0.42

In detail, Figure 3.2 shows the pin power errors with the sets of cross-sections. In the case of single assembly cross-sections as shown in the left figure, the errors are quite large at both of center and periphery of assemblies. However, using the checkboard cross-sections as shown in the right figure shows better solutions than using the single assembly calculation. It is noted that the error is not negligible due to the inaccurate leakage even though the homogenous cross-sections are generated for the specific problem.

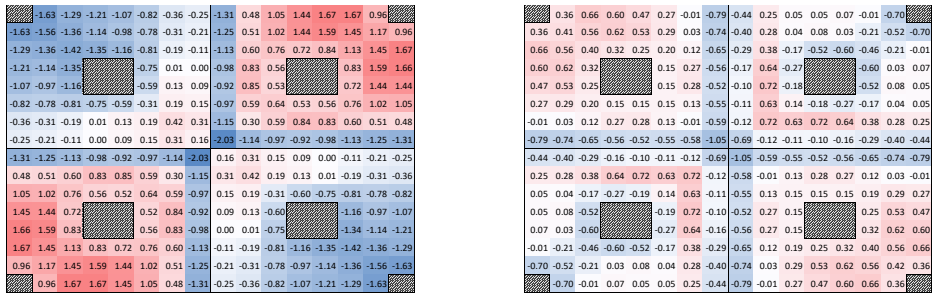

<Single Assembly XS> <Checkerboard XS>

Figure 3.2 Pin power errors with single and checkerboard XS

In order to reduce the error, the equivalence factors are introduced. The discontinuity factors and SPH factors are generated as well as the pin-wise

cross-sections with the heterogeneous single assembly calculation. Table 3-2 shows the errors of multiplication factor and pin power distribution. In this table, it is observed that using the SPH factor shows slightly better solutions. Figure 3.3 shows the pin power error distributions of using the discontinuity factors and SPH factors. In case of using the discontinuity factors as shown in the left figure, the pin power errors are small in the inner region of assemblies but the errors are not reduced and rather increased at the assembly interfaces. The reason is that the discontinuity factors are also generated from single assembly calculations with the reflective boundary conditions instead of actual boundary conditions which are not known. On the other hand, the case using the SPH factors shows good agreement of pin powers at the assembly interfaces as shown in the right figure. Since the SPH factor make an effect on all pin surfaces surrounding pins, the pin power near the assembly interfaces also slightly improved with the adjacent pins.

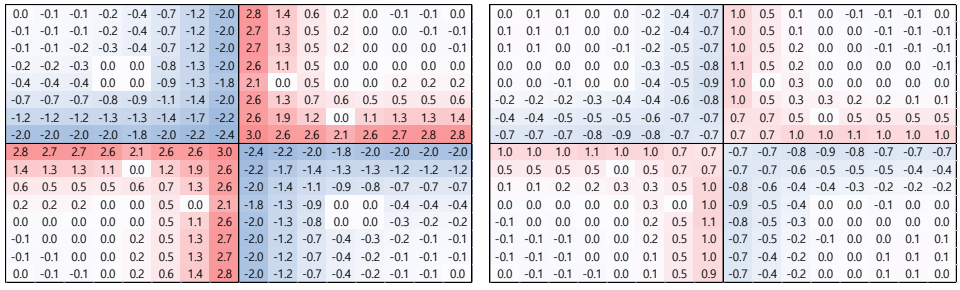

Figure 3.3 Pin power errors with discontinuity (L) and SPH factors (R)

Table 3-2 Reactivity and RMS errors of the A0C0 checkboard problem with the equivalence factors

	k-eff	$\Delta\rho$ (pcm)	RMS (%)
Reference	1.00450		
Discontinuity Factor	1.00496	46	1.36
SPH Factor	1.00460	10	0.50

Likewise, Table 3-3 shows various checkboard problems with the nine assemblies with difference energy group structures and equivalence factors. In the table, the results of the SPH factor shows the competitive accuracy of the multiplication factors and pin power distributions as comparing them of the discontinuity factor. Additionally, the four-group and eight-group structures show the slightly better solutions than two-group structure. Based on the comparing results, the SPH factor and coarse-group (4G or 8G) structures are suggested for upcoming benchmark problems.

Table 3-3 Reactivity and RMS errors of the checkboard problems

Problem	Δρ (pcm)						RMS Error of Pin Power Dist. (%)						MAX Error of Pin Power Dist. (%)					
	2G		4G		8G		2G		4G		8G		2G		4G		8G	
	PDF[1)]	SPH[2)]	PDF	SPH	PDF	SPH	PDF	SPH	PDF	SPH	PDF	SPH	PDF	SPH	PDF	SPH	PDF	SPH
A0B0	14.1	56.9	-38.4	5.7	-65.7	-17.3	0.86	0.74	0.76	0.21	0.92	0.40	1.84	-1.34	1.80	-0.59	1.48	0.65
A0B1	-48.8	-34.8	-50.3	-37.0	-32.2	-18.5	1.00	0.41	0.97	0.27	1.01	0.25	-2.12	-0.83	-2.01	-0.70	1.79	0.33
A0B2	-34.3	-29.3	-35.9	-32.0	-21.0	-18.9	0.88	0.36	0.86	0.24	0.86	0.24	-1.94	-0.76	-1.86	-0.67	1.59	0.35
A0B3	-47.3	-41.2	-45.1	-40.1	-17.9	-12.8	1.14	0.38	1.02	0.26	1.03	0.20	-2.21	-0.85	-2.05	-0.67	1.80	-0.38
A0C0	9.6	69.0	-55.3	6.5	-91.1	-22.3	1.03	0.85	0.94	0.25	1.13	0.46	2.11	-1.56	2.09	-0.64	1.73	0.76
A0C1	-63.1	-26.4	-73.2	-36.3	-60.0	-20.3	1.20	0.57	1.18	0.32	1.25	0.33	2.65	-0.99	2.49	-0.82	2.18	0.48
A0C2	-70.7	-38.1	-66.8	-34.6	-40.9	-6.8	1.30	0.51	1.22	0.31	1.27	0.28	2.79	-1.01	2.52	-0.80	2.19	0.41
A0C3	-56.2	-33.4	-53.9	-31.6	-31.2	-9.5	1.18	0.46	1.12	0.29	1.14	0.28	2.63	-0.93	2.38	-0.77	1.99	0.42
B0B1	42.7	26.2	5.9	-11.9	-1.2	-20.3	0.68	0.51	0.22	0.10	0.19	0.22	-1.00	-0.84	-0.72	0.41	-0.54	0.51
B0B2	37.8	27.6	-0.1	-10.6	-10.3	-20.4	0.58	0.53	0.15	0.09	0.25	0.23	-0.96	-0.92	-0.52	0.43	0.59	0.55
B0B3	95.5	66.8	21.0	-9.3	2.6	-26.2	0.91	0.65	0.26	0.14	0.20	0.29	-1.36	-1.08	-0.76	0.58	0.56	0.69
B0C0	-0.8	0.6	-1.6	-0.1	-2.2	-0.4	0.18	0.12	0.17	0.04	0.20	0.06	-0.41	-0.20	-0.37	-0.10	-0.34	0.10
B0C1	20.8	4.2	2.4	-15.5	4.8	-14.6	0.69	0.37	0.39	0.11	0.34	0.13	-1.20	-0.50	-1.06	0.39	0.84	0.34
B0C2	63.2	36.6	20.2	-8.1	16.6	-11.3	0.89	0.49	0.44	0.15	0.36	0.20	-1.36	-0.71	-1.10	0.55	0.86	0.49
B0C3	62.4	39.4	16.6	-7.2	9.6	-12.7	0.78	0.49	0.33	0.13	0.28	0.21	-1.13	-0.78	-0.92	0.50	-0.70	0.52
B1B2	-1.2	-0.5	-0.8	-0.1	-0.6	0.6	0.15	0.07	0.14	0.03	0.17	0.03	-0.29	0.14	-0.23	-0.08	0.27	-0.08
B1B3	14.7	12.2	8.6	5.7	6.4	3.9	0.25	0.15	0.07	0.05	0.03	0.08	-0.34	-0.23	-0.11	0.17	-0.09	0.20
B1C0	51.2	41.1	2.4	-8.1	-13.1	-24.0	0.67	0.60	0.12	0.10	0.24	0.28	-1.16	-1.06	-0.39	0.48	0.52	0.64

B1C1	0.4	3.3	-3.0	0.0	-4.8	-1.4	0.24	0.19	0.20	0.06	0.24	0.10	0.52	-0.32	0.47	0.13	0.37	0.21
B1C2	6.4	8.8	8.6	10.7	9.5	11.4	0.31	0.11	0.25	0.05	0.26	0.04	0.63	0.24	0.49	0.12	-0.41	0.08
B1C3	8.2	8.9	8.8	9.6	9.2	9.7	0.18	0.06	0.14	0.03	0.13	0.04	0.50	0.21	0.38	-0.10	0.30	0.12
B2B3	13.7	9.9	10.2	5.1	9.4	4.7	0.37	0.16	0.21	0.05	0.19	0.07	-0.46	-0.20	-0.30	0.18	-0.26	0.15
B2C0	44.1	42.9	-5.5	-6.2	-24.1	-22.8	0.61	0.63	0.18	0.11	0.38	0.29	-1.12	-1.14	0.57	0.50	0.78	0.69
B2C1	-5.9	1.8	-9.0	-0.8	-10.8	-0.9	0.34	0.24	0.33	0.09	0.40	0.12	0.67	-0.39	0.59	-0.19	0.53	0.25
B2C2	0.6	6.0	5.3	9.9	7.3	12.8	0.45	0.18	0.38	0.08	0.41	0.05	0.80	0.34	-0.64	0.17	-0.57	0.12
B2C3	5.0	7.5	7.4	9.7	8.6	10.6	0.32	0.12	0.26	0.05	0.27	0.04	0.64	0.25	0.50	0.13	-0.41	0.08
B3C0	108.8	87.1	17.7	-4.7	-11.8	-31.3	0.89	0.73	0.14	0.16	0.23	0.36	-1.52	-1.30	-0.44	0.65	0.54	0.83
B3C1	27.2	26.6	6.7	5.9	-2.0	-1.2	0.37	0.32	0.17	0.10	0.22	0.18	-0.62	-0.55	0.45	0.31	0.37	0.41
B3C2	1.5	4.8	-2.6	0.7	-4.9	-1.0	0.24	0.19	0.20	0.06	0.24	0.11	0.53	-0.33	0.47	0.13	0.38	0.21
B3C3	4.1	4.1	0.2	0.0	-1.5	-1.8	0.21	0.17	0.12	0.04	0.11	0.10	-0.41	-0.28	0.36	-0.13	0.29	0.17
C0C1	31.5	17.2	4.3	-10.9	0.3	-16.0	0.62	0.44	0.23	0.10	0.21	0.19	-0.86	-0.72	-0.74	0.36	-0.58	0.44
C0C2	78.5	54.3	21.9	-3.4	9.2	-14.8	0.83	0.56	0.27	0.14	0.22	0.26	-1.17	-0.92	-0.78	0.53	0.60	0.62
C0C3	74.8	56.3	15.5	-2.8	-0.6	-16.0	0.73	0.57	0.19	0.14	0.24	0.27	-1.15	-1.00	-0.60	0.56	0.56	0.67
C1C2	12.9	10.8	8.1	5.8	6.4	4.3	0.23	0.14	0.06	0.05	0.03	0.08	0.31	-0.20	-0.11	0.17	-0.09	0.19
C1C3	11.7	11.7	5.3	5.5	2.7	3.9	0.16	0.16	0.08	0.07	0.13	0.10	-0.27	-0.26	0.20	0.20	0.29	0.24
C2C3	-1.5	-0.9	-1.1	-0.7	-1.1	-0.1	0.14	0.06	0.13	0.03	0.15	0.03	-0.29	0.14	-0.22	0.08	0.25	-0.07

PDF[1)] : Pin-wise Discontinuity Factor

SPH[1)] : SPH Factor

3.2. L336C5 3D Benchmark Problem

The L336 C5 problem was proposed for evaluating the performance of modern whole core transport calculations without spatial homogenization. In this benchmark problem, two-dimensional and three-dimensional configurations are introduced with UO2 and MOX fuel assemblies. As a follow-up to the benchmark, an extension of the three-dimensional problems was developed as considering cases of the control rod insertion for the more difficult calculations. The extension contains three configurations of Unrodded, Rodded A and Rodded B as shown in the Figure 3.5. The assembly-width is 21.42cm and the number of axial planes is 4; three 14.18cm planes for the fuel and one 21.42cm plane for the reflector. The radial and axial configurations of the benchmark problems are shown in the Figure 3.4 and Figure 3.5. And the seven-group macroscopic cross-sections for the fuel-clad of MOX and UO2, the fission chamber, the moderator and the control rod are given in the benchmark specification. In this analysis, the three problems are solved for evaluating the pin-wise core calculation performance.

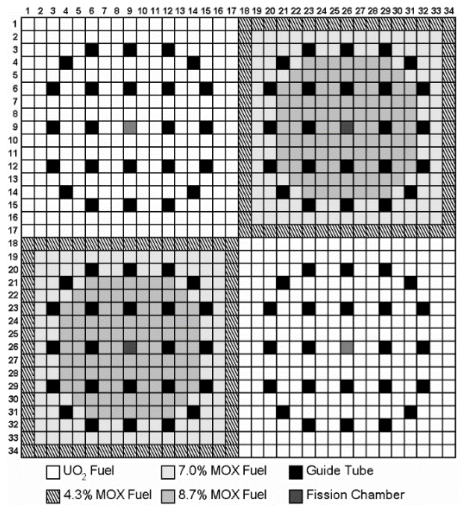

Figure 3.4. Radial configuration of C5G7 MOX benchmark problem

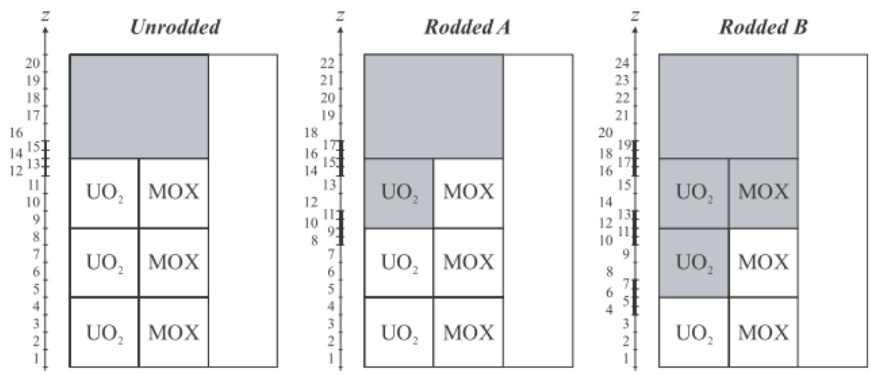

Figure 3.5 Axial configuration (L336C5 extension cases)

The nTRACER code is used to calculate reference solutions and generate the pin-wise homogeneous cross-sections for each assembly. The SPH method described in the previous section is adopted to generate equivalent homogeneous cross-sections. In order to generate reflector cross-

sections, two sets of the assembly-reflector problems are constructed for the edge and corner reflectors as shown in the following figure.

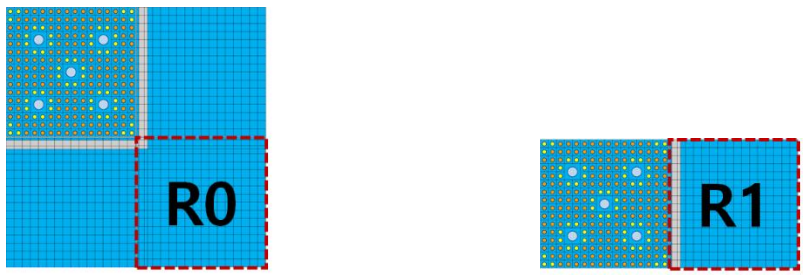

Figure 3.6 Two assembly-reflector problems for L336C5

Once the pin-wise homogeneous cross-sections in which the SPH factors are incorporated are generated, the pin-wise finite difference calculation is performed. Moreover, the conventional nodal calculations with the source expansion nodal method are also performed with two-group and seven-group assembly-wise homogeneous cross-sections and assembly discontinuity factors to assess the accuracy improvement of the pin-wise calculation.

Table 3-4 ~ Table 3-6 show the reference solutions, the nodal solutions and the pin-wise solutions of C5G7 extension cases. The two-group nodal calculations which are the typical way for the PWR core analysis show the quite large errors on the k-eff and power distributions. In the comparison, the pin-wise calculation results show that the reactivity, maximum pin power, pin power distribution errors are drastically reduced. Moreover, the maximum

and RMS errors are constantly about 3 % and 1% regardless of the control rod insertions. That means the pin-by-pin discretization is a good option for minimize the spatial errors.

Table 3-4 Results for the Unrodded case

	K-EFF		Max. Pin Power		Pin Power Distribution	
	Value	Error (pcm)	Value	Error (%)	Max. Error (%)	RMS Error (%)
nTRACER	1.14333	-	2.478	-	-	-
Pin (7G)	1.14253	-61.2	2.461	-0.71	3.23	0.97
Nodal (2G)	1.13986	-265.9	2.564	3.45	10.44	3.14
Nodal (7G)	1.14149	-140.9	2.506	1.12	7.61	2.00

Table 3-5 Results for the Rodded A case

	K-EFF		Max. Pin Power		Pin Power Distribution	
	Value	Error (pcm)	Value	Error (%)	Max. Error (%)	RMS Error (%)
nTRACER	1.12893	-	2.250	-	-	-
Pin (7G)	1.12856	-29.2	2.238	-0.52	3.33	0.88
Nodal (2G)	1.12543	-275.7	2.325	3.34	11.31	3.16
Nodal (7G)	1.12701	-151.3	2.280	1.33	7.60	1.89

Table 3-6 Results for the Rodded B case

	K-EFF		Max. Pin Power		Pin Power Distribution	
	Value	Error (pcm)	Value	Error (%)	Max. Error (%)	RMS Error (%)
nTRACER	1.07907	-	1.836	-	-	-
Pin (7G)	1.07886	-17.5	1.832	-0.22	3.72	0.88
Nodal (2G)	1.07629	-239.0	1.909	4.02	13.20	3.74
Nodal (7G)	1.07692	-185.0	1.887	2.82	10.40	2.77

3.3. VERA Benchmark Problem

The Consortium for Advanced Simulation of Light Water Reactors (CASL) [17] provides 10 benchmark problems based on the Watts Bar Nuclear Power Plant 1 (WBN1) for verification and validation of the modern nuclear physics methods and codes. The WBN1 is the Westinghouse four-loop type and it loads the 193 fuel assemblies for generating 3411 MW of thermal energy. The type of fuel assemblies is Westinghouse 17x17 VANTAGE (V5H) which consists of 264 fuel rods, 24 guide tubes and 1 instrument tube and the eight spacer grids are used to maintain the fuel rod integrity in the assembly. The as-built uranium enrichments of three batches are 2.110 w/o, 2.619 w/o, 3.1000 w/o are used in the benchmark specification and the loading pattern and the control bank positions are shown in the following figure.

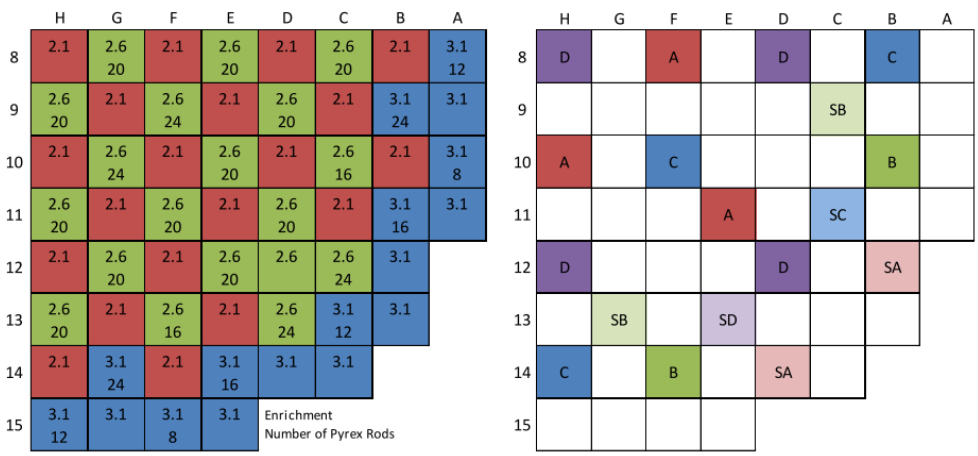

Figure 3.7 Loading pattern and control rod positions of WBN1 cycle1

The benchmark problem consists of the ten problems from a simple 2D pin cell to the full cycle depletion and refueling of a 3D reactor core configuration with control rods and burnable poisons consistent with actual nuclear power plant designs. Among the problems, the fifth problem is three-dimensional hot zero power problem and consists of 32 cases for initial critical test. In this problem, the 22, 27 and 32-th cases of fully inserted RCCA, partially inserted RCCA and all rod-out are chosen to evaluate the performance of pin-wise core calculation.

The reference solutions are generated by the nTRACER three-dimensional calculations at the hot zero power condition. In the nTRACER, the fuel pin cells, assemblies and reflectors are explicitly modeled to precisely verify the problem. In this work, the cross-section library of nTRACER based on the ENDF/B-VII.0 is used.

The homogeneous pin-wise cross-sections are generated for each of 9 assembly types as following the procedure described in the section 0. And the volume correction is applied to considering all the pins having a same size even though there are assembly gaps of which the cell sizes are different from the normal cells as following the section 2.3. And also, The SPH factor is generated and integrated into the homogeneous cross-sections by multiplying cross-sections with the SPH factor to reproduce the reference solution of the nTRACER calculation. The reflector cross-sections are generated with

considering three types of geometry for R0, R1, R2 as shown in the following figure. In the calculations, the volume correction and SPH factor are also incorporated.

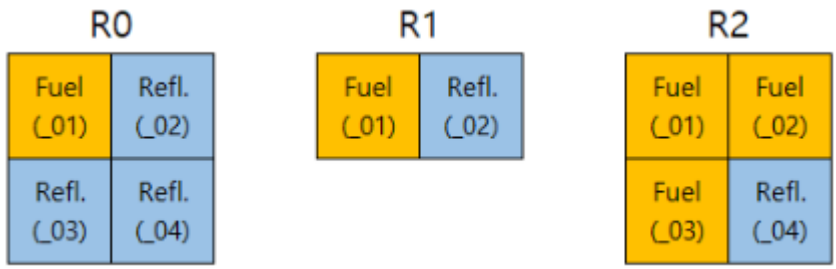

Figure 3.8 Three types of reflector geometry for the VERA benchmark

In order to investigate the accuracy improvement of the pin-wise calculation, the conventional nodal calculations with the assembly-wise homogeneous cross-sections are also performed for the three HZP cases. The detail calculation method and procedure are referred in the previous work [1].

Table 3-7 shows the solutions of the 32th case in which all the control rods are out. The reference eigenvalue of the benchmark book is calculated by KENO-VI and it is 1.006584(+-0.000013). Comparing the result of KENO, the eigenvalue of nTRACER is 1.005966 and the difference is only 62 pcm. This shows the nTRACER has numerically high accuracy to solve the neutronics problems. Since all the group constants are generated by

nTRACER calculations, accuracy can be treated as how close the results of nodal and pin-wise calculations are to the nTRACER results. The nodal solutions are generated from the conventional two-step calculations with energy structures of four- and eight-groups.

In case of the nodal calculation with four-group, the k-eff and maximum pin power errors are -60.5 pcm and 0.17%, but the maximum and RMS errors of the axially integrated radial pin power distribution are 23.97% and 4.95%. These results show the conventional assembly-wise two-step calculation has considerable approximation originated from the inaccurate cross-sections which are generated from the single assembly calculation with reflective boundary condition. Therefore, the spectrum effect of leakage between assemblies cannot be properly reflected in the core calculation.

In case of the pin-wise calculation with four-group, the errors of k-eff and power distributions significantly decreased to -15.6 pcm, -3.76% and 1.63% although the pin-wise cross-sections are generated with the single assembly calculation as same with the nodal calculation. In the pin-wise calculation, the single assembly is divided into pins of 1~2 cm. Thereby, the error caused by the inaccurate leakage between the assemblies can be reduced. This has already been confirmed in the section 3.1.

When comparing the accuracy of calculation by energy condensation, the calculation results of four-group and eight-group are similar. It means that

the pin-wise homogenization with coarse-group (over four-group) structure is reasonably sufficient to represent the spatial heterogeneity of the original problem.

Table 3-8 and Table 3-9 show the solutions of the 27th and 22th cases in which partially inserted RCCA and fully inserted RCCA, respectively. These results also show that the errors of k-eff and power distributions can be reduced by using the pin-wise calculation with the SPH method.

Table 3-7 Calculation results of the 32th case (VERA benchmark)

	K-EFF		Max. Pin Power		Rad. Pin Power Distribution	
	Value	Error (pcm)	Value	Error (%)	MAX Error (%)	RMS Error (%)
Reference (nTRACER)	1.005966	-	1.441	-	-	-
Pin (4G)	1.005808	-15.6	1.443	0.24	-3.76	1.63
Pin (8G)	1.005815	-14.9	1.437	-0.39	-2.80	1.03
Nodal (4G)	1.005354	-60.5	1.443	0.17	23.97	4.95
Nodal (8G)	1.005183	-77.5	1.437	-0.39	23.02	4.06

Table 3-8 Calculation results of the 27th case (VERA benchmark)

	K-EFF		Max. Pin Power		Rad. Pin Power Distribution	
	Value	Error (pcm)	Value	Error (%)	MAX Error (%)	RMS Error (%)
Reference (nTRACER)	1.001961	-	1.444	-	-	-
Pin (4G)	1.001878	-8.3	1.459	1.46	-3.62	1.68
Pin (8G)	1.001854	-10.7	1.463	1.94	-2.68	1.04
Nodal (4G)	1.001473	-48.6	1.515	7.12	30.02	7.94
Nodal (8G)	1.001267	-69.2	1.531	8.75	28.98	7.08

Table 3-9 Calculation results of the 22th case (VERA benchmark)

	K-EFF		Max. Pin Power		Rad. Pin Power Distribution	
	Value	Error (pcm)	Value	Error (%)	MAX Error (%)	RMS Error (%)
Reference (nTRACER)	0.992285	-	1.627	-	-	-
Pin (4G)	0.992414	13.1	1.645	1.79	-3.85	1.93
Pin (8G)	0.992202	-8.5	1.652	2.49	3.29	1.31
Nodal (4G)	0.992263	-2.3	1.657	2.95	32.53	5.98
Nodal (8G)	0.991849	-44.4	1.674	4.68	31.24	4.96

3.4. Small Modular Reactor (BanDi-50) Calculation

The BanDi-50 is one of the small modular reactors generating 180MWth (50MWe) designed by KEPCO E&C in Korea. The 37 17x17 and 2m-long fuel assemblies are loaded in the core in order to satisfy the power specification. Since The detail fuel information and geometry is shown in

Table 3-10 and Figure 3.9 and the radial core geometry is shown in **Error! Reference source not found.**Figure 3.10. Since the main characteristics is boron-free, the more and mixed burnable absorbers, the solid Pyrex and Gadolinia rods, and control rods are used to control excess reactivity during the operation. And also, the axially different enrichments of burnable absorbers are used to control the axial power shape during a cycle as shown in Figure 3.11. Comparing to standard fuel assemblies, the heterogeneity along the axial direction is strongly high so that the axial power shapes are top-skewed to control reactivity and axial power shape easily with top-mounted control rods. The fuel loading pattern is also shown in Figure 3.11.

Table 3-10 Core information of BanDi-50

Assembly Type	17×17
Fuel Length	2.0 m
Fuel Material	4.95 w/o UO_2

Fuel Density	10.3404 g/cm^3
Burnable Absorber	Solid Pyrex (7~48 w/o B_2O_3) Gadolinia (4 w/o Gd_2O_3)
Pellet Radius	0.40958 cm
Cladding Thickness	0.06642 cm
Pin Pitch	1.2623 cm
Spacer Material	Zircaloy-2
Spacer Density	6.550 g/cm^3
Spacer Linear Density	21.505 g/cm

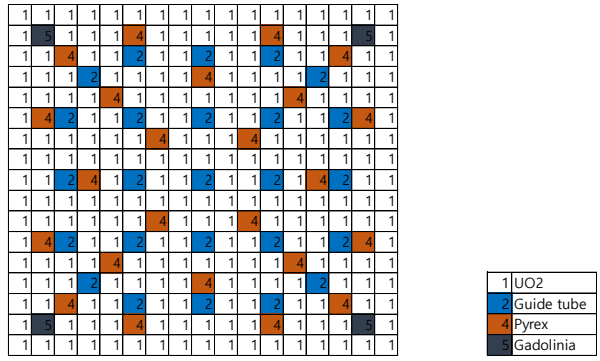

Figure 3.9 Fuel Assembly Configuration for BanDi-50

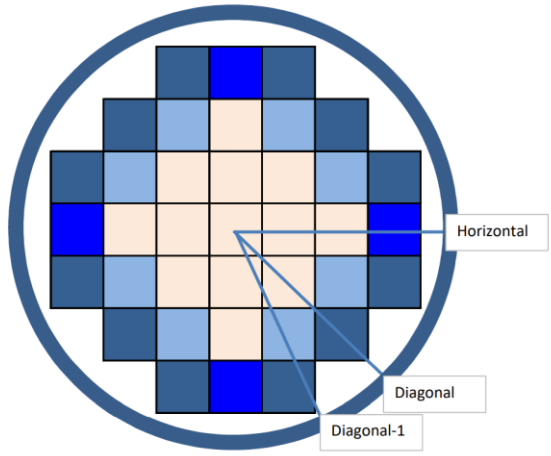

Figure 3.10 Core geometry of BanDi-50

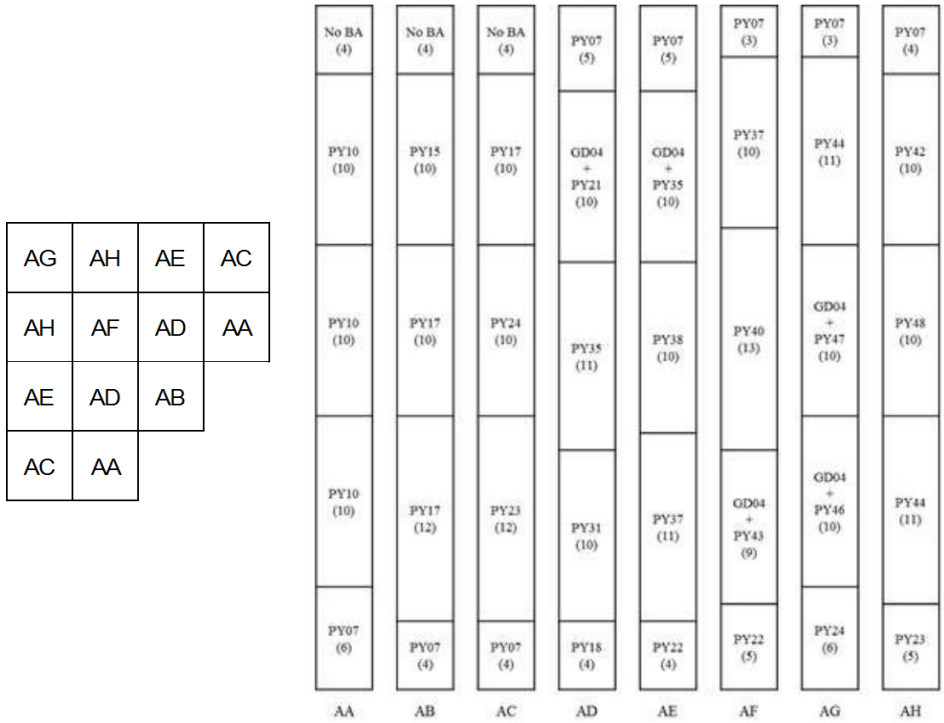

Figure 3.11 Loading Pattern and axial optimization in BanDi-50

Even though the assembly geometries of BanDi-50 are quite different from the commercial fuel assemblies, the proposed pin-wise two-step calculation process is followed in the calculation. The 25 radial configurations of fuel assemblies are independently modelled and calculated with the nTRACER code to generate four-group pin-wise cross-sections. After that, the final homogeneous cross-sections are generated as performing SPH iterations to incorporate SPH factors into the cross-sections. the reflector

cross-sections are also generated as following the conventional process which is introduced in L336C5 problem.

First of all, in order to investigate the basic performance to solve the strongly and axially heterogeneous fuel assembly problems having the high enriched burnable absorbers, the three-dimensional fuel assembly problems are established and calculated with reflective boundary conditions for each of 8 assembly types. As considering the different sizes of axial compositions of fuel assemblies, the mesh size of 5 cm is used in the calculations. the reference results are provided by nTRACER 3D calculations.

Table 3-11 shows the multiplication factors and maximum and RMS errors of axial power distributions of pin-wise solutions (nTRACER/PIN). nTRACER/PIN shows good agreement on the k-eff comparison with the maximum error of 90 pcm. Even though extremely top-skewed and severe gradient axial power shapes are observed as shown in Figure 3.12, the RMS errors of axial power distributions are only around 0.1 ~ 0.2 %. The maximum errors are around 2.0 ~ 3.0 % and they are shown at the uppermost mesh. Since the power value is around 6.0 at the uppermost mesh, the relative maximum errors are only 0.4 ~ 0.5 % as shown in Figure 3.12.

Table 3-11 3D Assembly Calculations in Bandi-50

	K-Eff			Axial Power Error	
	nTRACER	nTRACER/PIN	Error (pcm)	MAX. (%)	RMS., (%)
AA	1.30977	1.30951	-26	2.35	0.11
AB	1.29775	1.29745	-30	2.59	0.13
AC	1.29408	1.29408	0	2.69	0.14
AD	1.16192	1.16102	-90	2.68	0.15
AE	1.14982	1.14987	5	1.58	0.12
AF	1.11705	1.11675	-30	3.30	0.13
AG	1.10899	1.10948	49	2.28	0.11
AH	1.13473	1.13433	-40	2.81	0.13

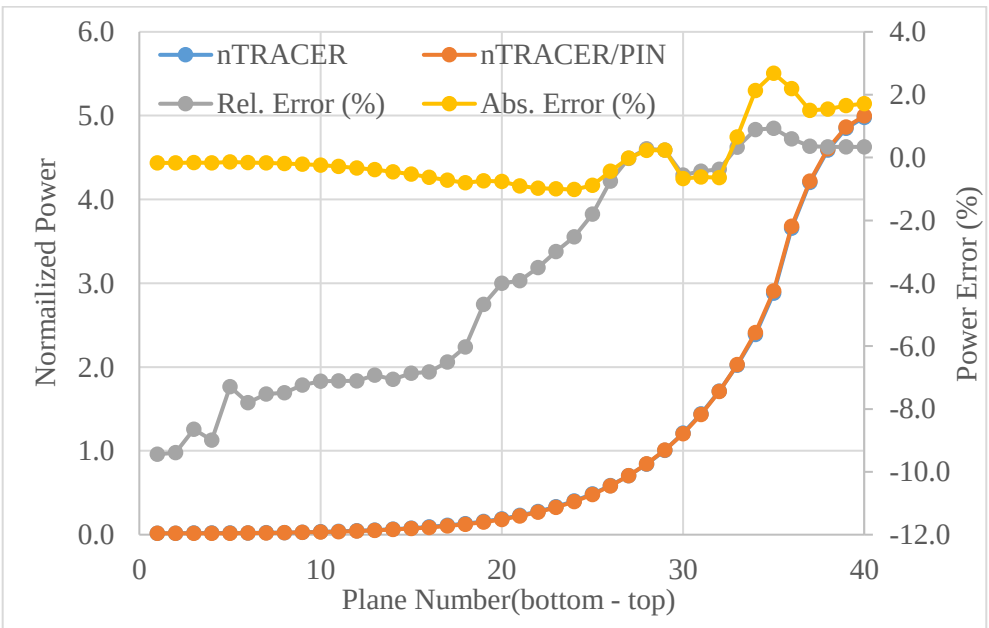

Figure 3.12 Axial power dist. of the fuel assembly AD in Bandi-50

The two-dimensional core calculations are also done with nTRACER, PIN and RENUS to verify pin-wise calculation performance for SMR reactors comparing to the conventional nodal calculations. From the core loading pattern of Figure 3.11, the axially middle configurations are selected to establish a two-dimensional problem as shown in Figure 3.13. Table 3-12 shows calculation results. With the reference value, the k-eff error of pin-wise calculation is only 33 pcm and the error of peaking factor is negligible even though the radial peaking factor of 1.562 is relatively higher than general values around 1.35 shown in the large commercial reactors and the power gradient from center to periphery is also higher. And the maximum error of the pin power distribution is 2.89 % which is shown at the outermost fuel rods but it is decreased to 1.19 % except the peripheral fuel rods in which pin powers are so low as shown in Figure 3.14 and Figure 3.15. The noticeable thing is that errors of the fuel rods near the burnable absorbers are not distinguishably higher than other fuel rods. Especially, the fuel rods near the Gadolinia rod located at (8,8) have similar errors comparing to errors of other fuel rods. This means the pin-wise calculation shows sufficiently good solutions where the lots of burnable absorbers are used and radial heterogeneity is very high.

With the results of RENUS, solutions of using the two-group structure

shows relatively higher pin power errors whereas the error of multiplication factor is only 74 pcm. RMS and maximum pin power errors are 1.44% and 6.55%. These errors are reduced to 0.86% and 5.76% with four-group structure. Comparing to these four-group results of the nodal calculation, pin-wise calculation improves about 2% of maximum pin power.

Table 3-12 Calculation results of the BanDi-50 2D problem

Code	K-Eff		Peaking Factor		Pin Power Dist. Error[1)]	
	Value	Error (pcm)	Value	Error (%)	RMS (%)	Max. (%)
nTRACER	1.01100	-	1.562	-	-	-
nTRACER/PIN	1.01133	33	1.568	0.35	0.01	2.89
RENUS (2G)	1.01174	74	1.553	-0.89	1.44	6.55
RENUS (4G)	1.01138	38	1.561	-0.08	0.86	5.76

• Pin Power Dist. Error[1)] : the absolute error with the normalized power distribution

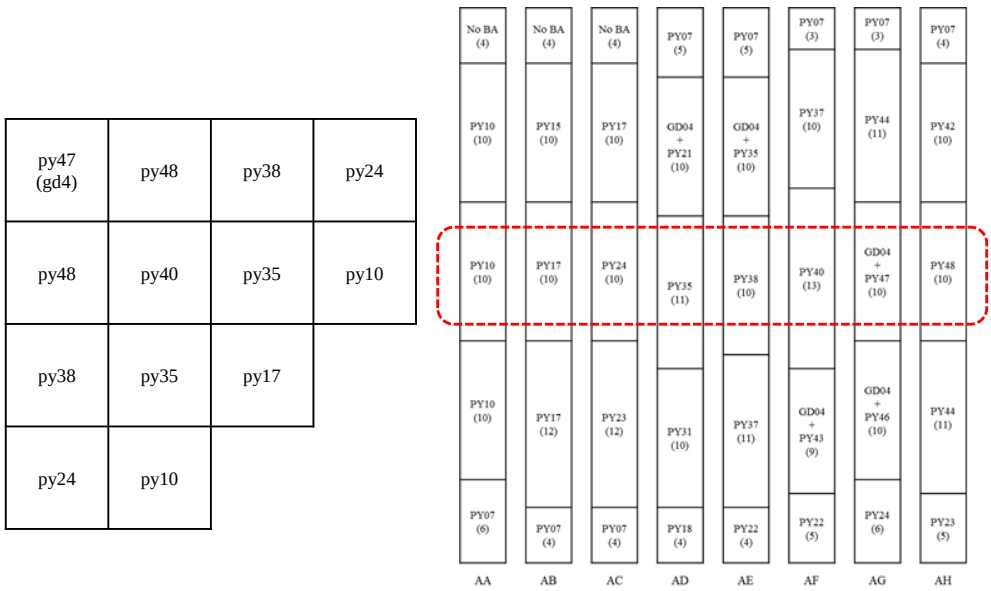

Figure 3.13 2D Core configuration of BanDi-50

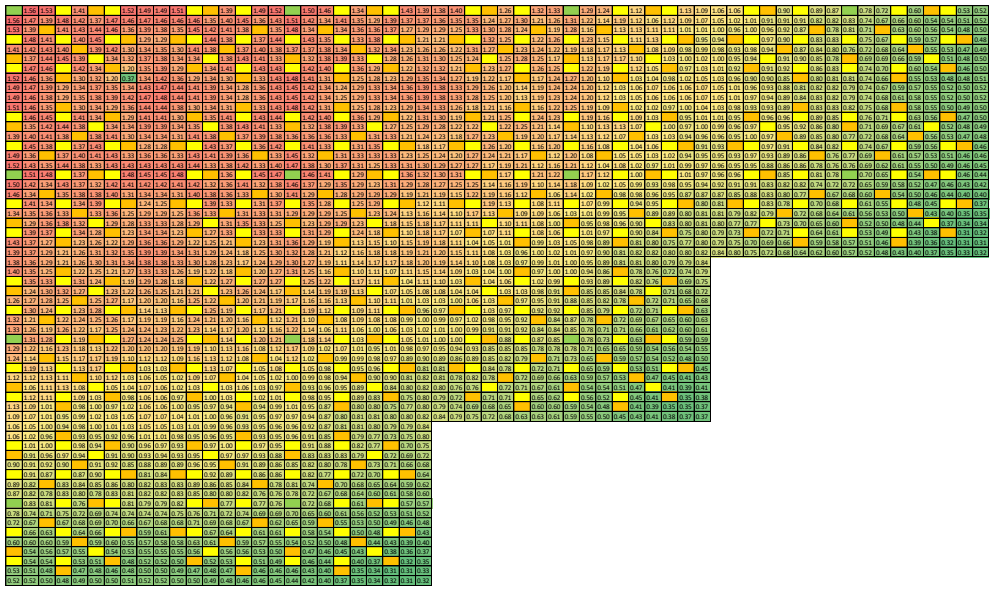

Figure 3.14 Pin power distribution(nTRACER) of 2D Core in Bandi-50

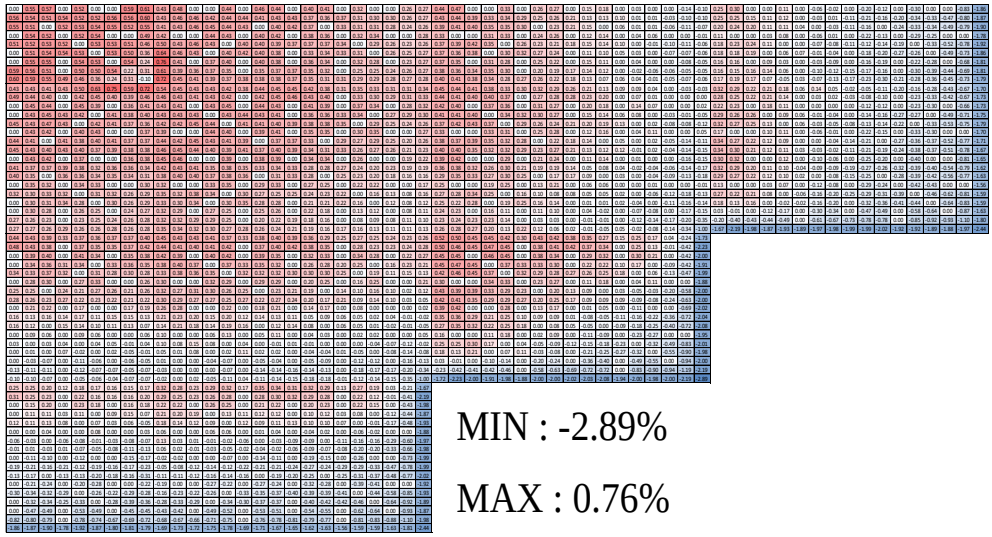

Figure 3.15 Pin power error distribution of 2D Core in Bandi-50

Finally, the 3D problem using the core geometry of Figure 3.9 and Figure 3.10 are established and solved with nTRACER and nTRACER/PIN codes to investigate performance of pin-wise calculations for SMR reactors. the bottom and top reflectors are neglected and the reflective boundary conditions are used for removing errors coming from the reflector modelling. Table 3-13 shows the calculation results of two codes. Like 2D calculations, solutions of the pin-wise calculation are almost close to the reference solutions calculated by whole core transport calculation of nTRACER with the k-eff error of 26 pcm and the RMS and maximum errors of pin power distribution of 0.01 % and 2.79 %. The maximum error is shown at the outermost fuel rod in which the pin power is so low as 0.39. Except the outermost fuel rods, the meaningful maximum error is decreased to 1.13 %. Despite of axially and radially high heterogeneity with axial zoning and lots of mixed burnable absorbers, the multiplication factor and pin power distribution of pin-wise calculations show very good accuracy comparing to the whole core transport calculation.

Table 3-13 Calculation results of the BanDi-50 3D problem

Code	K-Eff		2D Peaking Factor		Pin Power Dist. Error[1)]	
	Value	Error (pcm)	Value	Error (%)	RMS (%)	Max. (%)
nTRACER	1.10883	-	1.436	-	-	-

nTRACER/PIN	1.10909	26	1.440	0.24	0.01	2.79

• Pin Power Dist. Error[1] : the absolute error with the normalized power distribution

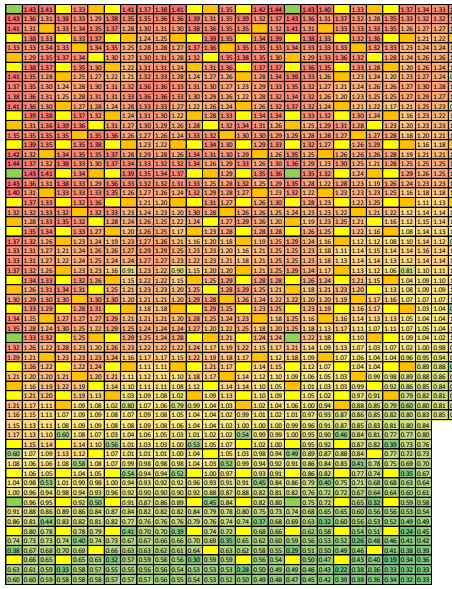

Figure 3.16 Pin power distribution(nTRACER) of 3D Core in Bandi-50

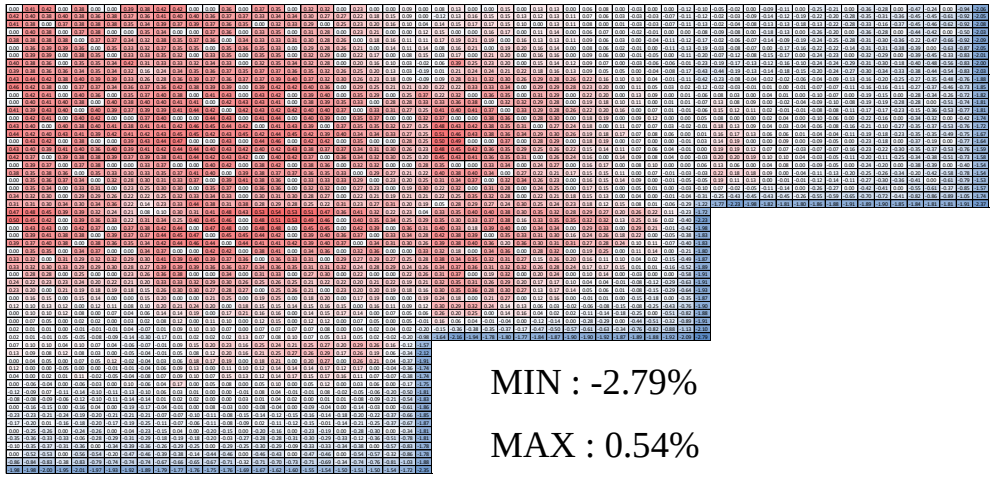

Figure 3.17 Pin power error distribution of 3D Core in Bandi-50

3.5. APR1400 Benchmark Problem

To evaluate efficiency and solution accuracy of the pin-wise 2D/1D decoupling method, numerical test calculations were carried out for the APR1400 PWR initial core. Hence the detailed core specifications are intellectual property of Korea Electric Power Corporation (KEPCO) and Korea Hydro and Nuclear Power (KHNP), a previous study targeting the core [18] employs published documents and a design control document which is provided by the United States Nuclear Regulatory Commission (U. S. NRC) via online [19]. Recently, however, Korea Atomic Energy Research Institute (KEARI) established a realistic core benchmark problem [20] which includes the neutronics modeling specifications and Monte-Carlo reference solutions generated by the McCARD code [21], so it became possible to consistently compare the Monte-Carlo reference, the deterministic transport to carry out both the lattice and the whole core transport calculations, and the pin-by-pin two-step which would be mainly used for the core design and analyses.

The APR1400 benchmark includes the following six problem sets.

1) Single fuel pin problems
2) 2D assembly problems
3) 2D core problems
4) 3D core problems

5) Control rod worth

6) 3D Core Depletion with Hot Full Power Condition

The problem 1 to 5 do not incorporate the thermos-hydraulic (T/H) effect. The fixed core conditions including the fuel and moderator temperatures (K) and the soluble boron concentrations (ppm) are provided in the benchmark with the Monte-Carlo reference solutions. Table 3-14 shows the three temperature conditions correspond to the cold-zero-power (CZP), hot-zero-power (HZP) and hot-full-power (HFP) nominal temperatures and boron concentrations. The cases would be referred as *CZ, HZ* and *HF* by the temperature with an attached digit indicating the boron concentrations.

Table 3-14. Conditions of APR1400 benchmark problem 1~5

Soluble boron concentration (ppm)	CZP Fuel: 300 K Moderator: 300 K	HZP Fuel: 600 K Moderator: 600 K	HFP Fuel: 900 K Moderator: 600 K
0	CZ0	HZ0	HF0
1000	CZ1	HZ1	HF1
2000	CZ2	HZ2	HF2

The problem 6 incorporates the T/H effect so the references are not provided. Only the core T/H conditions in Table 3-15 are designated.

Table 3-15. Core thermal conditions for APR1400 Problem 6

Parameter	Value
Pressure	15.51 MPa
Core thermal power	3983 MWth
Coolant inlet temperature	563.75 K
Coolant outlet temperature	597.05 K
Coolant mass flow rate	75.6×10^6 kg/hr

For the pin-wise calculations, the problem 1 and 2 have no meaning because the pin-wise homogenized group constants and corresponding SPH factors are commonly generated by single lattice calculations. The procedure inherently guarantees equivalence between the lower order solutions, the diffusion or SP3, and the transport solutions up to the 2D assembly level. Therefore, the problem 1 and 2 were replaced with the 2x2 checkerboard (CB) to observe the spectral interference effect by neighboring assemblies.

3.5.1 Overview of the APR1400 PWR initial core

To yield about 1,400 MW of electric power, the rated power of the initial core is nearly 4,000 MWth. The total number of fuel assemblies is 241 and the number of assemblies loaded along the core centerline is 17. Figure 3.18 shows a quadrant of the core with vertical and horizontal solid lines indicating the core centerline. Note that the stainless-steel shroud with about 2.2 cm

thickness radially surrounds the active core although it is not explicitly shown in the figure.

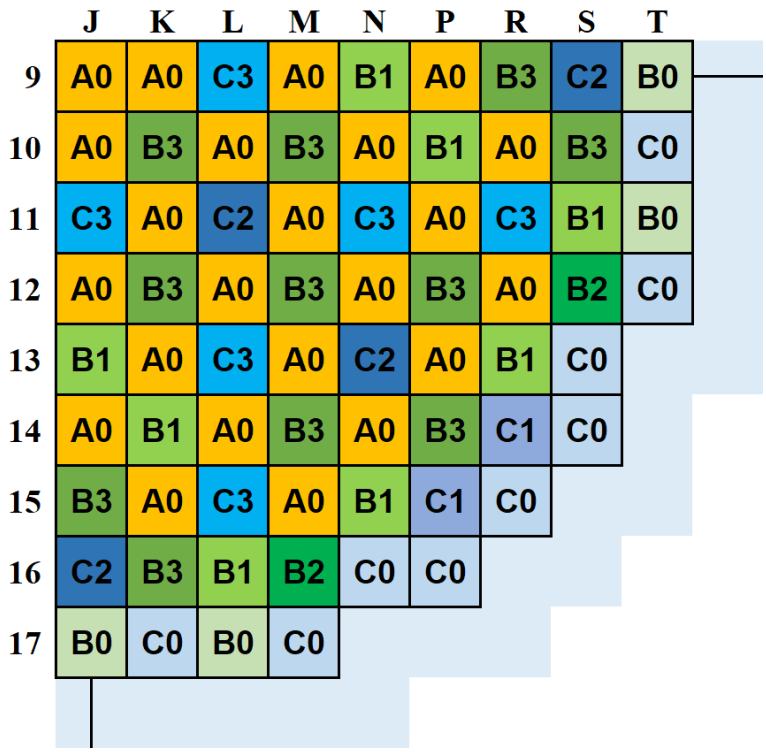

Figure 3.18. Radial assembly loading pattern of the APR1400 initial core

The CE-type fuel assembly has 16x16 lattice feature composed of 236 fuel pins, 4 guide tubes (GT) and 1 instrument tube (CT). According to the UO_2 fuel enrichment, the assemblies are categorized into A, B and C types, and the B and C types are split into 0 to 3 types by the radial enrichment zoning patterns and the number of Gadolinia burnable poison (BP) pins. The

Gadolinia pins are made of Gd_2O_3-UO_2 mixture and used to control the excessive reactivity of the core. The fuel enrichment and the number of Gadolinia pins by the assembly ID are listed in Table 3-16. Radial configurations for a lower-right quadrant of the B and C type assemblies are in Figure 3.19 and Figure 3.20. It should be noted that the numbers in each square-cell indicate the fuel enrichment and CT, GT and Gd denotes the center tube, guide tube and Gadolinia pins. The A0 assembly is the same as the B0 assembly except for the enrichment.

Table 3-16. Specifications of the APR1400 fuel assemblies

Assembly ID	Enrichment (%)	Number of BPs
A0	1.71	0
B0	3.14	0
B1	3.14 / 2.64	12
B2	3.14 / 2.64	12
B3	3.14 / 2.64	16
C0	3.64	0
C1	3.64 / 3.14	12
C2	3.64 / 3.14	16
C3	3.64 / 3.14	16

Axial configuration of the core is less heterogeneous than the radial configuration. The fuel pins except for the 1.72 % have lower-enriched

regions called as the axial blanket at the top and bottom ends to reduce the neutron leakage. Total height of the active fuel region including the blankets and normal fuel is 381 cm and length of each blanket is 15.24 cm.

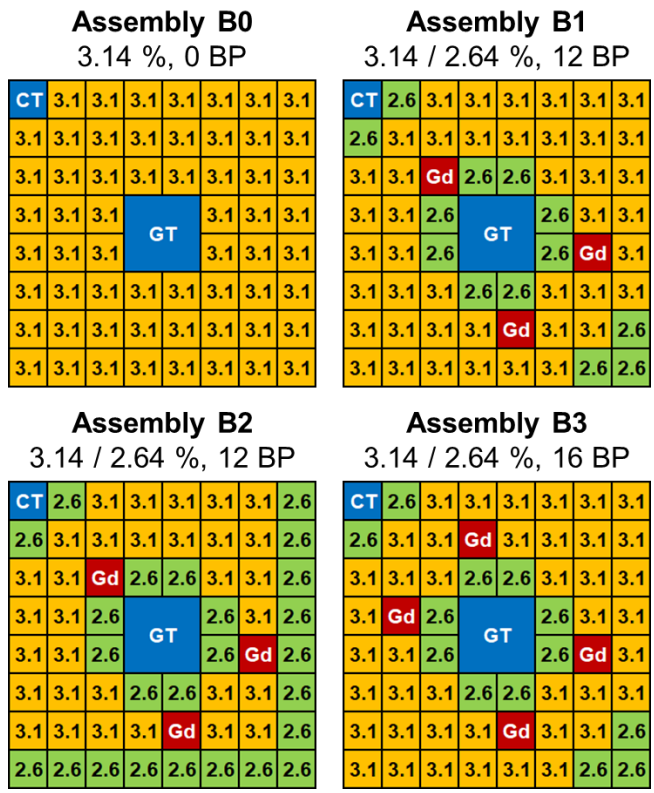

Figure 3.19. Radial configurations of the B type assemblies

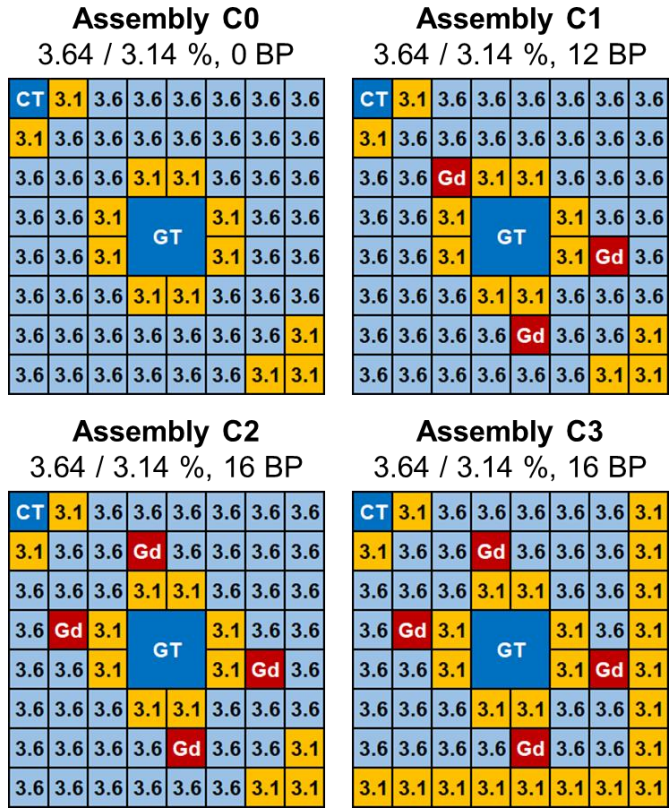

Figure 3.20. Radial configurations of the C type assemblies

The Gadolinia pins also have the axial heterogeneity at the top and bottom ends. The un-poisoned regions attached at the both ends are called a cutback. Length of the cutbacks are the same with the axial blankets.

Each assembly has 9 ZIRLO grids in the active fuel region. It would be worthwhile to note that 2 Inconel grids are in the bottom and top structure region including the plenum, standoff tube and nozzles, but the benchmark does not provide a detail of the structures and Inconel grids. Only the

moderator-filled planes with 50 cm thickness cover the both ends of the active fuel region as the axial reflectors. Figure 3.21 shows axial configuration of the C3 fuel assembly along a pin array indicated by the dotted red line.

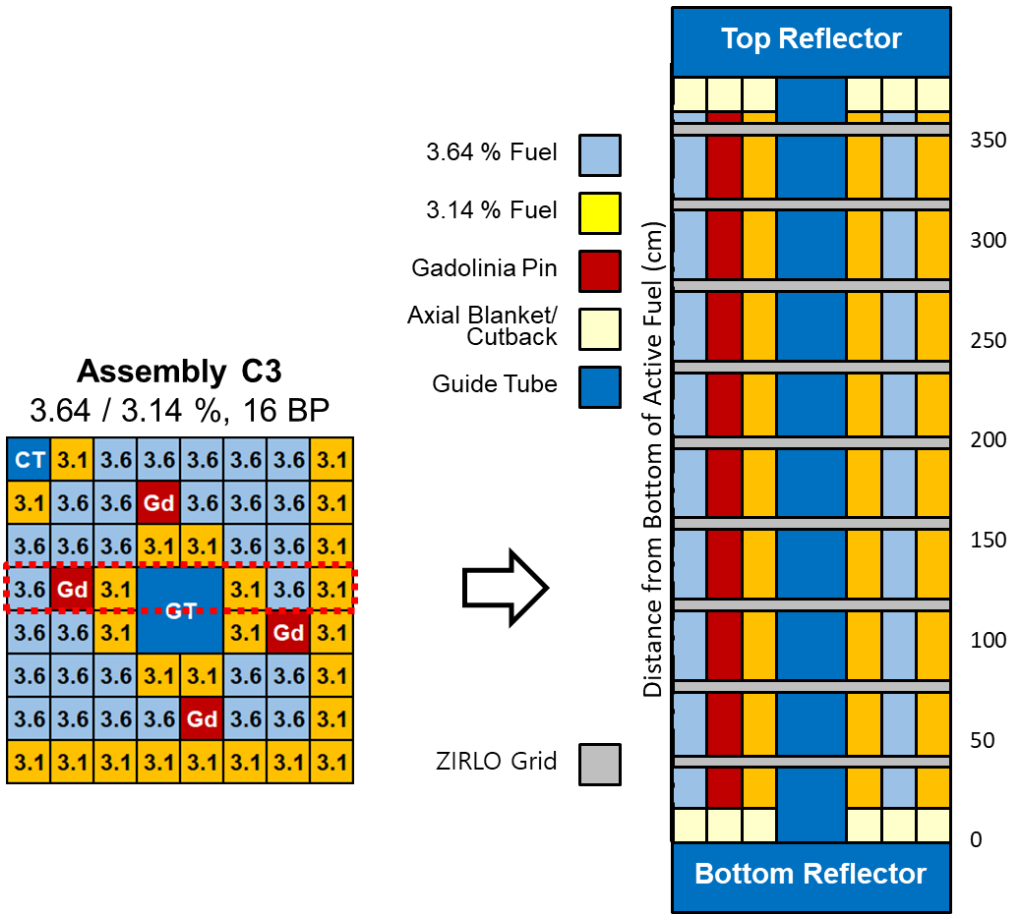

Figure 3.21. Active configurations of the C3 assembly

For purpose of controlling the core state, two types of the control element assemblies (CEAs) are employed. One is the full-strength CEA equipped with

the boron carbide (B_4C) neutron absorber covered by Inconel 625 cladding, and the other is the part-strength CEA equipped with the Inconel absorber covered by the Inconel cladding. The number of control rods per a CEA is 4 or 12 for the full-strength and 4 for the part-strength. By the number of control rods, the CEAs are denoted as 4-and 12-fingers. The benchmark provides specifications of the five (1 – 5) regulating group and the two (A, B) shutdown group control rod banks which consist of only the full-strength CEAs. Table 3-17 shows the number of CEAs included in each bank. *RG* and *SG* in the group column indicates the regulating group and the shutdown group. Hence, the control rod banks are inserted with a sequence of 5-4-3-2-1-B-A in the benchmark problem 5, the table follows the same order. Figure 3.22 and Figure 3.23 show locations of the CEAs in a core quadrant. The red-colored boxes with one-assembly size denotes the 4-finger CEAs while the cross-shaped rod boxes covering one assembly and its neighbors denotes the 12-finger CEAs.

Table 3-17. Specifications of the control rod banks

Bank ID	Group	4-finger CEAs	12-finger CEAs
5	RG	5	-
4	RG	8	-
3	RG	12	-
2	RG	8	4
1	RG	-	8
B	SG	-	20
A	SG	-	16

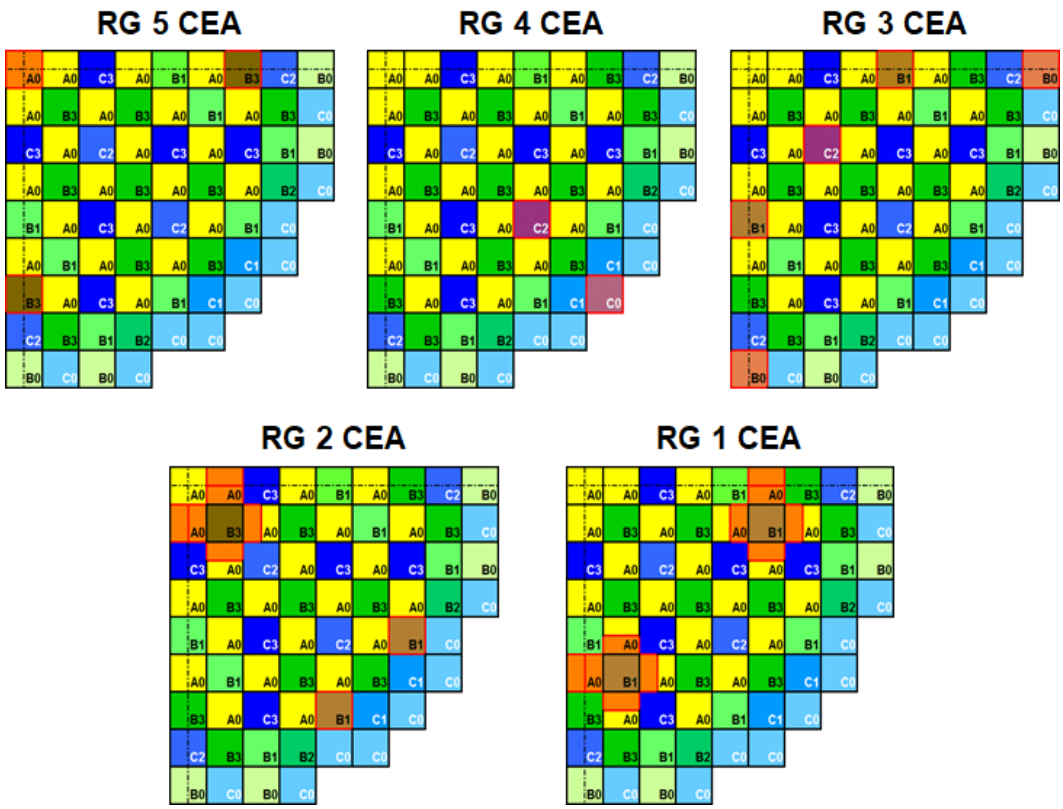

Figure 3.22. Radial configurations of the regulating group control banks

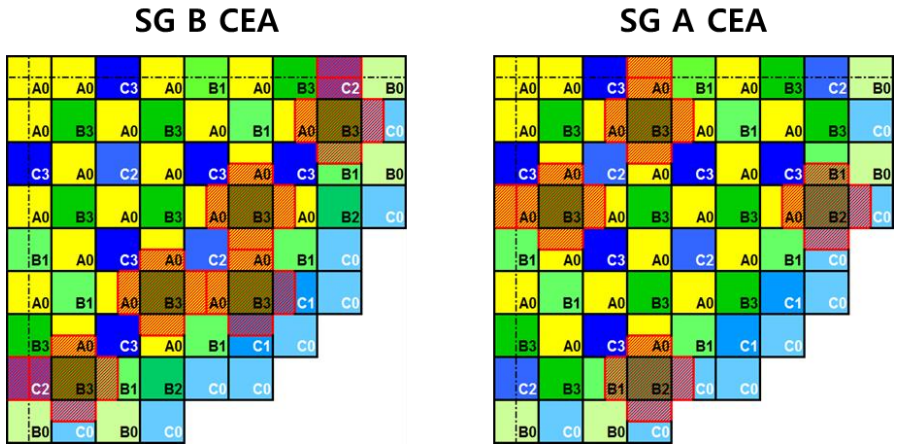

Figure 3.23. Radial configurations of the shutdown group control banks

3.5.2 Generation of the Pin-wise Homogeneous Cross-sections

The pin-wise homogeneous cross-sections are generated by the MOC calculations for lattices employing the nTRACER code and the corresponding SPH factors are generated by the pin-by-pin diffusion FDM calculations based on the transport solutions. The pin-wise cross-section generations and the SPH iterations to obtain the pin-wise equivalence factors are detailed in the follows.

(1) Specifications of the nTRACER calculations

As the conventional two-step core analysis, single lattice models are employed for the fuel assembly pin-wise cross-sections and the fuel-reflector

models are employed for the reflector pin-wise cross-sections. Hence the fuel assembly type used for the fuel-reflector model does not notably affects the reflector pin-wise cross-sections, the C0 assembly which is mainly loaded at the core periphery was used to generate the reflector pin-wise cross-sections.

All core components included in the models, such as fuel and Gadolinia pins, guide tubes with and without the control rods, center tube and the stainless-steel shroud, are explicitly modeled. The assembly water gaps are also explicitly modeled but the water gap pins are included in the fuel pins loaded along the assembly periphery by the pin-wise homogenization. Figure 3.24 shows modeling of a fuel pin-cell and sub-pin level discretization as an example. The fuel pellet, air gap, ZIRLO cladding and moderator region are modeled as the left figure without an assumption, and those were discretized into several flat-source-regions (FSRs) as the right figure to yield accurate transport solutions. On the other hand, the nine ZIRLO grids in the active fuel region are smeared into the moderator by preserving the total mass.

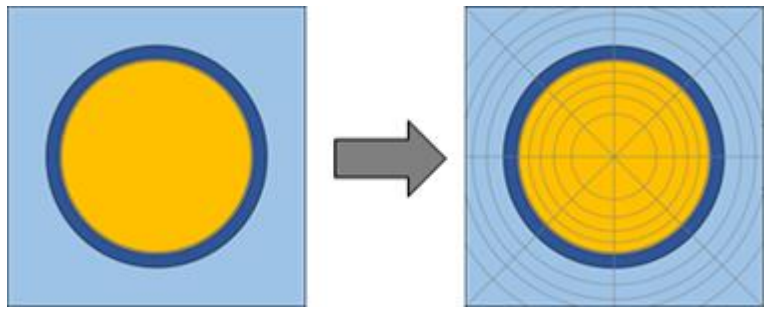

Figure 3.24. Modeling of a fuel pin-cell for the nTRACER calculations

The nTRACER calculations for the models are carried out by the transport corrected P0 MOC solver. The MOC ray spacing is 0.05 cm and the number of azimuthal and polar angles is 16 per a quadrant of azimuthal plane and 4 per a hemisphere. The transport solutions are based on the in-scatter corrected 47-group RPL library. To obtain fully converged pin-wise solutions, the MOC sweeps are repeated until the source-normalized residual became less than 10^{-8}.

(2) Generation of the SPH factors

The SPH generations are performed by the pin-by-pin diffusion FDM calculations for the fuel lattices and the fuel-reflector models. In case of the fuel assemblies, the assembly averaged SPH factor in each group is normalized to a unity by the standard SPH iteration scheme. Moreover, the volume adjustment to treat each pin-cell as the same-sized finite difference

mesh was performed while in the SPH factor generation, therefore, the SPH factors guarantee the equivalence between the diffusion FDM employing the volume-adjusted cross-sections and the reference transport solutions. The iteration scheme is shown in Figure 2.3.

(3) Generation of the reflector cross-sections

For the core calculation, cross-section sets are needed to be produced for fuel assembly and radial/axial reflectors. The cross-section set of fuel assembly is simply generated by a single assembly problem with the reflective boundary condition. To generate the reflector cross-section, five sets of the fuel assembly-reflector problems are constructed for the radial and axial reflectors as shown in the Figure 3.25.

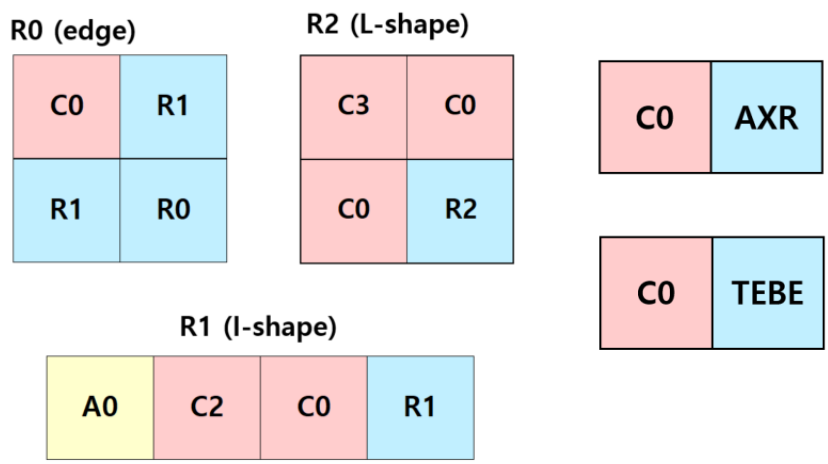

Figure 3.25 fuel-reflector configurations for reflector XS generation

For the case of R0 and R2 reflectors, the 2x2 problems of the conventional method are constructed to produce the reflector cross-sections. The cross-sections of axial reflector (AXR) and top/bottom end (TEBE) are produced through the fuel assembly-reflector problem where only one fuel assembly is placed as shown in the Figure 3.25. For generating R1-type reflector cross-sections, the two-assembly problem which is composed of one fuel and one reflector assemblies are simply used in the conventional calculation. In this work, the effect of the number of fuel assemblies is tested to figure out the optimum number of fuel assemblies for minimizing errors of radial power distributions. 6 sets of reflector cross-sections are generated as placing 1 ~ 6 fuel assemblies next to the reflector assembly. Additionally, a set of cross-sections for all reflector assembly is generated from the nTRACER 2D core problem. Table 3-18 shows the reactivity and power distribution errors of 2D core calculation with the 7 different reflector cross-section sets as comparing with the nTRACER solution.

A case using the reflector cross-sections generated from the 2D core calculation shows about -38 pcm of reactivity and 0.48%/1.06% of RMS/MAX pin power errors which is the best solution of pin-wise calculation. As comparing this solution, the number of fuel assemblies does not make a major effect on the reactivity since the error is under 10 pcm even though one fuel assembly is just considered. But the maximum and RMS

assembly power errors are meaningfully decreased with the reasonable number of fuel assemblies. From the results, the R1-type reflector cross-sections are generated as considering 3 fuel assemblies as shown in Figure 3.25 and they are used in the following 2D and 3D calculations.

Table 3-18 2D core errors with # of FAs used for generating reflector XS

No. of FAs	Reactivity Diff. [pcm]	RMS Power Diff [%]	MAX Power Diff [%]
1	-27.9	1.03	2.35
2	-28.9	0.93	2.13
3	-30.9	0.85	1.95
4	-31.5	0.82	1.87
5	-33.9	0.68	1.54
6	-33.2	0.72	1.63
Core	-37.7	0.48	1.06

3.5.3 Numerical Results

The pin-wise 3D calculations are performed for the benchmark problems. As noted earlier, the fuel assembly pin-wise cross-sections and the corresponding SPH factors are generated by the heterogeneous transport and

lower-order (diffusion) homogeneous calculations for single assemblies. Therefore, the diffusion calculation doesn't show any numerical error as comparing to the transport calculation. For this reason, the single fuel pin problems and 2D assembly problems are replaced by the 2x2 checkerboard problems to observe the spectral interference effect by the neighboring assemblies.

The accuracy of the pin-wise calculation is assessed by comparison with reference solutions generated by the direct whole core calculations employing the nTRACER code. To maintain consistency between the pin-wise and the transport calculations, the modeling specifications and the calculation options including the ray parameters and the 47-group XS library are kept unchanged.

(1) 2x2 checkerboard problems

The 36 checkerboard configurations with the 9 fuel assembly types are introduced for the numerical tests. Each of the checkerboard problems is named with the loaded assembly types and corresponding core condition. For example, the A0C2-HF1 case denotes a checkerboard problem consisting of the A0 and C2 type assemblies with the hot-full-power temperature condition and 1000 ppm soluble boron concentration. The pin-wise eight-group cross-sections are used to properly take account the spectral condensation error and the SPH factors for the diffusion FDM with 1 mesh per pin are generated by

following the SPH method.

The reactivity differences obtained by total 324 (36x9) cases of the checkerboard calculations are shown in Table 3-19. Considering various core thermal conditions from the cold-zero-power (CZ) to the hot-full-power (HF) and soluble boron concentration from 0 to 2,000 ppm, the accuracy is fairly observed except for B3C0-CZ1, B3C0-CZ2 and A0C0-CZ2 having -51.3 pcm, -56.9 pcm and -56.6 pcm errors of the reactivity, the other 321 cases show good agreement of the reference solutions with less than 50 pcm of the reactivity errors.

Table 3-19 Reactivity differences in checkerboard problems

Case ID	Reactivity difference (pcm)				
	Average	RMS	Max.	Min.	Stdev.
CZ0	-13.9	21.6	9.5	-45.4	16.8
CZ1	-15.4	23.6	12.0	-51.3	18.1
CZ2	-19.2	28.9	13.8	-56.9	21.9
HZ0	-11.3	20.8	13.9	-40.6	17.7
HZ1	-10.9	20.9	15.5	-42.6	18.0
HZ2	-11.5	21.5	16.7	-44.9	18.4
HF0	-11.5	21.1	14.4	-41.0	17.9
HF1	-11.1	21.2	16.0	-43.0	18.3
HF2	-11.7	21.8	17.2	-45.3	18.6

For all the temperature and soluble boron conditions, the root-mean-square (RMS) and maximum pin power errors are less than 0.8 % and 1.5 %, as shown in Figure 3.26, Figure 3.27 and Figure 3.28. However, the pin-power error is more sensitive to the thermal condition while the reactivity difference was not significantly affected. In case of the A0C0 checkerboard, for example, the RMS and maximum of the pin-power errors were 0.78 % and 1.38 % for CZ2, 0.41 % and 0.77 % for HZ2 and 0.41 % and 0.78 % for HF2 conditions. Hence the HZ and HF share the same moderator temperature (600 K) condition, it is considered as the main reason which contributes the notable difference in the pin power error of the CZ cases.

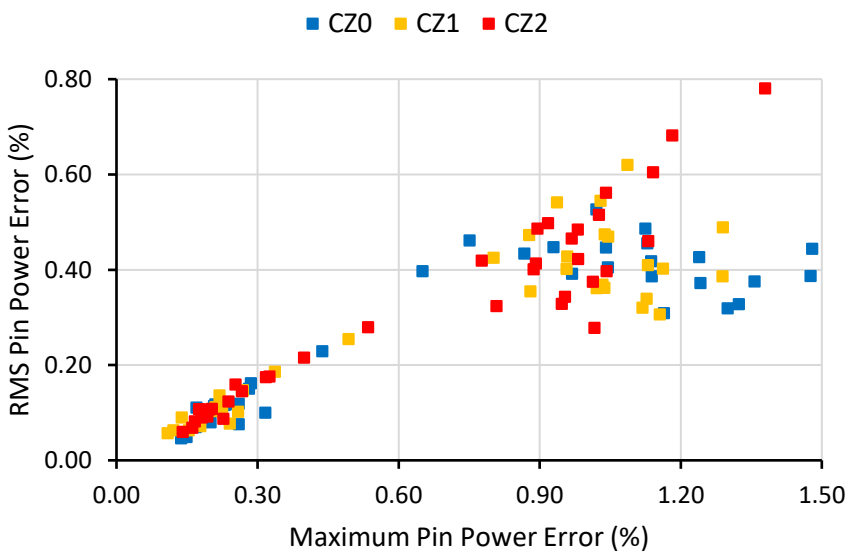

Figure 3.26. RMS and MAX pin power errors of CZP 2X2 problems

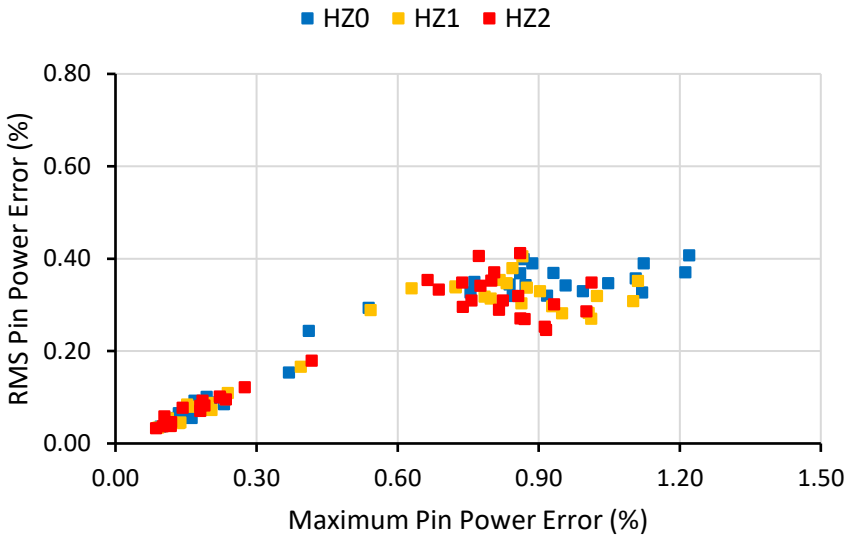

Figure 3.27. RMS and MAX pin power errors of HZP 2X2 problems

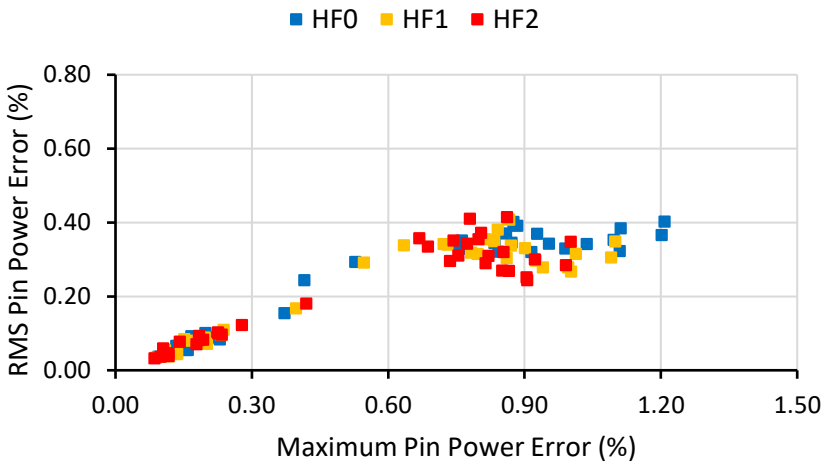

Figure 3.28. RMS and MAX pin power errors of HFP 2X2 problems

It is noted that the pin power error distribution shapes are affected by the Gadolinia burnable poison pins. The A0C0-HF2 checkerboard result shown in Figure 3.29 is an example without Gadolinia pins. Both the A0 assembly at the top-left and bottom-right and the C0 assembly at the top-right and bottom-left are loaded with the fuel pins only. In this case, the pin power error along the assembly boundaries was marginal while the significant error was observed at the center of each assembly. On the other hand, the A0C2-HF2 checkerboard in Figure 3.30 is an example with the Gadolinia pins. The C2 assembly at the top-right and bottom-left includes the 12 Gadolinia pins. In this case, the maximum pin power error was observed at the assembly boundaries and the error at the center region was relatively small.

	0.865	0.821	0.805	0.793	0.779	0.760	0.734	1.258	1.173	1.147	1.148	1.160	1.197	1.158	
0.865	0.836	0.821	0.817	0.808	0.789	0.765	0.737	1.264	1.185	1.171	1.184	1.192	1.197	1.236	1.158
0.821	0.821	0.834	0.859	0.853	0.811	0.775	0.743	1.276	1.209	1.230	1.151	1.151	1.231	1.197	1.197
0.805	0.817	0.859			0.844	0.786	0.749	1.287	1.236	1.164			1.152	1.192	1.160
0.793	0.808	0.853			0.842	0.786	0.751	1.293	1.243	1.171			1.151	1.184	1.148
0.779	0.789	0.811	0.844	0.842	0.806	0.775	0.749	1.300	1.236	1.256	1.171	1.164	1.230	1.171	1.147
0.760	0.765	0.775	0.786	0.786	0.775	0.763	0.749	1.167	1.252	1.236	1.243	1.236	1.209	1.185	1.173
0.734	0.737	0.743	0.749	0.751	0.749	0.749	0.750	1.210	1.167	1.300	1.293	1.287	1.276	1.264	1.258
1.258	1.264	1.276	1.287	1.293	1.300	1.167	1.210	0.750	0.749	0.749	0.751	0.749	0.743	0.738	0.734
1.173	1.185	1.209	1.236	1.243	1.236	1.252	1.167	0.749	0.763	0.775	0.786	0.786	0.775	0.765	0.760
1.147	1.171	1.230	1.164	1.171	1.256	1.236	1.300	0.749	0.775	0.806	0.842	0.844	0.811	0.789	0.779
1.148	1.184	1.151			1.171	1.243	1.293	0.751	0.786	0.842			0.853	0.808	0.793
1.160	1.192	1.152			1.164	1.236	1.287	0.749	0.786	0.844			0.859	0.817	0.805
1.197	1.197	1.231	1.151	1.151	1.230	1.209	1.276	0.743	0.775	0.811	0.853	0.859	0.834	0.821	0.821
1.158	1.236	1.197	1.192	1.184	1.171	1.185	1.264	0.737	0.765	0.789	0.808	0.817	0.821	0.836	0.865
	1.158	1.197	1.160	1.148	1.147	1.173	1.258	0.734	0.760	0.779	0.793	0.805	0.821	0.865	

	0.78	0.75	0.70	0.61	0.46	0.18	-0.22	0.24	-0.04	-0.33	-0.49	-0.59	-0.65	-0.69	
0.78	0.77	0.74	0.68	0.60	0.45	0.18	-0.20	0.22	-0.04	-0.32	-0.48	-0.57	-0.63	-0.67	-0.69
0.75	0.74	0.70	0.64	0.56	0.43	0.19	-0.17	0.18	-0.05	-0.30	-0.45	-0.54	-0.59	-0.63	-0.65
0.70	0.68	0.64			0.39	0.19	-0.12	0.13	-0.06	-0.28			-0.54	-0.58	-0.59
0.61	0.60	0.56			0.35	0.17	-0.11	0.12	-0.04	-0.24			-0.45	-0.48	-0.49
0.45	0.45	0.43	0.39	0.35	0.28	0.12	-0.13	0.16	0.02	-0.14	-0.24	-0.28	-0.30	-0.32	-0.33
0.18	0.18	0.19	0.19	0.17	0.12	0.02	-0.10	0.11	0.09	0.02	-0.04	-0.06	-0.05	-0.04	-0.04
-0.22	-0.20	-0.17	-0.12	-0.11	-0.13	-0.10	-0.11	0.05	0.11	0.16	0.12	0.13	0.18	0.22	0.24
0.24	0.22	0.18	0.13	0.12	0.16	0.11	0.05	-0.11	-0.10	-0.13	-0.11	-0.12	-0.17	-0.20	-0.22
-0.04	-0.04	-0.05	-0.06	-0.04	0.02	0.09	0.11	-0.10	0.02	0.11	0.17	0.19	0.19	0.18	0.18
-0.33	-0.32	-0.30	-0.28	-0.24	-0.14	0.02	0.16	-0.13	0.11	0.28	0.35	0.39	0.43	0.45	0.45
-0.50	-0.48	-0.46			-0.24	-0.04	0.12	-0.11	0.17	0.35			0.56	0.60	0.61
-0.59	-0.58	-0.54			-0.28	-0.06	0.13	-0.12	0.19	0.39			0.64	0.68	0.70
-0.65	-0.63	-0.59	-0.54	-0.46	-0.30	-0.05	0.18	-0.17	0.19	0.43	0.56	0.64	0.70	0.73	0.75
-0.69	-0.67	-0.63	-0.58	-0.48	-0.32	-0.04	0.22	-0.20	0.18	0.45	0.60	0.68	0.74	0.77	0.78
	-0.69	-0.65	-0.59	-0.50	-0.33	-0.04	0.24	-0.22	0.18	0.45	0.61	0.70	0.75	0.78	

Figure 3.29 Pin power and error (%) of the A0C0-HF2 2X2 problem

	0.976	0.925	0.903	0.887	0.865	0.838	0.803	1.353	1.236	1.169	1.105	1.043	1.130	1.138	
0.976	0.943	0.924	0.916	0.901	0.875	0.842	0.803	1.351	1.240	1.185	1.104	0.232	1.085	1.189	1.139
0.925	0.924	0.936	0.961	0.949	0.897	0.849	0.804	1.343	1.239	1.234	1.116	1.061	1.136	1.085	1.130
0.903	0.916	0.961			0.929	0.856	0.800	1.310	1.181	1.137			1.061	0.232	1.043
0.887	0.901	0.949			0.923	0.851	0.793	1.266	0.237	1.088			1.116	1.104	1.104
0.865	0.875	0.897	0.929	0.923	0.878	0.837	0.795	1.316	1.166	1.186	1.088	1.137	1.234	1.185	1.169
0.838	0.842	0.849	0.856	0.851	0.837	0.820	0.799	1.219	1.264	1.166	0.237	1.181	1.239	1.240	1.236
0.803	0.803	0.804	0.800	0.793	0.795	0.799	0.801	1.282	1.219	1.316	1.265	1.310	1.343	1.351	1.353
1.353	1.352	1.343	1.310	1.265	1.316	1.219	1.282	0.801	0.799	0.795	0.793	0.800	0.804	0.803	0.803
1.236	1.240	1.239	1.181	0.237	1.166	1.264	1.219	0.799	0.820	0.837	0.851	0.856	0.849	0.842	0.838
1.169	1.185	1.234	1.137	1.088	1.186	1.166	1.316	0.795	0.837	0.878	0.923	0.929	0.897	0.875	0.865
1.105	1.104	1.116			1.088	0.237	1.266	0.793	0.851	0.923			0.949	0.901	0.887
1.043	0.232	1.061			1.137	1.181	1.310	0.800	0.856	0.929			0.961	0.916	0.903
1.130	1.085	1.136	1.061	1.116	1.234	1.239	1.343	0.804	0.849	0.897	0.949	0.961	0.936	0.924	0.925
1.138	1.189	1.085	0.232	1.104	1.185	1.240	1.351	0.803	0.842	0.875	0.901	0.916	0.924	0.943	0.976
	1.139	1.130	1.043	1.105	1.169	1.236	1.353	0.803	0.838	0.865	0.887	0.903	0.925	0.976	

	0.40	0.37	0.34	0.27	0.16	-0.07	-0.37	0.19	0.07	-0.14	-0.27	-0.34	-0.36	-0.40	
0.40	0.40	0.36	0.32	0.26	0.14	-0.08	-0.36	0.18	0.09	-0.10	-0.21	-0.43	-0.36	-0.39	-0.40
0.37	0.36	0.34	0.30	0.24	0.12	-0.10	-0.35	0.16	0.09	-0.09	-0.21	-0.28	-0.31	-0.36	-0.36
0.34	0.33	0.30			0.05	-0.17	-0.46	0.24	0.12	0.01			-0.28	-0.43	-0.35
0.27	0.26	0.24			-0.02	-0.25	-0.75	0.92	-0.02	0.08			-0.21	-0.21	-0.27
0.16	0.14	0.12	0.05	-0.02	-0.09	-0.24	-0.50	0.28	0.21	0.19	0.08	0.01	-0.09	-0.11	-0.14
-0.07	-0.08	-0.10	-0.17	-0.25	-0.24	-0.27	-0.37	0.13	0.20	0.21	-0.02	0.12	0.09	0.09	0.07
-0.37	-0.36	-0.35	-0.46	-0.75	-0.50	-0.36	-0.31	0.00	0.13	0.28	0.92	0.24	0.16	0.18	0.19
0.19	0.18	0.16	0.24	0.92	0.28	0.13	0.00	-0.31	-0.37	-0.50	-0.75	-0.46	-0.35	-0.36	-0.37
0.07	0.09	0.09	0.12	-0.02	0.21	0.20	0.13	-0.37	-0.27	-0.24	-0.25	-0.17	-0.10	-0.08	-0.07
-0.14	-0.11	-0.09	0.01	0.08	0.19	0.21	0.28	-0.50	-0.24	-0.09	-0.02	0.05	0.12	0.14	0.16
-0.27	-0.21	-0.21			0.08	-0.02	0.92	-0.75	-0.25	-0.02			0.24	0.26	0.27
-0.34	-0.43	-0.28			0.01	0.12	0.24	-0.46	-0.17	0.05			0.30	0.32	0.34
-0.36	-0.36	-0.31	-0.28	-0.21	-0.09	0.09	0.16	-0.35	-0.10	0.12	0.24	0.30	0.34	0.36	0.37
-0.40	-0.39	-0.36	-0.43	-0.21	-0.10	0.09	0.18	-0.36	-0.08	0.14	0.26	0.32	0.36	0.40	0.40
	-0.40	-0.36	-0.34	-0.27	-0.14	0.07	0.19	-0.37	-0.07	0.16	0.27	0.34	0.37	0.40	

Figure 3.30 Pin power and error (%) of the A0C2-HF2 2X2 problem

(2) 2D Core Problems

The two-dimensional all-rods-out (ARO) core has radial vacuum and axial reflective boundary conditions. The core is surrounded by simplified reflector assemblies. The reflector assemblies include only the shroud and the empty space is filled with moderator. The 2D core problems are also named with the core conditions. As noted already, the CZ, HZ and HF indicate the cold-zero-power, hot-zero-power and hot-full-power temperature conditions and the digits from 0 to 2 indicate the boron concentrations.

The reactivity, RMS and maximum assembly power differences of the 2D core problems are shown in Figure 3.31 ~ Figure 3.34. The reference solutions of the result are produced by McCARD calculations. In the figures, 'nTRACER/PIN' represents the pin-wise calculation with homogeneous pin-wise cross-sections generated by single assembly calculations of nTRACER. As shown in the Figure 3.31, the reactivity errors of the pin-wise calculations are under ~50 pcm in hot-zero-power and hot-full-power cases as comparing the reference McCARD solutions. In cold-zero-power cases, the errors of the nTRACER solutions as well as nTRACER/PIN solutions seems to be higher about 170 pcm than the reference solution. Since the all of the pin-wise group constants used in the nTRACER/PIN calculations are generated by the nTRACER calculations, the numerical errors of nTRACER/PIN calculations can be clearly quantified by comparing the nTRACER solutions as shown in

the Figure 3.32. As shown in the figure, the errors are only under 40 pcm in all cases. It is noted that the pin-wise two-step calculation procedure provides very good solutions in terms of reactivity. The Figure 3.33 and Figure 3.34 show the RMS and maximum errors of assembly power distributions as comparing with the reference solutions. the nTRACER/PIN solutions show about 1% and 3% of RMS and maximum errors which are smaller than errors of the DeCART solutions. The detail assembly-wise error distributions of the HF1 case to the reference solution are shown in the Figure 3.35. The nTRACER solution shows about 1% in/out power tilt whereas the DeCART solution shows about 2% in/out tilt. the nTRACER/PIN solution also shows about 2.7% tilt which is approximately close to the DeCART. The reason is that nTRACER/PIN uses pin-wise homogenized group constants which are well generated with the better flux distribution of nTRACER and its pin-wise calculation is reasonable to estimate surface flux gradients.

The solutions are compared the nTRACER solutions to investigate the numerical errors of nTRACER/PIN solutions as shown in Figure 3.36 and Figure 3.37. The RMS and maximum errors are only about 1% and 2%. In terms of the assembly power distributions representing local solutions, the nTRACER/PIN calculation procedure shows accurate solutions.

The pin power distributions of nTRACER/PIN are also compared to the nTRACER solutions as shown in Figure 3.38. The axially integrated pin

power distribution is normalized to the core volume as the following equation. The maximum and RMS pin power errors are approximately 1% higher than the assembly power errors. In cold-zero-power cases, the maximum pin power errors are higher than other cases. The pin power errors are also high due to approximation of the reflector cross-section generation and the pin powers are high at the peripheral region in low temperature condition because the high enriched fuel assembly is located. Similarly, HF0, HF1 are HF2 show better solutions with lower error than 2% pin power since the temperature is high and the peripheral power is relatively low. In the nuclear design, the pin power distributions become concern when the meaningful power is generated and the power is much low in the peripheral region due to the leakage and negative feedbacks. In that cases, the pin power errors should be much lower.

To choose the efficient number of energy groups, the HZ0 problem are solved with the four- and eight-group cross-sections. As shown in the Figure 3.39, the eight-group solution is better than the four-group solution in terms of reactivity and assembly power distribution. However, the reactivity errors of both solutions are under 50 pcm and the RMS and maximum errors are under 1.0% and 2.0%. Therefore, it is noted that four-group calculations provide a reasonably accurate solution, yet fast computing time.

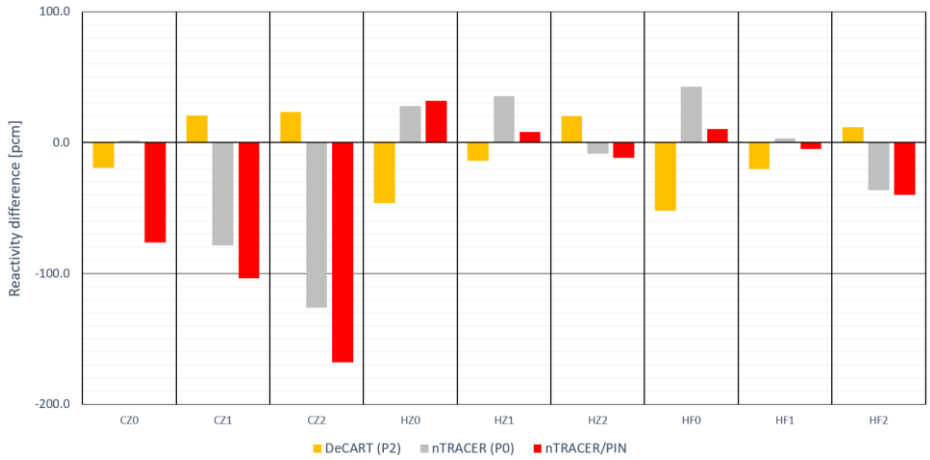

Figure 3.31 Reactivity diff. for 2D core problems (Ref: McCARD)

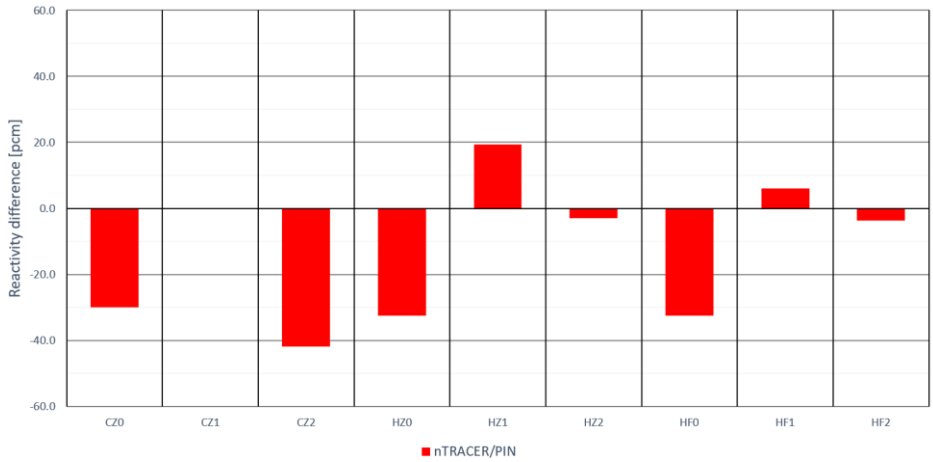

Figure 3.32 Reactivity diff. for 2D core problems (Ref: nTRACER)

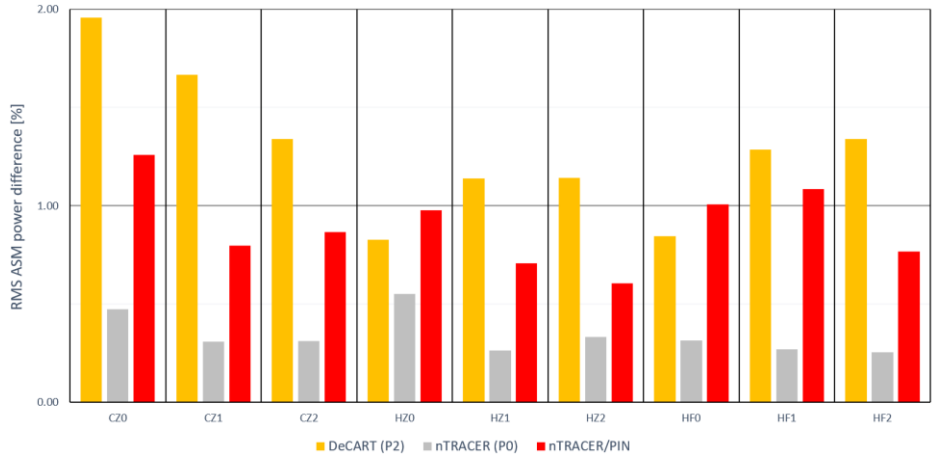

Figure 3.33 RMS assembly power differences of 2D core problems

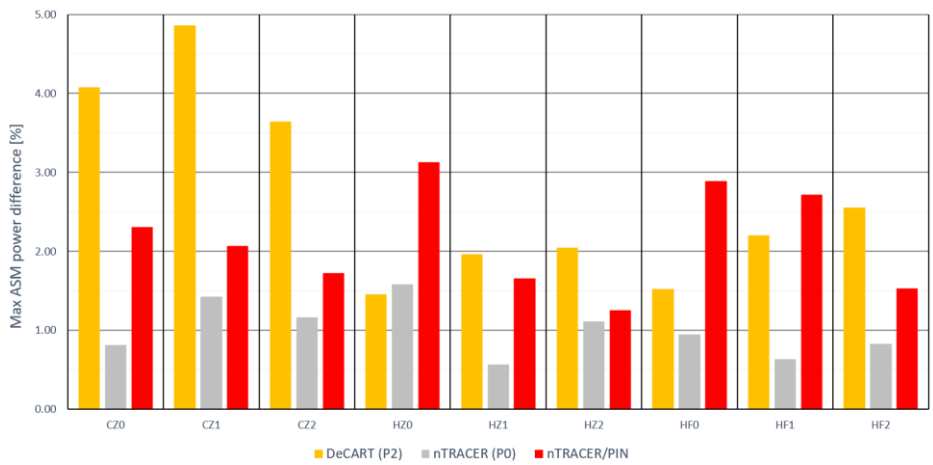

Figure 3.34 MAX assembly power differences of 2D core problems

< DeCART >

-2.11	-1.97	-1.88	-1.65	-1.19	-0.67	0.19	1.21	2.19
	-1.99	-1.91	-1.52	-1.23	-0.37	-0.01	1.06	2.22
		-1.89	-1.54	-0.91	-0.47	0.50	1.09	1.84
			-1.08	-0.80	-0.08	0.30	1.18	1.55
				-0.18	-0.03	0.93	1.67	
					0.63	1.28	1.56	
						1.53		

RMS (%)	1.28
Max (%)	2.22

< nTRACER >

-1.09	-0.77	-0.02	-0.54	-0.10	-0.30	0.50	0.76	0.27
	-0.29	-0.60	0.00	-0.46	0.25	-0.04	0.53	0.22
		-0.04	-0.48	0.27	-0.18	0.57	0.31	0.02
			0.16	-0.24	0.26	-0.22	0.12	0.00
				0.39	-0.24	0.13	-0.08	
					0.32	0.26	0.01	
						0.18		

RMS(%)	0.33
Max (%)	1.09

< nTRACER/PIN >

-2.72	-2.35	-1.38	-1.77	-0.75	-0.76	0.95	1.64	0.65
	-1.59	-2.06	-0.89	-1.30	0.18	0.02	1.43	0.68
		-1.24	-1.54	-0.12	-0.45	1.27	1.29	0.54
			-0.30	-0.71	0.72	0.24	1.16	0.48
				0.69	0.07	1.29	0.77	
					1.41	1.47	0.64	
						0.93		

RMS(%)	1.08
Max (%)	2.72

Figure 3.35 Radial power difference for the 2D core problem (HF1)

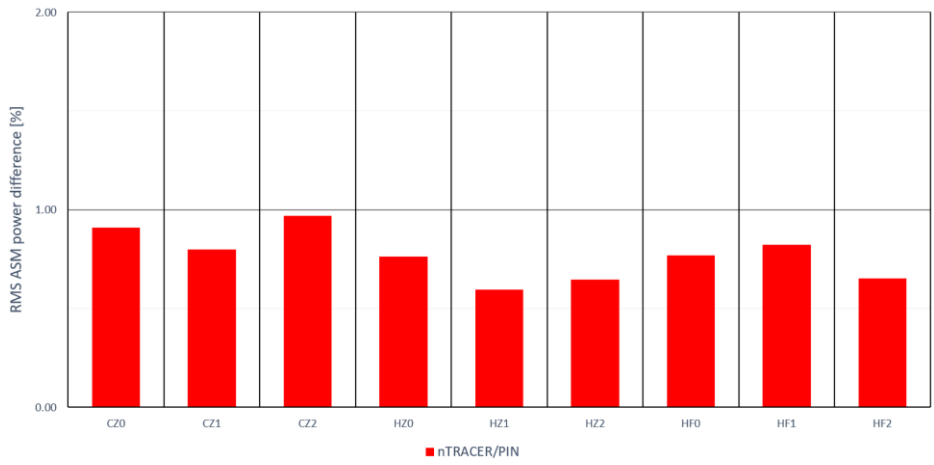

Figure 3.36 RMS Assembly power errors for 2D core problems

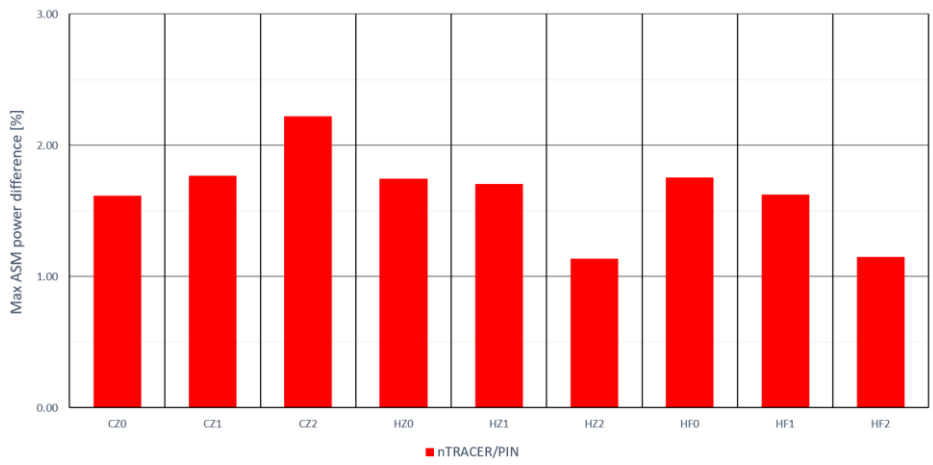

Figure 3.37 MAX assembly power errors for 2D core problems

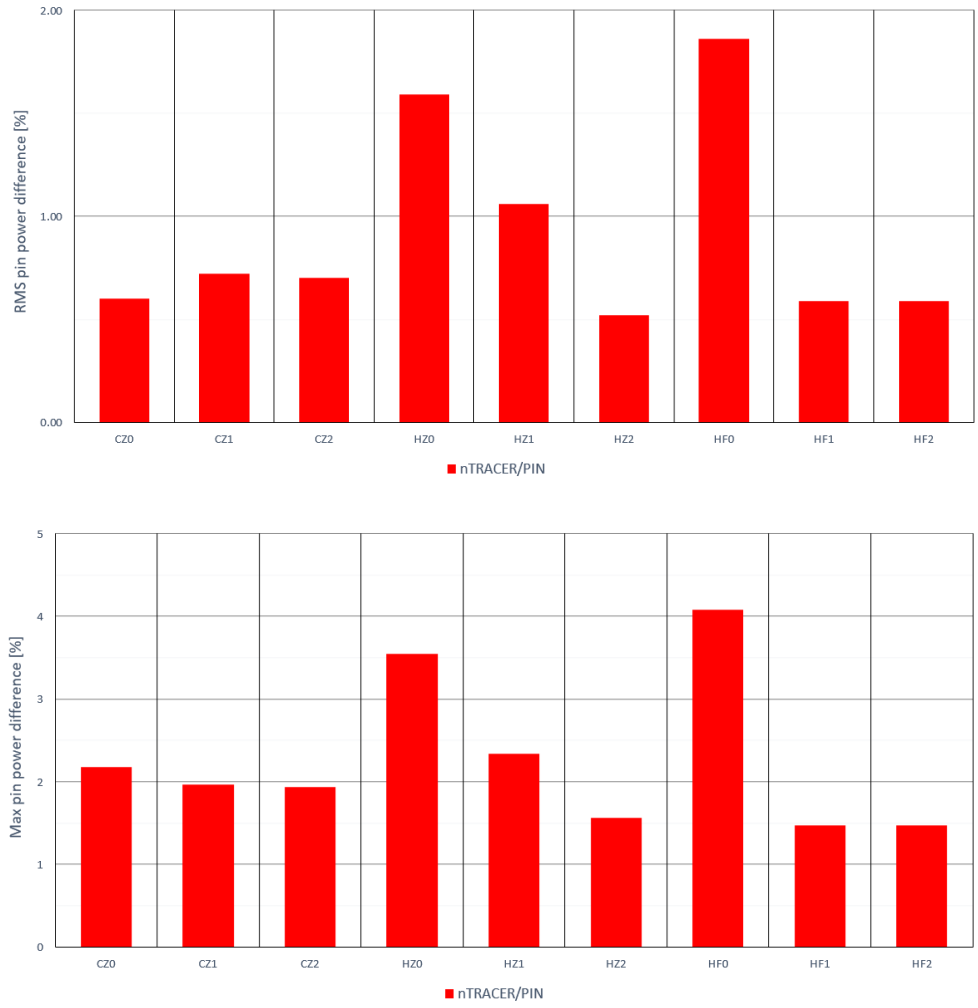

Figure 3.38 RMS and MAX pin power errors for 2D core problems

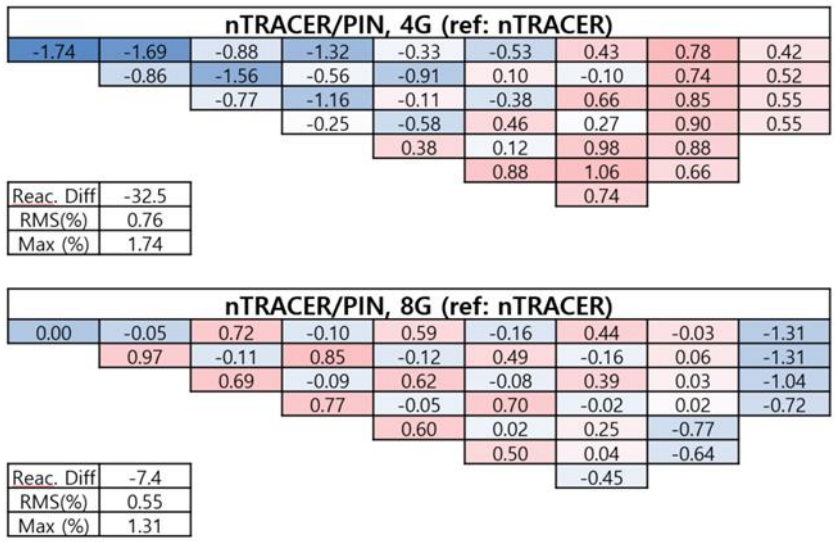

Figure 3.39 Radial Power Difference with 4 and 8 groups

(3) 3D core problems

The 2D core was extended to the axial direction and the moderator-filled axial reflectors and vacuum boundaries were attached to the top and bottom ends of the core. The 3D core problems were also referred by the temperature conditions and the boron concentrations. Like the 2D core problem, reactivity and radial power distributions are compared as the analysis of 3D core problems. First of all, the nTRACER/PIN solutions are compared with the reference solutions which are generated by McCARD as shown in the Figure 3.40 ~ Figure 3.42. The reactivity errors of nTRACER/PIN are about 0 ~ 180

pcm and these values are competitive to the errors of DeCART. The RMS errors of assembly power distributions are under 2% and the maximum errors are about 4% which are also similar values of whole core transport solutions done by DeCART. The reason why errors of nTRACER/PIN solutions are close to them of DeCART is that both of nTRACER cross-section generation and pin-wise calculation provides good solutions. In order to quantify the numerical errors of pin-wise calculation, the solutions of nTRACER/PIN are compared to the nTRACER as shown in the Figure 3.43 ~ Figure 3.45. the reactivity errors are under 50 pcm and the RMS and maximum errors of assembly power distributions are under 1% and 2%.

In 3D calculation, axial power distributions should be verified as well as radial power distributions. Figure 3.46 ~ Figure 3.47 show errors of axial power distributions as comparing with the McCARD reference solutions. nTRACER shows the best overall results with about 1% and 2% of RMS and maximum errors. DeCART shows 1.6% and 3% of RMS and maximum errors which are higher than nTRACER. nTRACER/Pin solutions also show 1.5% and 3% of RMS and maximum errors which are close to DeCART. Figure 3.48 and Figure 3.49 show the nTRACER/PIN results as considering the nTRACER to the reference solutions. In the figures, the RMS and maximum errors are about 1% and 2%. In order to estimate the solutions in detail, axial power distributions of the CZ1 problem in which errors of is highest are

compared as shown in Figure 3.50. It is observed that the axial power distribution of nTRACER/PIN is very close to that of nTRACER.

The whole core pin power distributions are evaluated as comparing the results of nTRACER/PIN to the results of nTRACER. The 3D pin power distributions are axially integrated to generate radial pin power distributions and then the 2D distributions are compared. As shown in Figure 3.51 and Figure 3.52, the RMS and maximum errors are around 1% and 2% which are good solutions in cases of HZ and HF. However, the errors are around 2% and 4% in cases of CZs in which the temperatures are very low and the peripheral powers are high since the errors become higher in reflector interfaces.

These overall results show pin-wise calculations are treated as a good solution for 3D core calculations when the pin-wise cross-sections are properly provided.

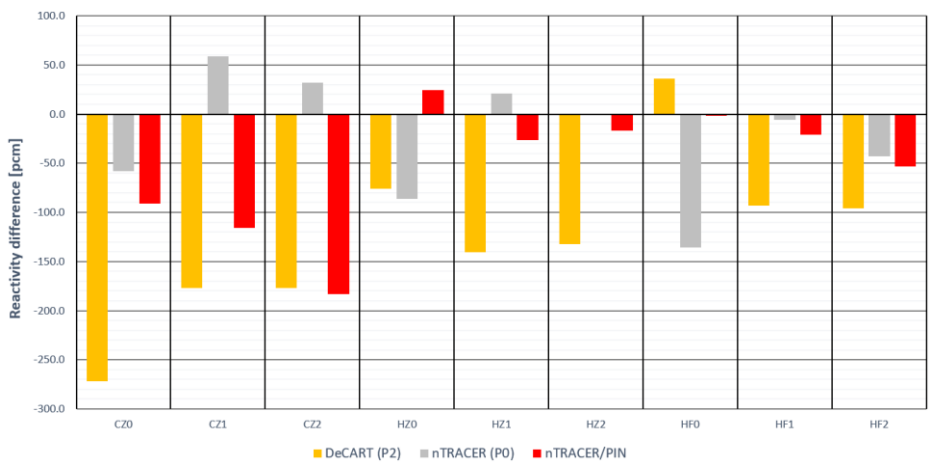

Figure 3.40 Reactivity diff. for 3D core prob. (Ref: McCARD)

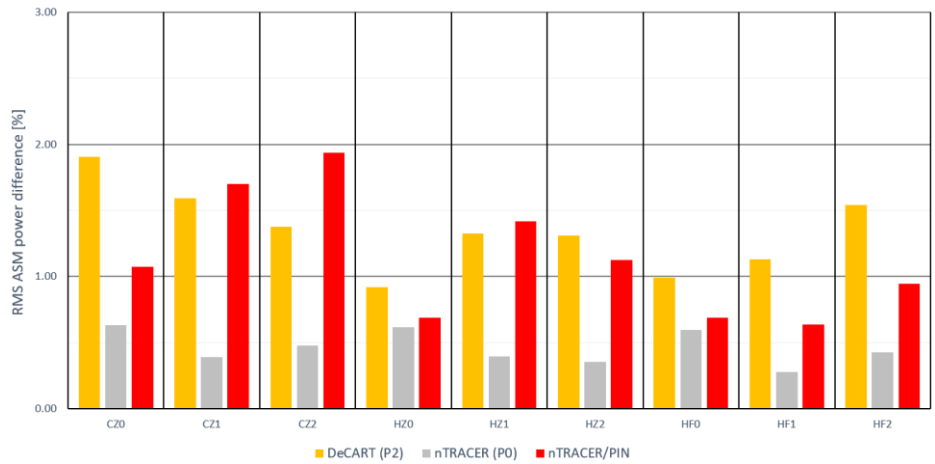

Figure 3.41 RMS ASM 2D Power diff. for 3D core prob. (Ref: McCARD)

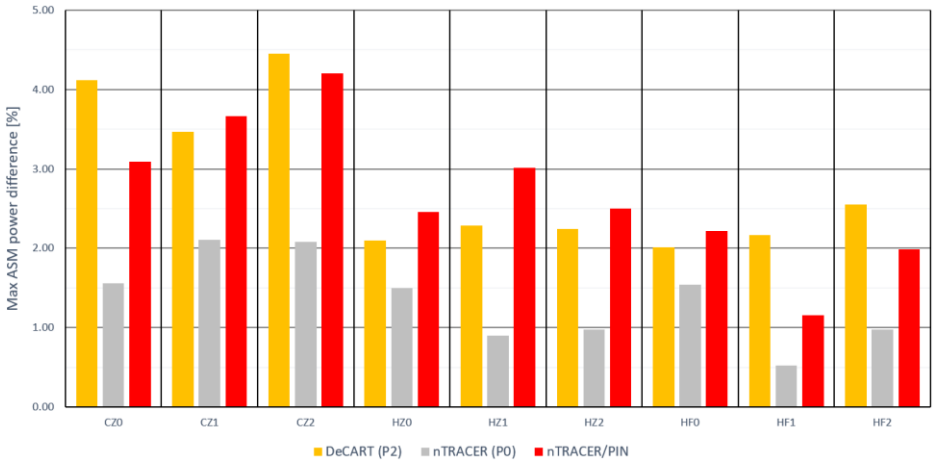

Figure 3.42 Max ASM 2D Power diff. for 3D core prob. (Ref: McCARD)

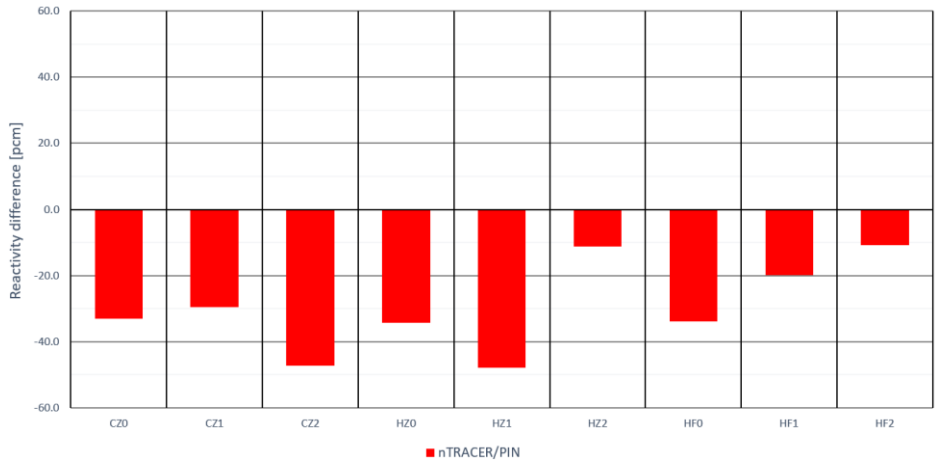

Figure 3.43 Reactivity diff. for 3D core prob. (Ref: nTRACER)

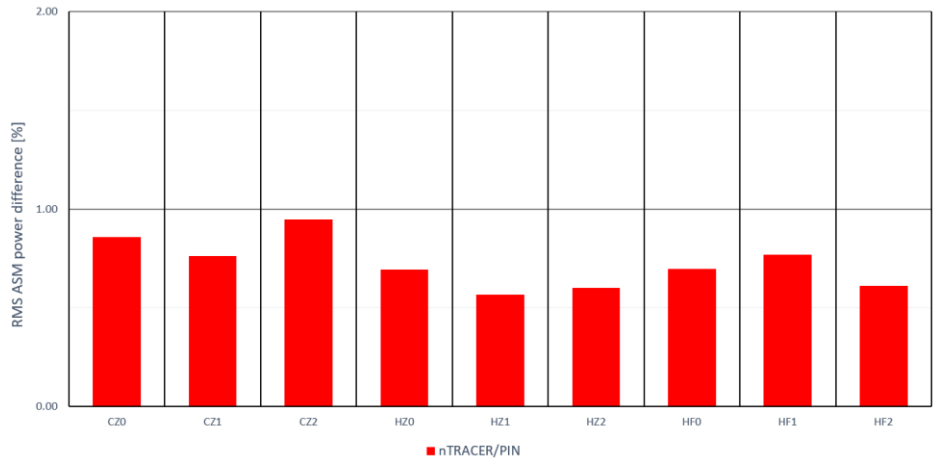

Figure 3.44 RMS ASM 2D power diff. for 3D core prob. (Ref: nTRACER)

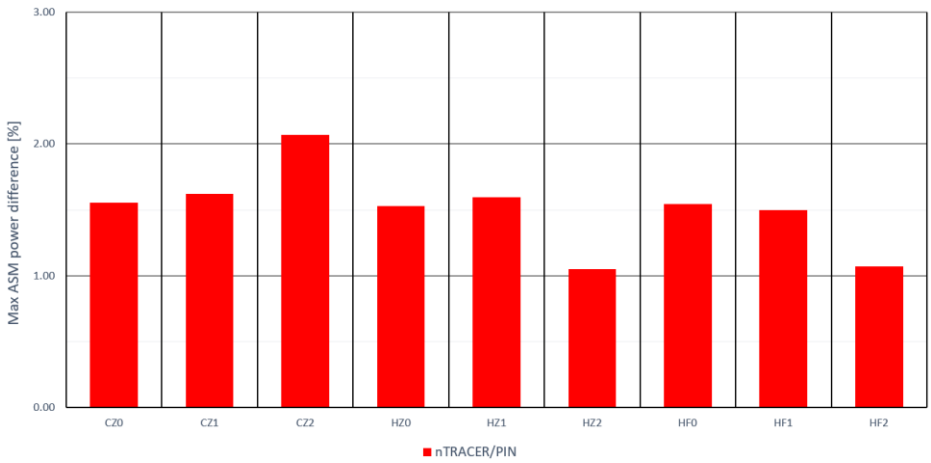

Figure 3.45 Max ASM 2D power diff. for 3D core prob. (Ref: nTRACER)

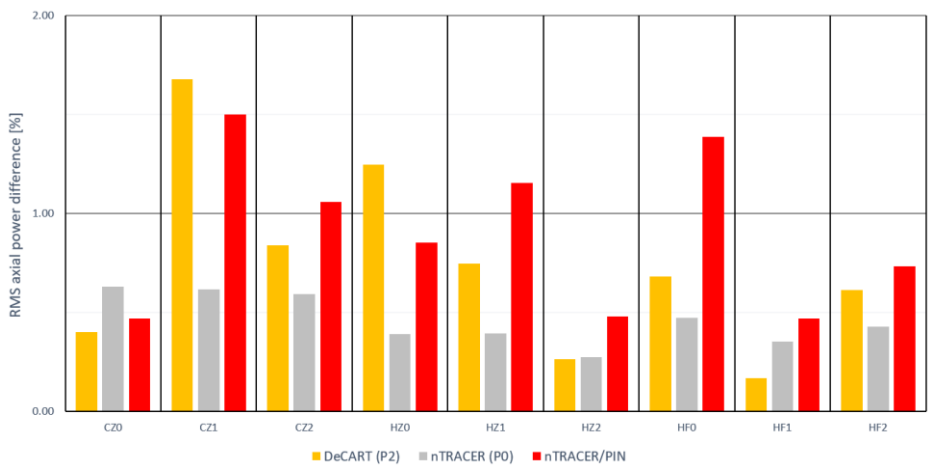

Figure 3.46 RMS axial power diff. for 3D core prob. (Ref: McCARD)

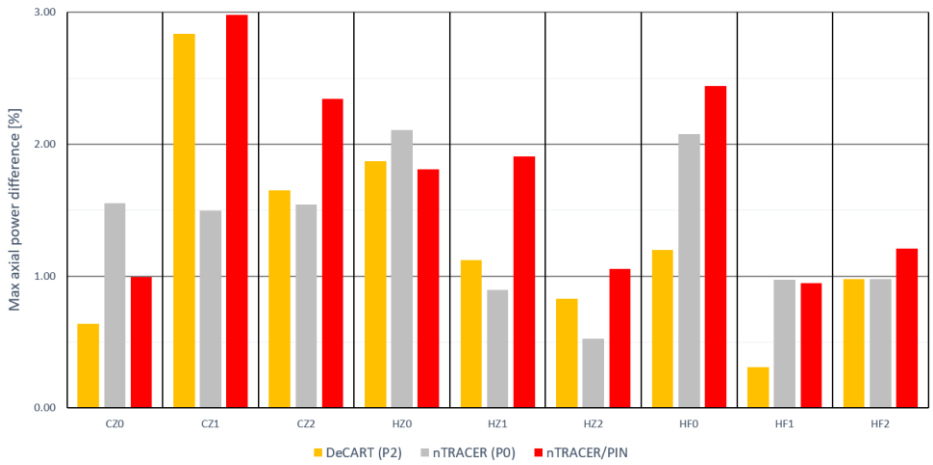

Figure 3.47 MAX axial power diff. for 3D core prob. (Ref: McCARD)

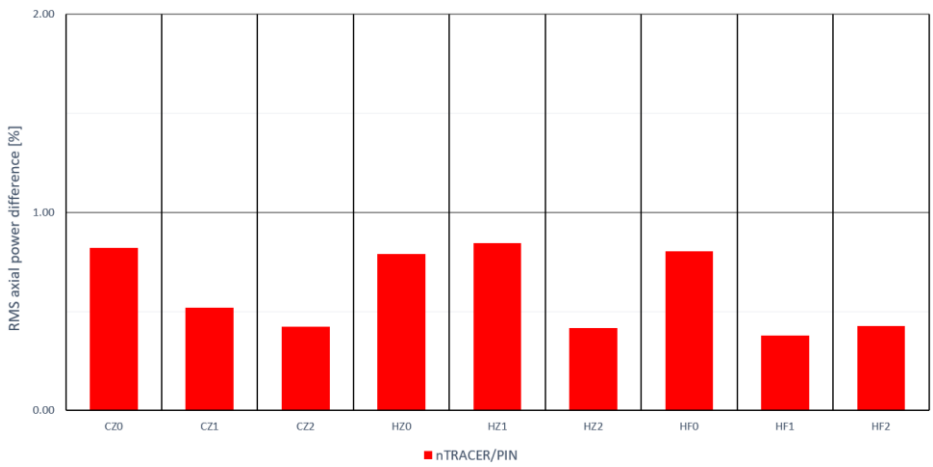

Figure 3.48 RMS axial power diff. for 3D core prob. (Ref: nTRACER)

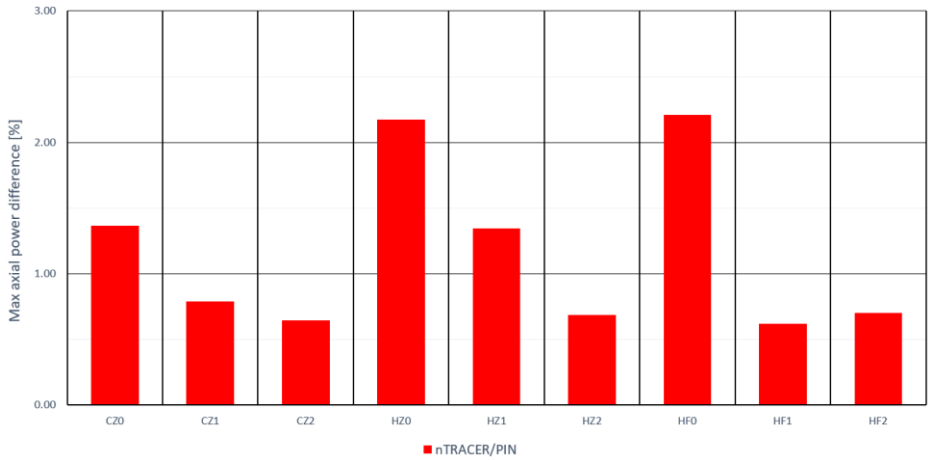

Figure 3.49 MAX axial power diff. for 3D core prob. (Ref: nTRACER)

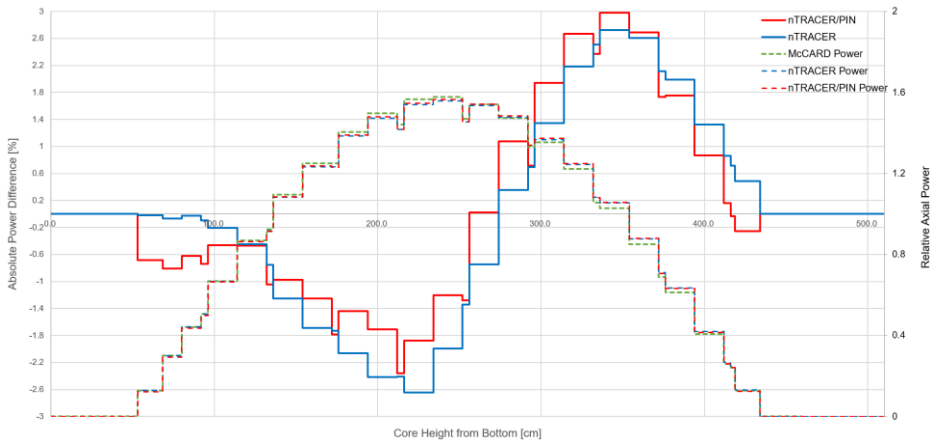

Figure 3.50 Axial power dist. and errors for 3D CZ1 prob.

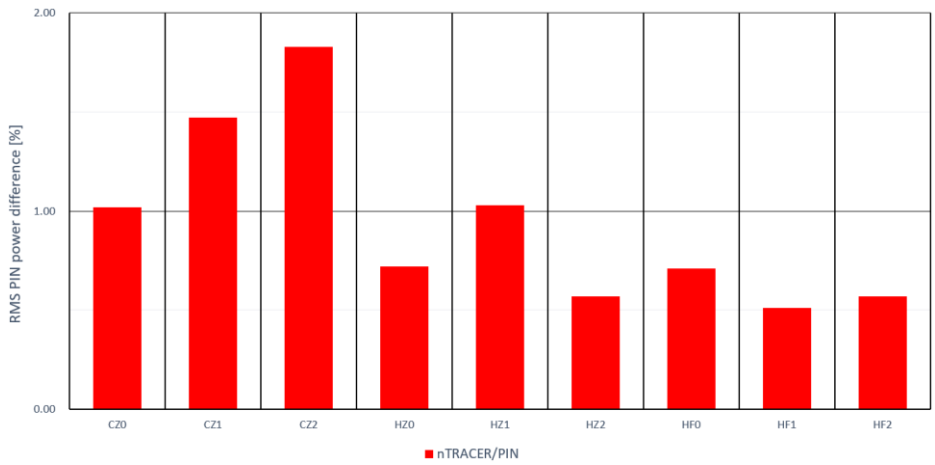

Figure 3.51 RMS pin power diff. for 3D core prob. (Ref: nTRACER)

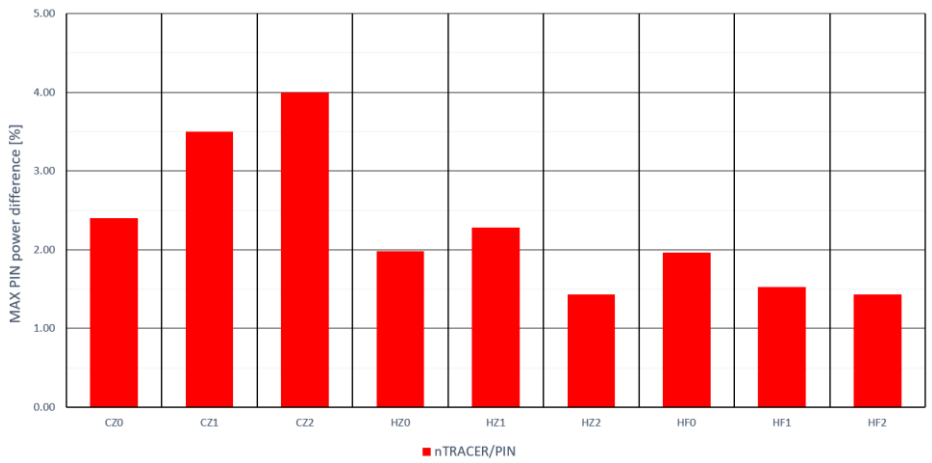

Figure 3.52 MAX pin power diff. for 3D core prob. (Ref: nTRACER)

(4) Control rod worth

The control rod worth calculations were performed by inserting the control rod bank 5, 4, 3, 2, 1, B and A sequentially under the fixed temperatures and boron concentration conditions. The accumulated worth means the total rod worth of the all inserted control banks and the group worth means the increase of accumulated worth by a newly inserted control bank. In case of the 5-4-3, for example, the accumulated worth is the reactivity difference between the 5-4-3 bank insertion case and the ARO core, while group worth is difference of accumulated worth between the 5-4-3 bank insertion case and the 5-4 bank insertion case. Table 3-20 shows the results of the control rod worth calculations and Figure 3.53 and Figure 3.54 show errors of the accumulated and group worth. The solutions of pin-wise calculations have errors of -1 ~ +1% to the reference solutions of McCARD for the accumulated control word worth. Comparing with errors of nTRACER and DeCART, the errors of pin-wise calculations are also sufficiently low. Referring to nTRACER solutions, errors of accumulated control rod worth are around 0.5%. Errors of group-wise control rod worth are also under 2% and 1.5% with the reference solutions of McCARD and nTRACER, respectively.

Figure 3.55 and Figure 3.56 show the RMS and maximum errors of radial assembly power distributions for the rod-insertion cases with the

reference solutions of McCARD. Similar to the calculation of the unrodded cases which are introduced in the previous results, the RMS difference is less than 1.5 %, and the MAX difference is less than 4 %. As referring the nTRACER solutions, the RMS and maximum errors are around 1% and 2% which are slightly higher than the unrodded cases. Figure 3.59 and Figure 3.60 show the RMS and maximum errors of axial power distributions. Comparing to nTRACER solutions, the RMS and maximum errors are under 1% and 2%. These values are similar to the unrodded cases. Figure 3.62 shows the RMS and maximum errors of pin power distributions which are gradually increased as inserting banks sequentially since the flux gradients are severe as inserting banks. In conclusion, as summing up results of the rodded cases, the pin-wise calculations show the good solutions which have similar accuracy comparing to the unrodded cases even though the local heterogeneity are stronger due to the rod insertions.

Table 3-20 Individual CEA Worth

Inserted Bank (pcm)	McCARD		DeCART		nTRACER		nTRACER/PIN	
	Acc.	Grp.	Acc.	Grp.	Acc.	Grp.	Acc.	Grp.
5	369.0	369.0	370.3	370.3	365.4	365.4	365.0	365.0
5-4	691.7	322.7	696.7	326.4	686.9	321.5	691.0	326.0
5-4-3	1691.1	999.4	1704.9	1008.2	1687.2	1000.3	1687.9	996.9
5-4-3-2	2733.0	1041.9	2753.6	1048.7	2726.0	1038.8	2721.2	1033.3
5-4-3-2-1	4743.0	2010.0	4762.4	2008.8	4723.7	1997.7	4693.8	1972.5
5-4-3-2-1-B	8885.2	4142.2	8982.8	4220.4	8849.5	4125.8	8838.9	4145.1
5-4-3-2-1-B-A	16119.2	7234.0	16241.3	7258.5	15987.0	7137.6	15957.7	7118.7

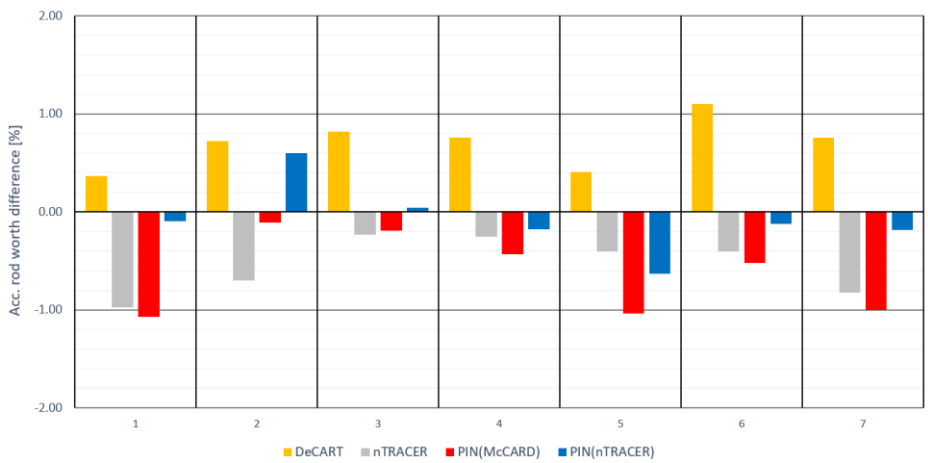

Figure 3.53 Errors of accumulated control rod worth

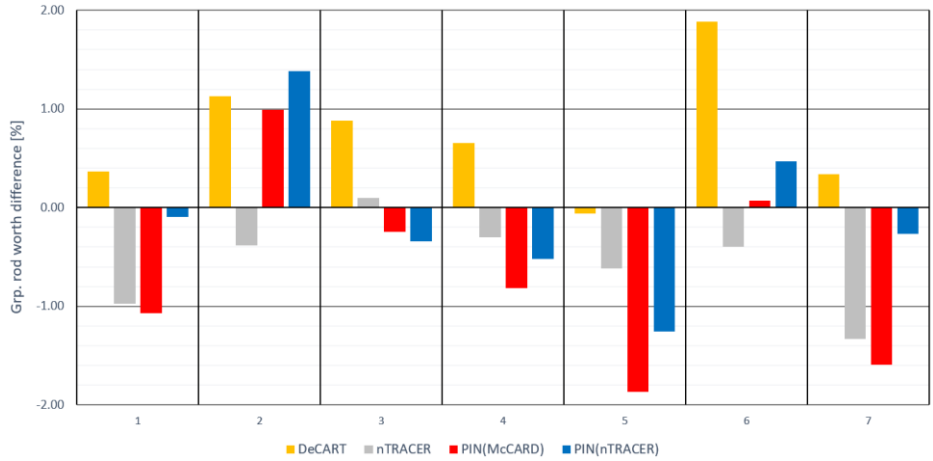

Figure 3.54 Errors of group control rod worth

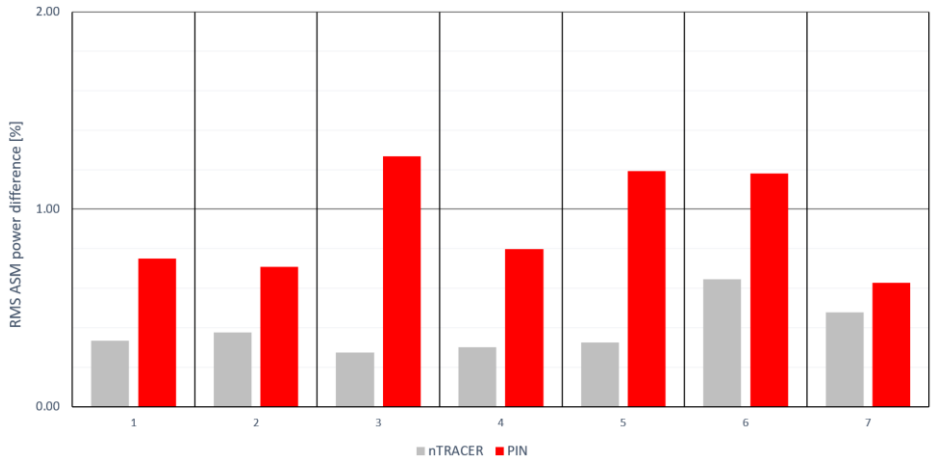

Figure 3.55 RMS ASM 2D power diff. for rod-in prob. (Ref: McCARD)

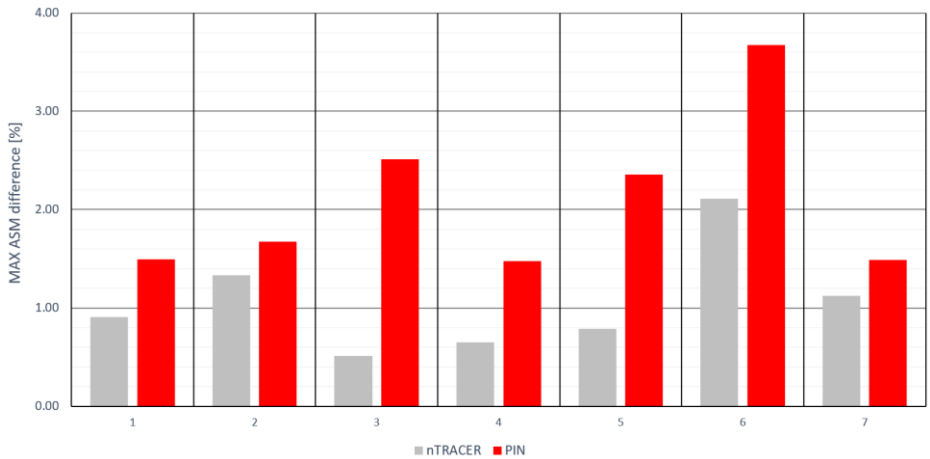

Figure 3.56 MAX ASM 2D power diff. for rod-in prob. (Ref: McCARD)

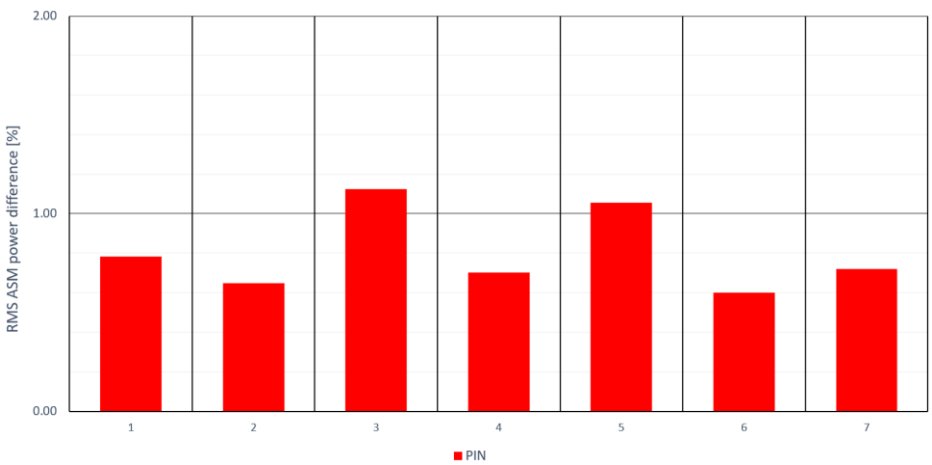

Figure 3.57 RMS ASM 2D power diff. for rod-in prob. (Ref: nTRACER)

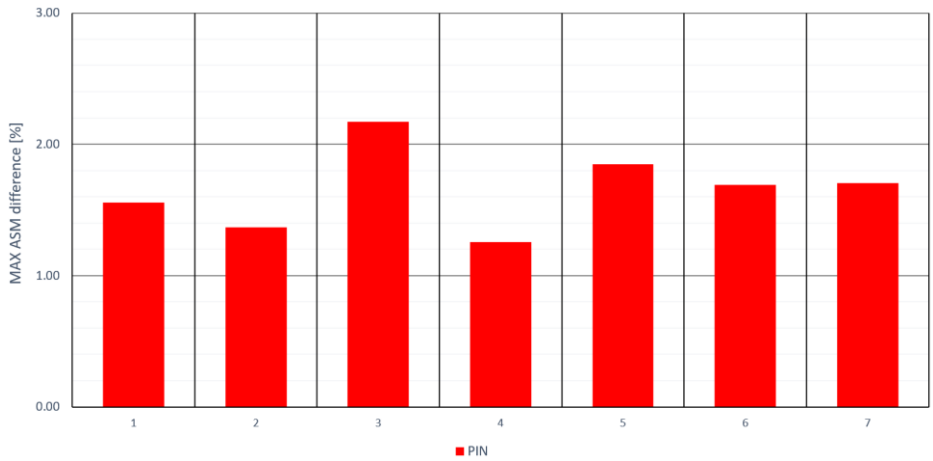

Figure 3.58 MAX ASM 2D Power diff. for rod-in prob. (Ref: nTRACER)

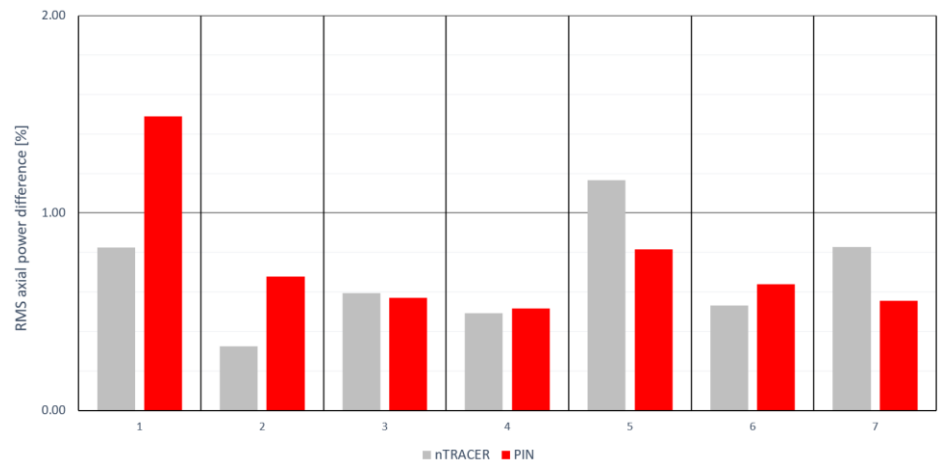

Figure 3.59 RMS ASM axial power diff for rod-in prob.

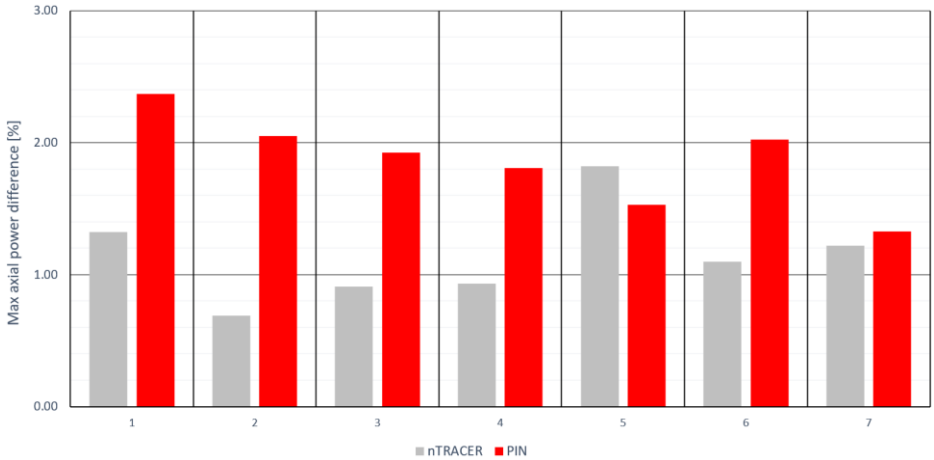

Figure 3.60 MAX ASM axial power difference for rod-in prob.

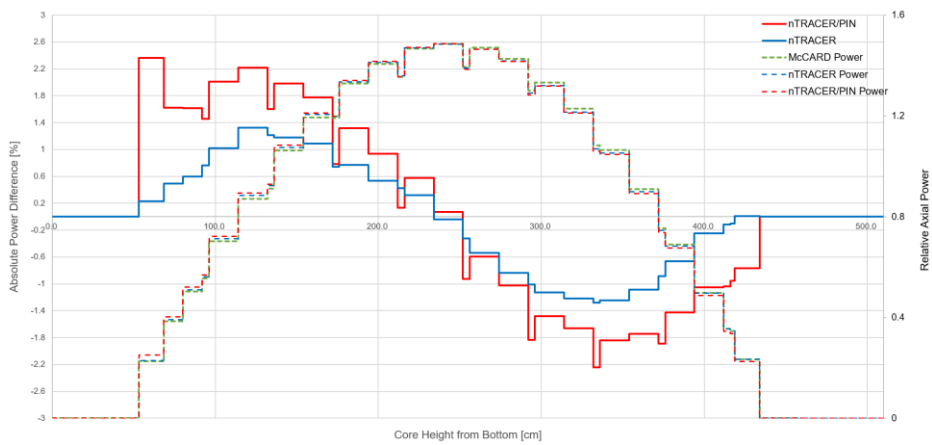

Figure 3.61 Axial power distributions for R5-in case

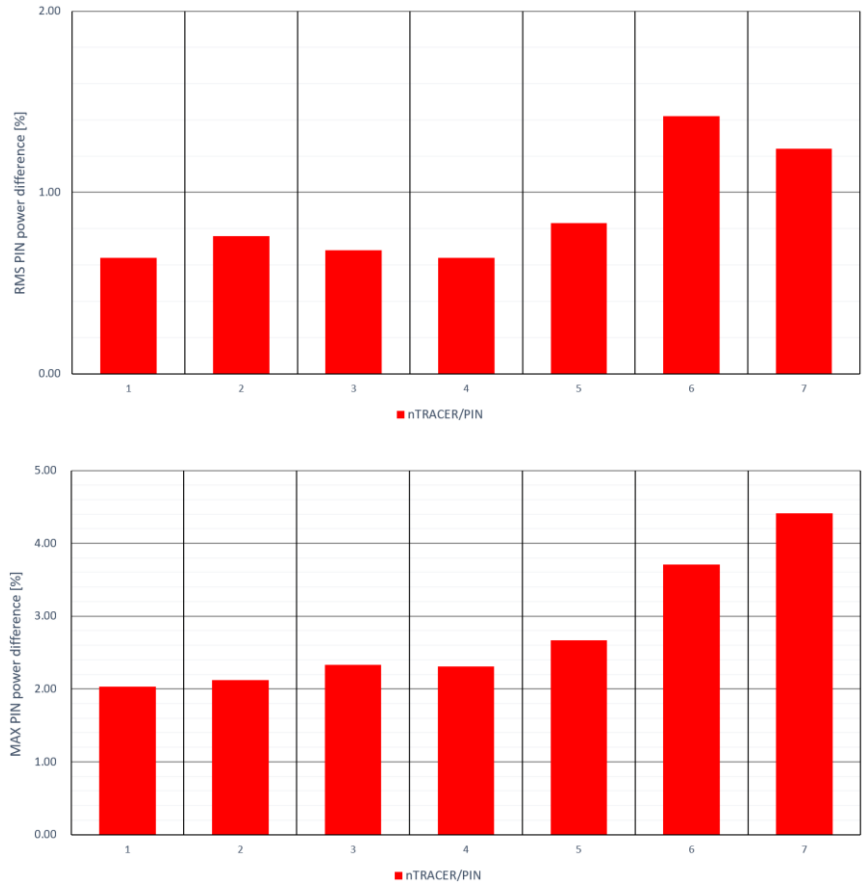

Figure 3.62 pin power errors for rod-in prob. (Ref: nTRACER)

3.5.4 Calculation Performance

In order to calculate the 3D APR1400 problems, the 241 fuel assemblies and 72 artificial reflector assemblies should be considered. Since the number of total rods is 80,128 and the number of axial planes are 36, the total number of 3D nodes becomes 2,884,608. Thinking of four energy groups, the matrix size is over 11 million by 11 million. Solving this linear system directly is not practical because lots of computing resource should be consumed and calculation time is too long. In order to maximize the calculation performance, the 2D/1D decoupling method is introduced in this work and the planar and axial parallelization is implemented. Moreover, the two-level CMFD acceleration is adopted. As a result of 2D/1D parallelization and CMFD acceleration, the computing time of 2D and 3D quarter-core calculations is shown in Table 3-21. 36 threads are used to maximize parallelization of planar 2D calculations. The computing time of the 2D calculation is 5.5 seconds with the CMFD acceleration whereas the calculation without the CMFD acceleration takes 7 times longer. The time reduction is mainly coming from reducing iteration count of the pin-wise 2D/1D calculation. 3D calculation also shows the calculation with CMFD acceleration is 3.5 times faster than otherwise. The best computing time of the 3D quarter-core calculation is about 25 seconds and this computing performance is sufficient to apply pin-wise calculation to the commercial nuclear design process.

Table 3-21 Computing time of APR1400 problems

	CMFD	Pin 2D/1D Iter.	CMFD Iter.	Time (sec)	Time/Iter. (sec)
2D	w/o CMFD	230	-	38.98	0.169
	w/ CMFD	31	250	5.5	0.177
3D	w/o CMFD	243	-	93.54	0.384
	w/ CMFD	47	250	25.63	0.545

- Hardware Spec. : 96 Core (Intel Xeon SPP-9242/2.3Gh-48C * 2ea), 384GB (RECC DDR4-2933)
- Operation System : CentOS 7.1

3.6. SPERT III E-Core Transient Calculation

The Special Power Excursion Reactor Test III (SPERT III) reactor [22] is a pressurized-water, nuclear-research reactor which has been constructed to provide a facility for conducting reactor kinetic behavior and safety investigations. The investigations are designed to provide information for the advancement of pressurized-water and boiling-water reactor technology and safety. The facility has been designed for operation up to pressures of 2500 psia, temperatures of 650°F, and flows of 20,000 gpm and incorporates essential features typical of pressurized-water and boiling-water reactors. The original report was published in 1961 and the updated report describing the engineering features of the reactor and supporting process equipment with the E-core and other modifications was published in 1965. Especially, the E-Core of the SPERT III facility is a kind of PWR since the UO2 fuels, moderator of light water, coolant flow rate and core pressure are typical to PWR and the various tests of RIA ejections covering up to super-prompt critical tests were performed. In this work, the super-prompt critical tests in the various initial conditions are evaluated in order to validate the transient 2D/1D decoupling method.

3.6.1 Modelling for nTRACER calculation

The E-core geometry is shown in the Figure 3.64. The rated core thermal power is 20MW, the rated flow speed is 14.0 fps and the pressure is 1500 psia. The UO2 fuel rod used in the experiment is same to the commercial one except using the stainless steel (SUS348) for the cladding. The enrichment of U235 is 2.8 w/o and the stack density of fuel rod is 10.5g/cm3. The gap between fuel pellets and cladding is filled with the helium gas. The detail structure is shown in the Figure 3.63.

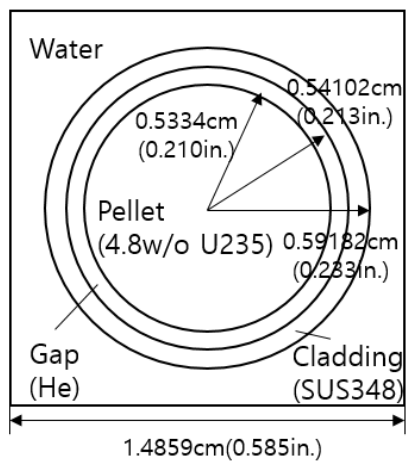

Figure 3.63 Structure of the fuel cell (SPERT III E-Core)

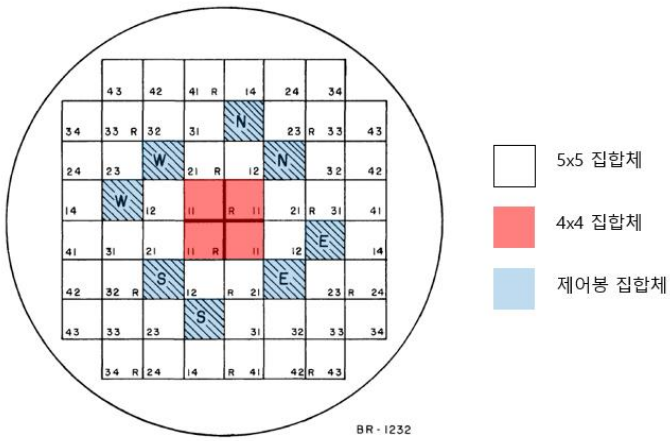

Figure 3.64 Geometry of the SPERT III E-Core

There are three assembly types in the core. As shown in the Figure 3.65, the first assembly type is a normal 5X5 fuel assembly. There are 25 fuel rods with the cell pitch of 1.4859cm in the assembly. The stainless-steel channel box surrounding the fuel rods blocks the cross flow from neighboring assemblies. In the top, bottom and middle positions of the fuel assembly, the spacer grids exist to maintain the geometry. The middle spacer grids are located in 33.02cm and 67.31cm apart from the bottom grid. The second assembly type is a 4x4 fuel assembly and the four assemblies are located in the core center. Different from the 5x4 fuel assembly, the 4x4 fuel assembly has 16 fuel rods. Moreover, the cruciform transient control rod is located in the center of the four assemblies as shown in the Figure 3.66.

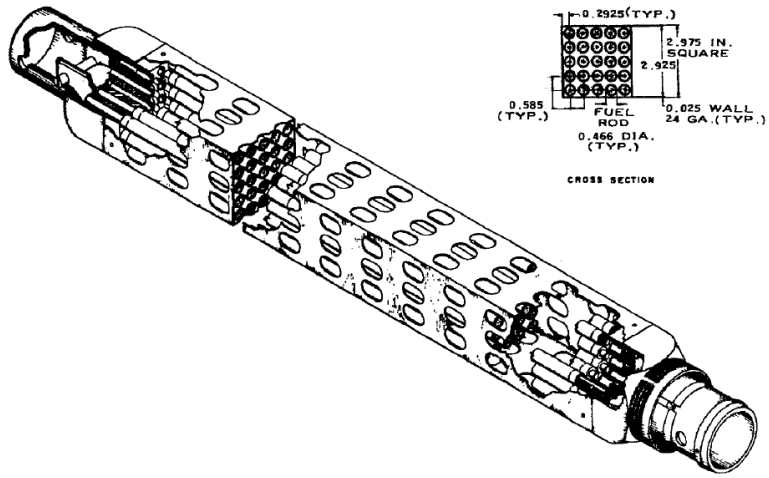

Figure 3.65 5x5 fuel assembly of SPERT III E-Core

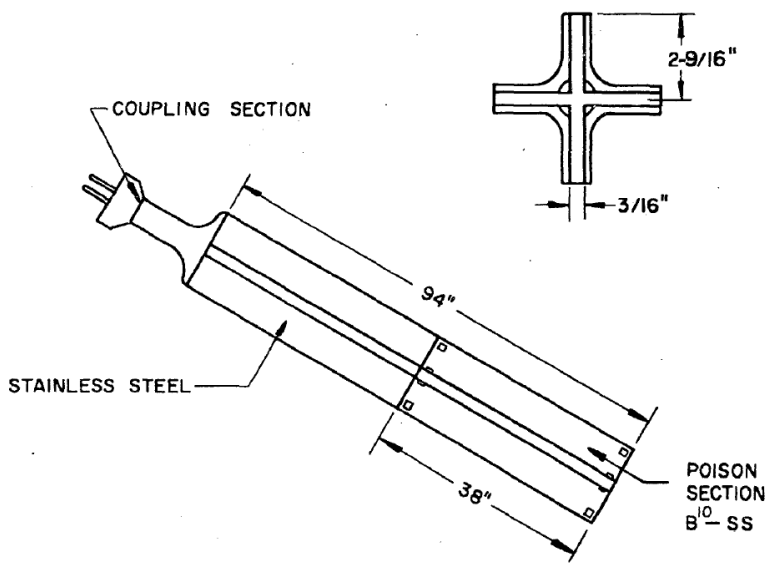

Figure 3.66 Crucial-form transient control rod (SPERT III)

The third assembly type is a static control assembly. There are 8 control assemblies in the core and they are used for maintain core to critical in the steady-state condition. The assembly is composed of the poison section of upper part and the fuel section of lower part as shown in the Figure 3.67. In the poison section, the square region of 6.30cm is filled with B10 and it is surrounded by the 0.47cm-thick stainless steel. The fuel section which is upper part of the assembly has same structure of the 4x4 fuel assembly. There is a flux suppressor between lower and upper part and the shape is similar to the spacer grid and the material is B10.

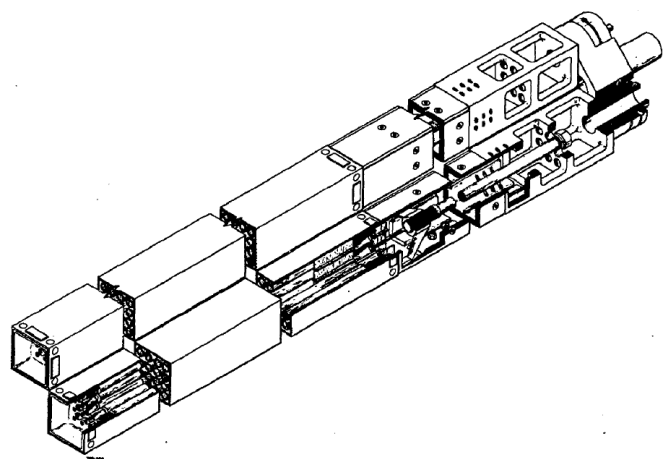

Figure 3.67 A pair of control assemblies (SPERT III)

Since the assembly geometry is quite different from the general one of commercial PWRs, the procedure generating cross-section is quite different from the typical lattice calculation. Instead of the lattice calculation, the three-

dimensional nTRACER calculation is done to generate pin-wise cross-sections for the pin-wise calculation. In order to consider three types of assemblies, each of fuel pins with moderator is composed of four cells as shown in the Figure 3.68.

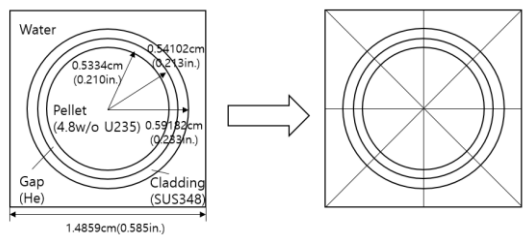

Figure 3.68 Four cells for one fuel pin-cell (SPERT III)

The width of all the assembly types is identically 7.62cm, the axial length is 120.0cm including 10.912cm and 11.806cm of bottom and top structures. 92.282cm of the active fuel length is divided into nodes of 5.99cm except the bottom node of 7.432cm. The 5x5 fuel assembly is modelled as shown in the Figure 3.69. The end plug and spacer grids are identically modelled with the 10x10 pin-cell geometry. The channel box surrounding the assembly is homogenized into the peripheral cells.

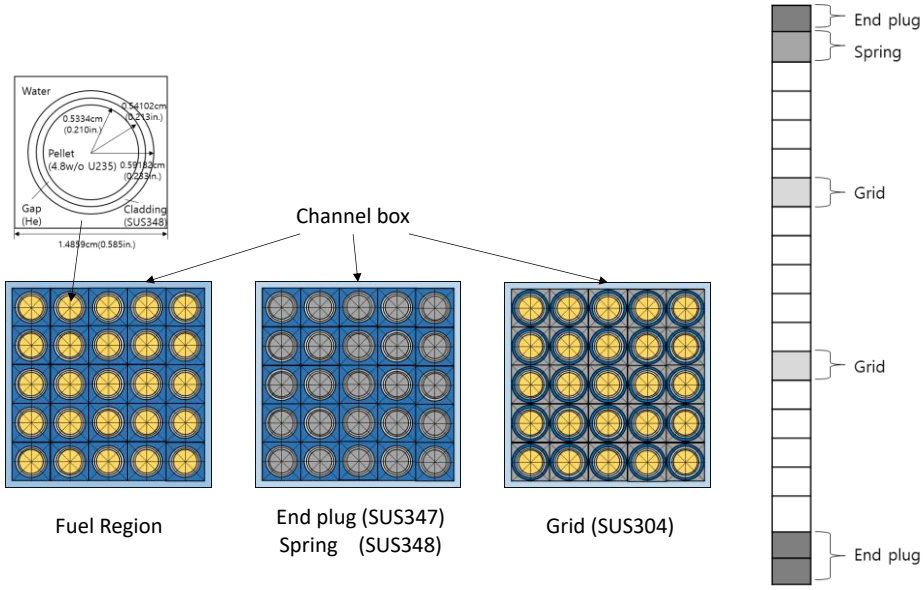

Figure 3.69 modelling 5x5 fuel assembly (SPERT III E)

As the 4x4 fuel assembly is composed of the upper fuel part and lower poison part, the two parts are independently modelled. Different from the 5x5 fuel assembly, the channel box and the cruciform control rod are explicitly modelled with 4x4 fuel pins as maintaining 10x10 pin-cell geometry as shown in Figure 3.70.

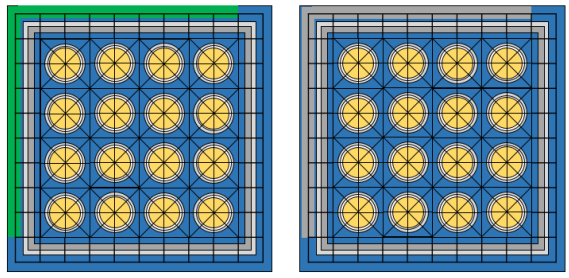

Figure 3.70 the pin-cell modelling of the 4x4 assembly (SPERT III)

The control assembly is composed of the lower fuel part, the middle flux suppressor and the upper poison part. The fuel part geometry is same to the 4x4 fuel assembly except the cruciform control rod. The flux suppressor has same geometry, yet with different materials which is specified in the reference with their volumes. The fuel rod region is substituted with stainless steel (SUS348) and the outer region is filled with the mixture of 18-8 stainless-steel and 1.35% B-10. The upper part is filled with the mixture of 18-8 stainless steel and 1.35% B-10.

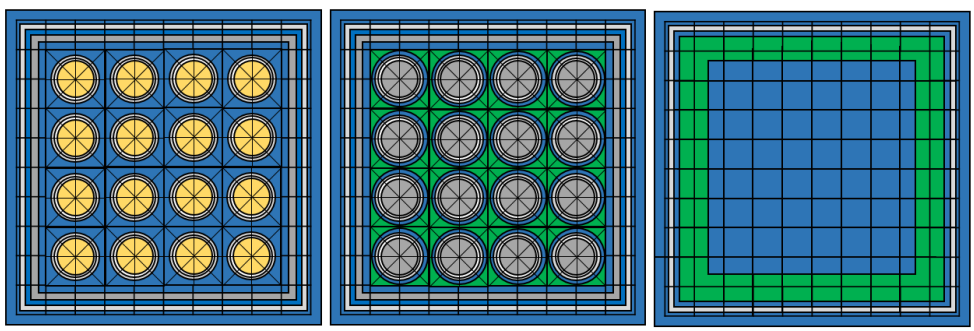

Figure 3.71 the pin-cell modelling of the control assembly (SPERT III)

There are various shaped fillers in the reflector region and the light water flows through the fillers. This fillers and moderator regions are explicitly modelled. The outside of the core is assumed to the stainless steel (SUS304) the geometry of reflector is shown in the Figure 3.72.

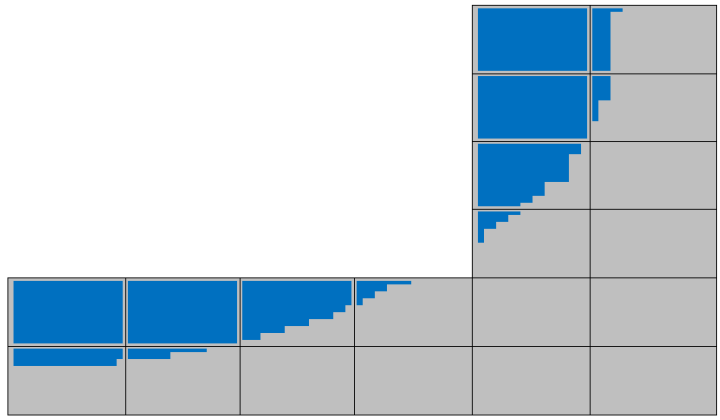

Figure 3.72 the reflector modelling (SPERT III)

3.6.2 Generation of the pin-wise cross-section

In general, the pin-wise cross-sections are generated with the lattice calculation as describing in the calculation method. However, the cross-sections are generated from the whole core transport calculation with nTRACER since the purpose of this work is to evaluate the transient calculation itself not including the procedure for generation of pin-wise cross-section.

In order to generate the pin-wise cross-sections for each case, the three-dimensional transport whole core calculation is done with the modelling of SPERT III E-Core. Then, the pin-wise cross-sections are generated with the homogenization process. Different from the typical pin-wise homogenization process, the SPH factors are not considered in this process for only focusing

the transient calculation.

The cross-section is defined as a function of control assembly and transient rod positions, fuel temperature and moderator temperature as shown in the following.

$$\Sigma_x = \Sigma_{x,ARO} + \delta\Sigma_{x,CA} + \delta\Sigma_{x,TR} + \frac{d\Sigma_{x,TF}}{dTF}(TF - TF_0) + \frac{d\Sigma_{x,TM}}{dTM}(TM - TM_0)$$

where

x : Reaction type,

$\Sigma_{x,ARO}$: cross-section in all rod out condition,

$\delta\Sigma_{x,CA}$: cross-section whether the control assembly are inserted or not,

$\delta\Sigma_{x,TR}$: cross-section whether the transient rods are inserted or not,

$\frac{d\Sigma_{x,T_F}}{dT_F}$: derivative coefficient for fuel temperature variation,

$\frac{d\Sigma_{x,T_M}}{dT_M}$: derivative coefficient for moderator temperature variation,

TF_0 : reference fuel temperature,

TM_0 : reference moderator temperature,

TF : fuel temperature, and

TM : moderator temperature.

The control assembly delta cross-section ($\delta\Sigma_{x,CA}$) is generated from the

steady-state calculation as inserting control assemblies step-by-step. With the gradually insertion of the control assemblies, the three-dimensional pin-wise homogeneous cross-sections are generated for each axial position. Then the delta cross-section of each position is obtained as the following.

$$\delta\Sigma_{x,CA_i} = \Sigma_{x,CA_i} - \Sigma_{x,ARO}$$

In pin-wise core calculations, the actual delta cross-section according to a position of control assemblies is obtained as interpolating the delta cross-sections of the adjacent axial positions as the following.

$$\delta\Sigma_{x,CA} = f \times \delta\Sigma_{x,CA_i} + (1-f) \times \delta\Sigma_{x,CA_{i-1}}$$

The transient rod delta cross-section ($\delta\Sigma_{x,TR}$) is also generated as following the same procedure of control assembly.

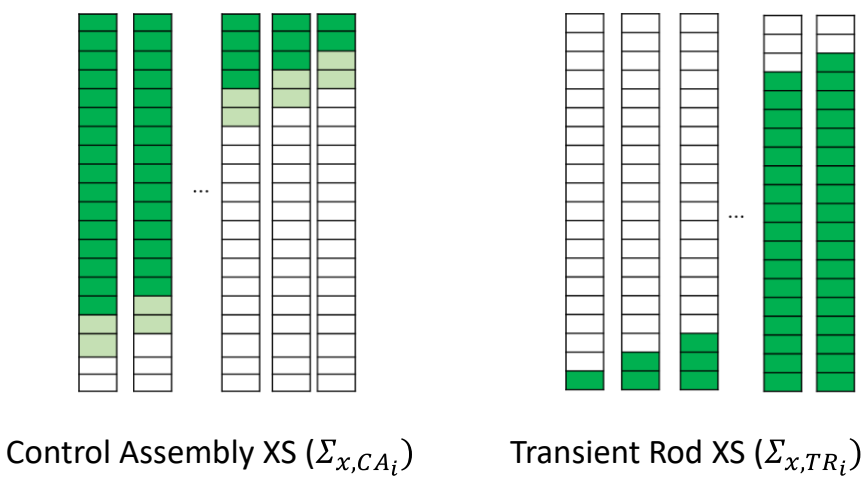

Figure 3.73 Axial positions of CA and TR for cross-section generation

The derivative cross-section terms of fuel temperature and moderator temperature are generated as following the typical procedure.

$$\frac{d\Sigma_{x,T_F}}{dT_F} = \frac{\Sigma_{x,TF} - \Sigma_{x,TF_0}}{\sqrt{TF} - \sqrt{TF_0}}, \frac{d\Sigma_{x,T_M}}{dT_M} = \frac{\Sigma_{x,TM} - \Sigma_{x,TM_0}}{TM - TM_0}$$

3.6.3 Numerical results

The five test cases of the SPERT III E-Core is chosen among over 100 test cases and they are all super-prompt critical problems which are desired for evaluating transient pin-wise calculations as shown in Table 3-22. Since the initially inserted reactivity is 1.17~1.23$, the core power should be rapidly increased within a second.

Table 3-22 Test Cases for SPERT III E-Core Transient calculation

Test No.	Initial Power (MW)	Reactivity ($)	Inlet Temp. (°F)	Flow Rate (gpm)	Max. Core Power (MW)	Max. Time (s)
60	$5x10^{-5}$	1.23±0.05	500±4	12000	410±41	0.227±0.005
81	1	1.17±0.04	504±4	12000	330±30	0.135±0.003
86	20	1.17±0.05	502±4	12000	610±60	0.110±0.005

The pin-wise two-group cross-sections for the test cases are generated with the given conditions in Table 3-23. The control assembly and transient

rod cross-sections are also generated in the reference core conditions of each test.

Table 3-23 Conditions of cross-section generations

Test No.	Pressure (MPa)	Fuel Temperature (C)	Moderator Temperature (C)	Flow Rate (kg/s)	Initial Power (MW)
60	10.44	260, 560	260, 265	582.5	$5x10^{-5}$
81	10.44	260, 560	260, 265	582.5	1
86	10.44	468.6, 768.6	263.9, 268.9	582.5	20

- Underlined values are reference conditions.

Once the cross-sections are prepared, the kinetic parameters such as delayed neutron fraction, decay constant and neutron velocity are obtained from the test 60 as shown in the Table 3-24.

Table 3-24 Kinetic parameters of the test 60 (SPERT III)

Precursor Group	Delayed neutron fraction(pcm)	Decay constant
1	2.21068E-04	0.0128
2	1.22515E-03	0.0318
3	1.20809E-03	0.1190
4	3.54989E-03	0.3181
5	1.15646E-03	1.4027
6	3.83279E-04	3.9289

* neutron velocity : 1.83058E+07 cm/s (fast), 3.86983E+05 (thermal)

The pin-wise core calculation is done with the following process. As the initial control assembly and transient rod positions which can keep the core critical steady state are not given in the benchmark reference but the reactivity to be inserted, the positions should be found to satisfy the initial critical of the core and the inserted reactivity by rod ejection.

1) Find a position of the control assemblies to make core critical with the transient rod out.
2) Find a position of the control assemblies to have excess reactivity in steady-state calculation.
3) Find a position of the transient rod to make core critical.

With the above process, the proper reactivity is inserted into the core when the transient rod is out during transient calculation. As following the process, the initial control assemblies and transient rod positions are determined as shown in the following table. It is noted that the hot-standby(81) and hot-full-power cases(86) find a position of the control assemblies having excess reactivity from the transient calculation (no feedback) in the second step because the position of steady-state calculation includes the fuel and moderator temperature feedback effects.

Table 3-25 Initial positions of CA and TR (SPERT III)

Test No.	Control Assembly[cm]	Transient Rod[cm]
60	76.993	30.074
81	77.054	29.649
86	83.224	31.682

The results of the tests are shown in the. In the hot-zero-power case, the benchmark calculations show 400~450% of peak core powers with the reference power is 415%. The pin-wise result (nTRACER/PIN) shows very close to the transport result (nTRACER) with the difference of about 10% core power. The hot-standby results also show the similar peak core powers even though the peak time is slightly different (0.01 sec). In the hot-full power case, the difference of peak core powers about 40% is reasonable with the core power increases very high due to initial full power and super-prompt critical state. Since the cross-sections are generated from the nTRACER calculation, it is desirable that the pin-wise results follow the transport results. The figures show the asymptotic power levels are different in common since overall differences such as feedback routines, practical control rod worth are exist between the codes.

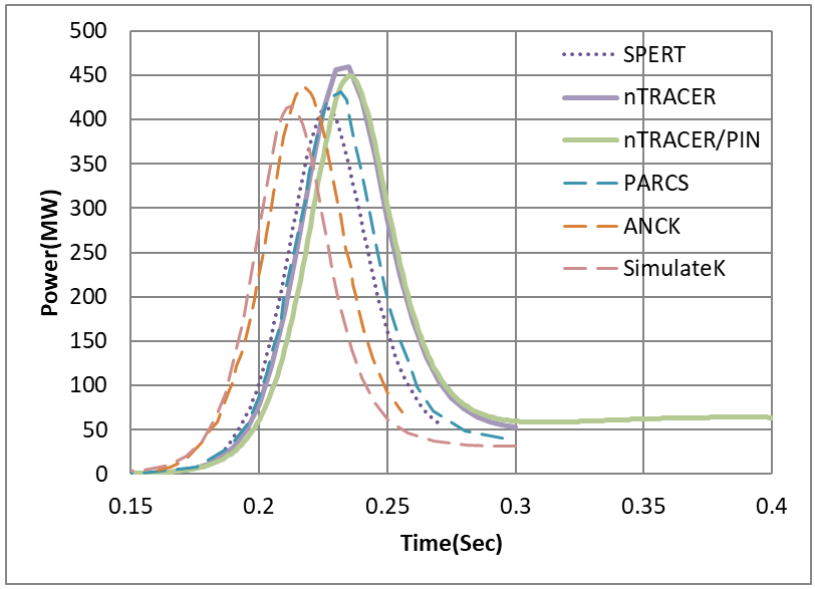

Figure 3.74 The transient core power behavior of the HZP case

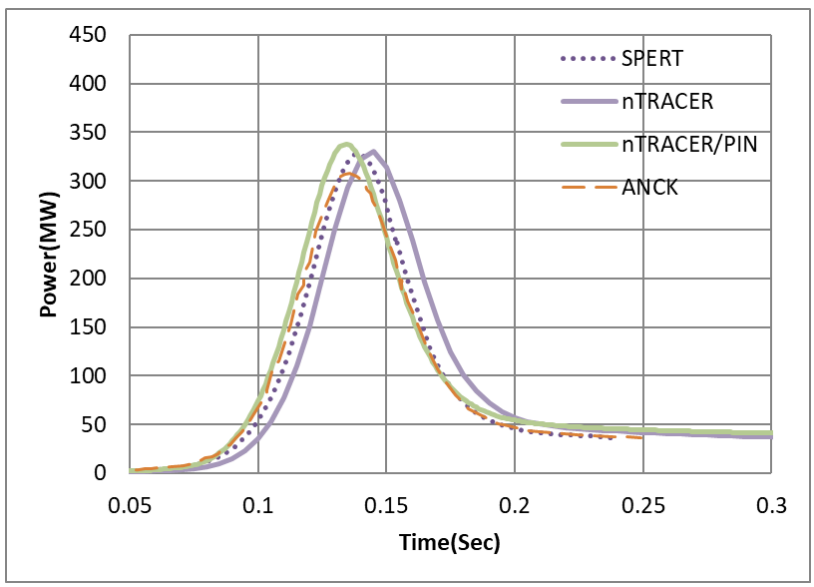

Figure 3.75 The transient core power behavior of the HS case

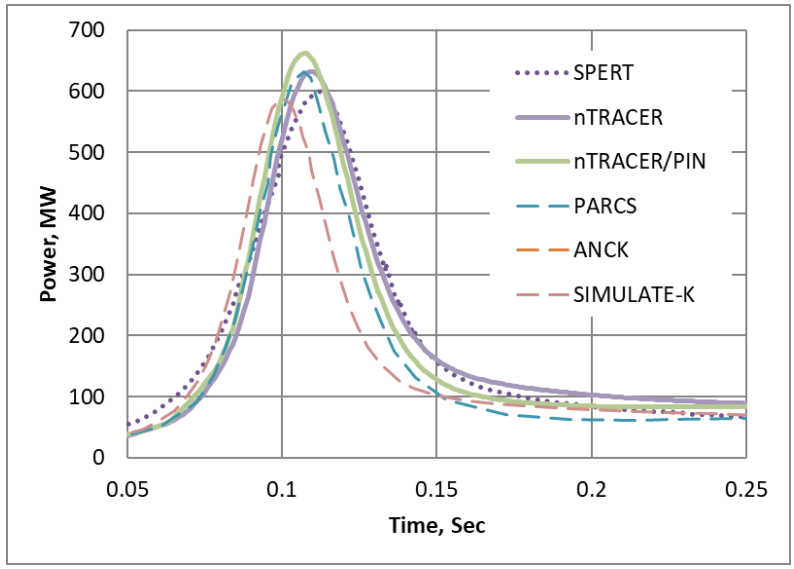

Figure 3.76 The transient core power behavior of the HFP case

4. Conclusions

A new pin-wise three-dimensional nuclear design code has been developed for designing and simulating the commercial reactor cores. In order to establish more accurate solutions, the pin-by-pin neutronics solver with SPH method is implemented. Since too much calculation time is required to the pin-wise three-dimensional calculation, the 2D/1D decoupling method with planar parallelization is introduced as decoupling the three-dimensional calculation into a set of radial and axial calculations. Also, the two-level CMFD calculation is introduced to accelerate the calculation.

For the pin-wise homogenization with a few energy groups, the conventional two-step calculation procedure is used, yet pin-wise group constants are generated with some techniques as described in chapter 0 and 0. Since the pin-by-pin calculation with the pin-wise homogeneous group constants doesn't preserve the solutions of the lattice calculation, the two pin-wise equivalence factors, discontinuity factor and SPH factor, are suggested and investigated for the simple 2x2 checkerboard problems. As results, it is observed that the SPH method can give the competitive solutions to the discontinuity factor which is numerically more exact and the simple application for the implementation.

The L336C5 and VERA benchmark problems are prepared for verifying the pin-by-pin neutronics solver. The whole core transport code nTRACER is

used for generating the pin-wise cross-sections and reference solutions. With the pin-wise homogenization, the assembly-wise homogenization error of the conventional nodal calculation is drastically reduced. And, it is observed that the coarse-group (over four-group) structure is reasonably sufficient to represent the heterogeneity of the reference by comparing the accuracy of calculation for the energy condensation.

In order to evaluate the performance of pin-wise calculation for small modular reactors, the BanDi-50 is chosen. Since it is a boron-free reactor, the lots of burnable absorbers are used and the axially high heterogeneous fuel assemblies are loaded. From calculations of the 3D assembly, 2D core, 3D core problems, it is shown that the accuracy of pin-wise calculations is sufficient to utilize the SMR nuclear design. And also, the APR1400 benchmark problems are solved and the results also shows very good agreement on the results of the whole core transport calculations. the proposed pin-wise calculation methods show the great computing performance about 25 seconds for a 3D quarter-core problem.

Finally, the capability of transient calculation is evaluated with the SPERT III E-Core. Considering the core and fuel assembly geometry which is quite different from the commercial reactors, two-group pin-wise cross-sections are generated with nTRACER for whole core. And, the cross-section function is newly constructed as a function of control assembly and transient

rod positions and fuel and moderator temperatures. The kinetic parameters are also generated from the adjoint calculation of nTRACER. The three super-prompt critical cases (hot-zero-power, hot-standby and hot-full-power) are evaluated and compared with results of other codes. Results of pin-wise calculations shows similar peak core power and time to the reference nTRACER results.

In conclusion, the two-step calculation procedure with pin-wise 2D/1D decoupling method is well established and the calculation performance is optimized with planar and axial parallelization.

5. References

[1] J. I. Yoon and H. G. Joo, "Two-level coarse mesh finite difference formulation with multigroup source expansion nodal kernels," in *J. Nucl. Sci. Technol., 45, 668.*, 2008.

[2] Y. S. Jung and H. G. Joo, "Decoupled planar MOC solution for dynamic group constant generation in direct three-dimensional core calculations," in *International Conference on Mathematics, Computational Methods & Reactor Physics (M&C 2009)*, New York, 2009.

[3] H. G. Joo, J. Y. Cho, K. S. Kim, C. C. Lee and S. Q. Zee, "Methods and Performance of a Three-Dimensional Whole-Core Transport Code DeCART," in *The Physics of Fuel Cycles and Advanced Nuclear Systems*, Chicago, Illinois, USA, 2004.

[4] B. Kochunas, B. Collins, D. Jabaay, T. J. Downar and W. R. Martin, "Overview of development and design of MPACT: Michigan parallel characteristics transport code," in *Proceedings of the 2013 International Conference on Mathematics and Computational Methods Applied to Nuclear Science and Engineering(M&C 2013)*, 2013.

[5] B. William, S. Shaner, L. Li, B. Forget and K. Smith, "The OpenMOC method of characteristics neutral particle transport code," *Annals of Nuclear Energy 68 (2014): 43-52.,* pp. 43-52., 2014.

[6] J. F. Briesmeister, "MCNP-A General Monte Carlo N-Particle Transport Code, Version 5.," LA-UR-03-1987, 2003.

[7] L. M. Petrie, "KENO IV: An improved Monte Carlo criticality program. (No. ORNL-4938)," Oak Ridge National Lab, Tenn.(USA), 1975.

[8] P. K. Romano and B. Forget, "The OpenMC monte carlo particle transport code," *Annals of Nuclear Energy,* no. 51, pp. 274-281, 2013.

[9] K. S. Simth, "Multidimensional nodal transport using the simplified P/sub L/method.," *Transactions of the American Nuclear Society,* no. 52, 1986.

[10] M. Tatsumi, N. Sugimura and A. Yamamoto, "Verification of AEGIS/SCOPE2, a next-generation in-core fuel management system," in *American Nuclear Society*, 2003.

[11] J. C. Lefbvre, J. Mondot and J. P. West, "Benchmark Calculations of Power Distribution (NEACRP-L336)," Organization for Economic Cooperation and Development, 1991.

[12] J. A. Turner, K. Clarno, M. Sieger, R. Bartlett, B. Collins, R. Pawlowski

and R. Summers, "The virtual environment for reactor applications (VERA): design and architecture.," *Journal of Computational Physics,* no. 326, pp. 544-568, 2016.

[13] R. Sanchez, "Approximate solutions of the two-dimensional integral transport equation by collision probability methods," *Nuclear Science and Engineering,* vol. 2, no. 64, pp. 384-404, 1977.

[14] H. G. Joo and J. Y. Cho, "Dynamic implementation of the equivalence theory in the heterogeneous whole core transport calculation," in *PHYSOR 2002: International Conference on the New Frontiers of Nuclear Technology: Reactor Physics, Safety and High-Performance Computing*, Seoul, Korea, 2002.

[15] A. Hebert, "A consistent technique for the pin-by-pin homogenization of a pressurized water reactor assembly," *Nuclear Science Engineering,* vol. 113, p. 227, 2991.

[16] J. T. Hwang, N. Choi and H. G. Joo, "Pin-by-Pin 2D/1D SP3 FDM Scheme with 3D Assembly-wise CMFD Acceleration," in *Transactions of the Korean Nuclear Society Spring Meeting*, Jeju, Korea, 2019.

[17] R. Szilard, H. Zhang, D. Kothe and P. Turinsky, "The Consortium for Advanced Simulation of Light Water Reactors (No. INL/CON-11-22917)," Idaho National Laboratory, 2011.

[18] H. Hong and H. G. Joo, "Analysis of the APR1400 PWR Initial Core with the nTRACER Direct Whole Core Calculation Code and the McCARD Monte Carlo Code," in *Trans. of KNS Spring Meeting*, Jeju, Korea, 2017.

[19] "APR1400 Design Control Document Tier 2, Chapter 4 Reactor," APR1400-K-X-FS-14002-NP, 2018.

[20] "APR1400 Reactor Core Benchmark Problem Book," RPL-INERI-CA-004, Korea Atomic Energy Research Institute, 2019.

[21] H. J. Shim, "McCARD: Monte Carlo Code for Advanced Reactor Design and Analysis," *Nuclear Engineering and Technology,* vol. 44, pp. 161-176, 2012.

[22] J. Dugone, "SPERT III reactor facility: E-core revision," IDO-17036, 1965.

[23] Y. S. Ban, "Development of Advanced Leakage Feedback Method for Two-step Core Analyses," in *Ph.D. Thesis, Seoul National University*, 2018.

[24] H. Hong and H. G. Joo, "Leakage Feedback Method for Pin-by-Pin Core Calculation," in *Trans. of KNS Spring Meeting*, Jeju, Korea, 2019.